Budapest University of Technology and Economics
Faculty of Electrical Engineering and Informatics
Department of Electron Devices

Suspended Microchannel Resonators

Master Thesis

Name: *Maurício Lucena Couto*
Supervisors: *Dr. Ferenc Ender, Assistant Professor*
Annalisa De Pastina, M.Sc. EPFL
Dr. Luis Guillermo Villanueva, Assistant Professor EPFL

Budapest, 2017

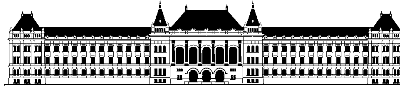

HEAD OF DEPARTMENT

MSc THESIS TASK DESCRIPTION

Maurício Lucena Couto
candidate for MSc degree in Electrical Engineering

Suspended Microchannel Resonators

Background: Suspended Microchannel Resonators (SMRs) are hollow resonant structures containing an embedded U-shaped micro fluidic channel. Having the sample fluid confined inside the resonator allows for real time detection of liquid compounds while the device quality factor remains almost unaffected [1].
Theoretical studies and experimental results have shown that these devices present a *non-monotonic* energy dissipation as the fluid viscosity is increased or decreased. This is in contrast with conventional cantilevers immersed in fluid, where the quality factor monotonically decreases as the fluid viscosity increases [2].
In the simplest configuration, the channel contained inside the cantilever is perfectly centered about the neutral axis of the resonant structure. Analytical models have shown variation of the device quality factor by several orders of magnitude when the microfluidic channel is placed out of the beam neutral axis [2].
This project aims to experimentally demonstrate the relation between SMRs' energy dissipation and off-axis placement of the microfluidic channel, in function of fluidic properties as compressibility and dynamic viscosity.

The student's tasks are the following:

- Review and understand the state of the art about theoretical studies concerning energy dissipation of hollow beam resonators;
- Propose an experimental plan presenting interesting geometries and fluidic properties to be tested;
- Design and fabricate samples to be tested;
- Optimize an experimental setup;
- Collect experimental results and compare with theoretical studies found in literature.

[1] T. P. Burg and S. R. Manalis, "Suspended microchannel resonators for biomolecular detection," *Applied Physics Letters,* vol. 83, pp. 2698-2700, 2003/09/29/ 2003.
[2] J. E. Sader, T. P. Burg, and S. R. Manalis, "Energy dissipation in microfluidic beam resonators," *Journal of Fluid Mechanics,* vol. 650, pp. 215-250, 2010/05// 2010.

Supervisors: Annalisa De Pastina, PhD student EPFL
Luis Guillermo Villanueva, assistant professor EPFL

Supervisor at the department: Dr. Ferenc Ender, assistant professor, ender@eet.bme.hu

Budapest, 27 February 2017

András Poppe, PhD
associate professor
head of department

Budapest University of Technology and Economics
Faculty of Electrical Engineering and Informatics
Department of Electron Devices
Magyar tudósok körútja 2, Building Q, section B, 3rd floor
Budapest, H-1117, Hungary
Tel: +3614632702, E-mail: adm@eet.bme.hu

STUDENT DECLARATION

I, **Mauricio Lucena Couto**, the undersigned, hereby declare that the present MSc thesis work has been prepared by myself and without any unauthorized help or assistance. Only the specified sources (references, tools, etc.) were used. All parts taken from other sources word by word, or after rephrasing but with identical meaning, were unambiguously identified with explicit reference to the sources utilized.

I authorize the Faculty of Electrical Engineering and Informatics of the Budapest University of Technology and Economics to publish the principal data of the thesis work (author's name, title, abstracts in English and in a second language, year of preparation, supervisor's name, etc.) in a searchable, public, electronic and online database and to publish the full text of the thesis work on the internal network of the university (this may include access by authenticated outside users). I declare that the submitted hardcopy of the thesis work and its electronic version are identical.

Full text of thesis works classified upon the decision of the Dean will be published after a period of three years.

Budapest, 3 July 2017

...……………………………………………….
Mauricio Lucena Couto

Abstract

Suspended Microchannel Resonators (SMRs) are hollow resonant structures containing an embedded U-shaped microfluidic channel. Confining the fluid to the inside of the resonator eliminated the problems of damping and viscous drag associated with a conventional solid resonator immersed in fluid. SMRs enable real time detection of liquid compounds with high resolution. They have been successfully used for weighing of biomolecules and single nanoparticles as well as for density and viscosity measurements. It was shown that in these devices the energy dissipation is not a monotonic function of the fluid viscosity, in contrast with conventional cantilevers, where the energy dissipation always increases with the viscosity. Moreover, it was discovered a variation in the device quality factor by several orders of magnitude when the microfluidic channel is placed out of the beam neutral axis.

In this work, SMRs with six different values of channel off-axis placement were successfully fabricated in a cleanroom environment using processes such as photolithography and etching. Two techniques to fill the cantilevers with fluid were proposed and the devices were characterized using laser-Doppler vibrometry and piezoelectricity, for detection and actuation respectively.

The resonance frequency and quality factor were measured for two cantilevers of different lengths at atmospheric pressure and in a vacuum environment. The measured resonance frequencies agreed with the simulations, with a maximum error of 5 %. Quality factors up to 6,000 were achieved for measurements in vacuum, compared to quality factors of hundreds achieved in air.

Table of contents

List of Figures v
List of Tables viii
1 Literature review 1
1.1 Mechanical resonators 1
1.1.1 Quality factor 2
1.1.2 Biosensing 3
1.2 Suspended Microchannel Resonators 4
1.3 Energy dissipation 8
2 Preliminary studies and initial considerations 14
2.1 Preliminary studies 14
2.2 Initial considerations 16
2.2.1 Microchannels 16
2.2.2 Neutral axis and off-axis placement 19
2.2.3 Estimating the Reynolds number β 23
3 Fabrication 25
3.1 Central window definition - First photolithography 26
3.2 Top silicon nitride etching and photoresist strip 29
3.3 Cantilever and inlets definition - Second photolithography 32
3.4 Cantilever release and inlet opening 39
3.5 Main challenges 44
3.6 Summary 46
4 Microfluidic interface 47
4.1 Immersion and sealing 47
4.2 Fluidic connectors 47
5 Characterization 52
5.1 Actuation and detection 52
5.2 Resonance frequency measurement 53
6 Conclusions and outlook 59
Bibliography 60
Appendices 63

List of Figures

Fig. 1: Scanning electron microscopy images of different mechanical resonators 1

Fig. 2: Quality factor extracted from the amplitude-frequency spectrum of a mechanical resonator [5]. 2

Fig. 3: Dynamic mode: The cantilever resonates at a specific frequency. When a mass is added to the beam, the resonant frequency decreases [4]. 3

Fig. 4: Design of a conventional U-tube resonator filled with a viscous fluid [18]. 4

Fig. 5: (a) Suspended microfluidic channel as resonator. (b) Analytes are detected based on their mass density difference relative to the surrounding fluid [19]. 5

Fig. 6: Representation of the two mass measurement modes of a SMR 6

Fig. 7: SMR (left) measures the buoyant mass of the particle in two fluids 7

Fig. 8: Dual SMR schematic 8

Fig. 9: Plot of the normalized quality factor vs Reynolds number, for on-axis channel [1] 10

Fig. 10: Plot of the normalized quality factor vs Reynolds number, for Z0 = 0.1 [30]. 11

Fig. 11: Plot of the normalized quality factor vs Reynolds number, for $\gamma = 0.03$ 12

Fig. 12: Plot of the normalized quality factor vs Reynolds number, for values off-axis placement between 0 and 1 (a) $\gamma = 0.01$, (b) $\gamma = 0.1$ [30]. 13

Fig. 13: Semi-log graph of the normalized quality factor vs off-axis placement. 14

Fig: 14: Normalized quality factor vs off-axis placement, for different values of γ and $\beta = 0.01$. 15

Fig. 15: Normalized quality factor vs off-axis placement, for different values of γ and $\beta = 1$. 15

Fig. 16: Normalized quality factor vs off-axis placement, for different values of γ and $\beta = 100$. 16

Fig. 17: Schematic of the wafer. LPCVD stands for low pressure chemical vapor deposition. 16

Fig. 18: SEM image of the wafer (image provided by Annalisa De Pastina from EPFL). 17

Fig. 19: Wafer layout showing the 16 chips. Image from CleWin 18

Fig. 20: Two chip designs that were used for fabricating SMRs. 18

Fig. 21: 4-cantilever chip. Starting point of the fabrication process. 19

Fig. 22: Cross-section of one of the channels on wafer 63238. Image taken with the SEM. 20

Fig. 23: Plot of Z_0 vs thickness of silicon nitride to be etched for wafer 63238 21

Fig. 24: Plot of Z_0 vs thickness of silicon nitride to be etched for wafer 7304 22

Fig. 25: Plot of Z_0 vs thickness of silicon nitride to be etched for wafer 63236 22

Fig. 26: Representation of the microfabrication process. 25

Fig. 27: First mask design showing the central window and area of each chip. 27

Fig. 28: Successful alignment of the first mask to the layer already present on wafer. 28

Fig. 29: Chip 11 after development.. 28

Fig. 30: Schematic of the wet bench. Baths 1 and 2 filled with remover Shipley 1165 30

Fig. 31: Measurement of the thickness etched on chip 12. A step of 455 nm was measured.. 31

Fig. 32: ATMsse OPTIhot tool used for surface preparation [33]. 33

Fig. 33: ATMsse OPTIspin used for coating. 33

Fig. 34: Spin curve of the photoresist AZ ECI 3027. A rotation speed of 1200 rpm is needed to achieve a film thickness of 5 μm [35] 34

Fig. 35: Design mask for the second photolithography process for chips with 12 cantilevers. Inset shows the cantilevers in detail. Image from CleWin. 35

Fig. 36: Design mask for the second photolithography process for chips with 4 cantilevers. Inset shows the cantilevers in detail. Image from CleWin. 35

Fig. 37: Chip 12 after the development. Image taken with the Optishot microscope with a magnification of 5x. 36

Fig. 38: Chip 10 after the development. Image taken with the Optishot microscope with a magnification of 5x. 37

Fig. 39: Comparison between the photoresist features of an inlet on chip 10 (left) and the CleWin design (right). Image on the left was taken with the Optishop microscope with a magnification of 20x. 38

Fig. 40: Comparison between photoresist area on top of a cantilever on chip 12 (top) and the CleWin design (bottom). Image on top was taken with the Optishot microscope with a magnification of 50x. 38

Fig. 41: Chip 11 after photoresist strip, showing the released cantilevers. Image taken with Optishot microscope with a magnification of 5x. 40

Fig: 42: Chip 11 after photoresist stripping. Image taken with the SEM. 41

Fig. 43: Released cantilevers of chip 11. Image taken with the SEM. 42

Fig. 44: Inlet opening of chip 11. Pillars and apertures from previous microfabrication processes can be seen. Image taken with the SEM. 42

Fig. 45: Zoom at the clamping of a cantilever of chip 11. Image taken with the SEM. 43

Fig. 46: Zoom at the tip of a cantilever of chip 11. Image taken with the SEM. 43

Fig. 47: Chip 10 after the photoresist stripping. Image taken with the SEM. 44

Fig. 48: Chip 8 after development. Excess of resist indicates underexposure. Image taken with Optishot microscope with a magnification of 5x. 45

Fig. 49: Closer look of the chip layout. Inset: inlet dimensions. Image from CleWin. 48

Fig. 50: NanoPort model N-333 [38]. 49

Fig. 51: Examples of NanoPorts. The ring can be seen on the left; mounted NanoPort attached to the chip on the center; NanoPorts with tubing shown on the right [39]. 50

Fig. 52: Slim bonded port from LabSmith attached to a chip. The port interfaces to capillary tubing via one-piece fitting [40]. 50

Fig. 53: Connectors designed using SolidWorks. Left: truncated cone to be attached to a tubing (OD = 1.6 mm). Right: cylinder to be attached to a needle (OD = 0.9 mm). 51

Fig. 54: Connectors bonded to a test wafer. 51
Fig. 55 Schematic of a typical LDV. 52
Fig. 56 Experimental setup for measuring the resonance frequency. Cantilever vibrations are actuated by a piezo crystal and detected by LDV [45]. 53
Fig. 57: Sensor head, vibrometer controller and lock-in amplifier.. 54
Fig. 58: Chamber environment. The platform, the sample and the piezo chip are shown. 55
Fig. 59: Frequency response at the tip of a 250 µm cantilever, showing the first resonance frequency. Measurement performed in vacuum ($2 \cdot 10^{-4}$ mPa) with an actuation voltage of 50 mV. 56
Fig. 60: Fitting of the frequency response with a Lorentzian function (red curve). 56
Fig. 61: Frequency response at the tip of a 500 µm cantilever with a Lorentzian fit (red curve). Measurement performed at atmospheric pressure with an actuation voltage of 100 mV. 57
Fig. 62: Frequency response at the tip of a 500 µm cantilever with a Lorentzian fit (red curve). Measurement performed in vacuum ($2 \cdot 10^{-4}$ mPa) with an actuation voltage of 25 mV. 57
Fig. 63: Representation of the process flow to define the microchannels. EB1 stands for e-beam lithography 1 (Image provided by Annalisa De Pastina from EPFL). 64

List of Tables

Table 1: Layers of the wafers with respective thicknesses. 19
Table 2: Thickness of top layer and internal silicon nitride layer for the different wafers. 20
Table 3: Simulated frequency of the four resonators for different glycerol-water solutions. ..23
Table 4: Reynolds number of the four different resonators for glycerol-water solutions. 24
Table 5: Etch rates for silicon nitride and photoresist with recipe Si_3N_4. 29
Table 6: Etching parameters and desired Z_0 for the first four processed chips.......................30
Table 7: Comparison between expected and actual thickness of silicon nitride etched 31
Table 8: Etching parameters and measurements for chips 6 and 10 32
Table 9: Etching rates for processes used in AMS 200..39
Table 10: Etching steps carried out to release the cantilevers 40
Table 11: Chips processed with the respective Z_0..46
Table 12: Comparison between simulated and measured resonance frequency. 58
Table 13: Comparison between quality factors measured in air and in vacuum. 58
Table 14: Detailed run-card for the microfabrication process. 65

1 Literature review

1.1 Mechanical resonators

Microelectricalmechanical systems (MEMS) can be defined as electrically induced micromechanical resonators. They have been successfully used for a few decades in the fields of communications and sensing, in devices such as gyroscopes, microphones, pressure sensors, accelerometers and mirror arrays for projectors [1]. The well-known Scanning Tunneling Microscope (STM) and Atomic Force Microscope (AFM) are two remarkable examples of MEMS devices. The development of these two microscope techniques is considered a revolution in the atomic and molecular field. The use of the well-established semiconductor technology to fabricate these miniaturized devices and the possibility of integration with microelectronics on a common substrate are among the reasons of the MEMS success.

Mechanical resonators are continuum mechanical structures, such as beams, plates, strings and membranes that exhibit resonance, i.e. naturally oscillate at specific frequencies (resonance frequencies) with greater amplitude than at others. Figure **1** shows some examples of these structures.

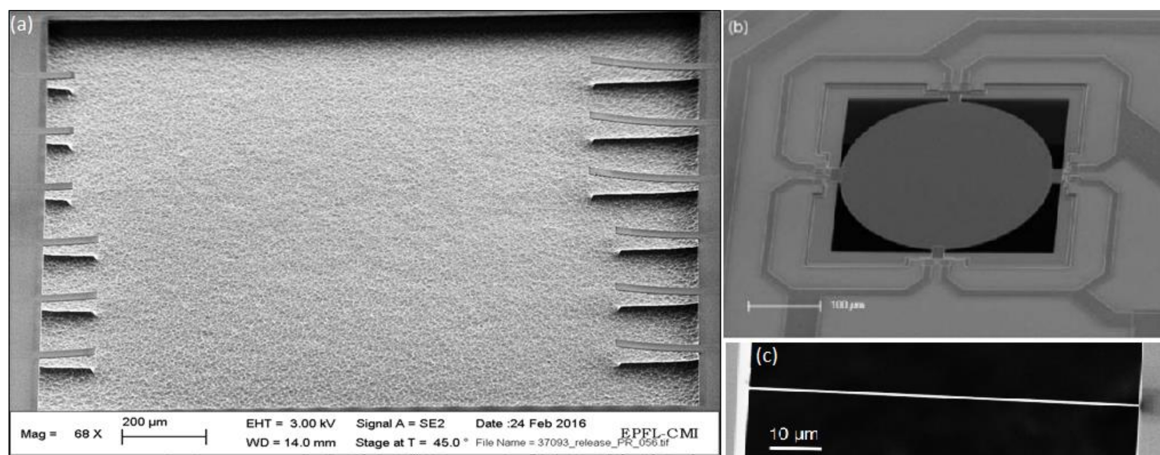

Fig. 1: Scanning electron microscopy images of different mechanical resonators: (a) microcantilever array (image provided by Annalisa De Pastina from EPFL), (b) surface stress membrane-like sensor [2], (c) resonant nanostring [3].

At the resonance frequencies, the energy is commuting between kinetic and potential energy with a small amount being dissipated [1]. It is common to model the resonator as a harmonic oscillator, which means that the resonance frequency is related to the mass m and the spring constant k of the mechanical structure [1]

$$\omega = \sqrt{\frac{k}{m}} \tag{1}$$

1.1.1 Quality factor

A key parameter of a resonator is the so-called quality factor (Q). Q is defined by the ratio between the energy stored and the energy lost during one cycle at resonance [4]

$$Q = 2\pi \frac{W_s}{W_d} \tag{2}$$

where W_s is the stored vibrational energy and W_d is the energy loss during one cycle of vibration. Thus, the quality factor defines the rate at which a resonator dissipates energy.

The quality factor can be calculated from the amplitude-frequency spectrum of the vibration using the following equation

$$Q = \frac{f_0}{\Delta f_0} \tag{3}$$

where f_0 is the resonance frequency and Δf_0 is frequency bandwidth at the 3dB amplitude points as shown in Figure **2** [5]. The quality factor determines the accuracy of the resonance frequency measurement, i.e. how narrow and sharp the peak is. A high quality factor is desired for applications of mechanical resonators.

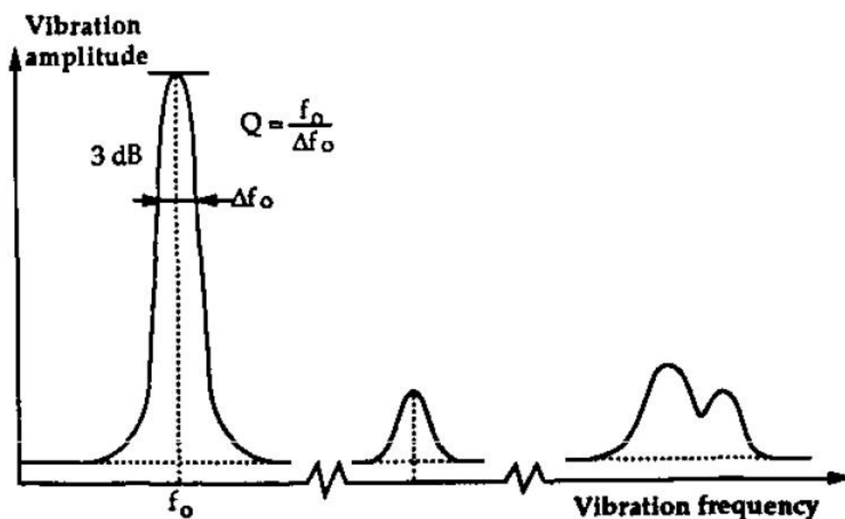

Fig. 2: Quality factor extracted from the amplitude-frequency spectrum of a mechanical resonator [5].

The quality factor of a resonator is the sum of dissipation mechanisms. Energy can be lost to the surrounding medium (gas or liquid), through the clamping to the substrate via elastic waves and through dissipative mechanisms intrinsic to the resonator. Operation in vacuum can eliminate the medium interaction losses while an optimized resonator design minimizes the clamping losses. Intrinsic losses, usually the limiting mechanism of the quality factor, can be reduced by lowering the temperature [1].

1.1.2 Biosensing

Micro- and nanomechanical resonators are widely used as biosensors. They take advantage of their small dimensions to measure with very high resolution physicochemical changes of biological particles. Mechanical biosensors are often singly-clamped beams, also denominated cantilevers [4].

In one of the most common operation modes, the cantilever is driven at its resonance frequency. When a biomolecule lands on top of the cantilever the resonance frequency decreases due to the added mass (see Figure **3**). It can be seen from equation **(1)** that the resonance frequency is strongly affected by the added mass. The mass of the biomolecule is then determined by measuring the change on this resonance frequency.

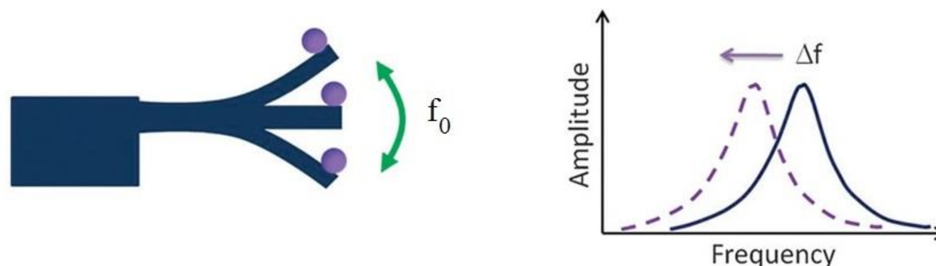

Fig. 3: Dynamic mode: The cantilever resonates at a specific frequency. When a mass is added to the beam, the resonant frequency decreases [4].

Micro- and nanomechanical resonators have proven to measure mass with exquisitely sensitivity [6]–[9]. Recently, the detection limits have been reduced to the yoctogram range (10^{-24} g), enabling the mass measurement of a single proton [4]. To be able to resolve such small mass changes, a resonator with nanoscale dimensions and high quality factors (1,000 - 100,000) is required, which implies that the measurements must be performed in vacuum.

However, sensing of biological particles should be performed in aqueous solutions, the

environment where biological processes occur. This is very challenging as it has been proved that the immersion of resonators in viscous liquids causes substantial energy loss [10], [11]. In other words, the quality factor is severely degraded. It is reduced to around a value of few units [12]–[14], in contrast to very high quality factors larger than 10^4 achieved in vacuum [4]. Moreover, viscous drag also increases the effective mass of the resonator and thus reduces the mass sensitivity. Although the quality factor can be enhanced by using electronic feedback called Q control, the mass responsivity in terms of frequency shift per mass loading is not improved [15]. Miniaturization is not an option either. While it provides significant improvements in gas environments [14], it always leads to a monotonic degradation of quality factor in the case of resonators immersed in liquids [10].

1.2 Suspended Microchannel Resonators

As explained in the last section, the low quality factor combined with the low mass responsivity leads to low sensitivity of micro- and nanomechanical resonators when immersed in liquid. A solution to overcome this limitation is instead of immersing the resonator in the liquid, flow the liquid through the resonator, as it is illustrated in Figure **4**. With this approach, the resonator can still be operated in vacuum, resulting in almost identical quality factors for an empty and filled resonator [16]. This concept has been used for decades, in macroscopic U-tube density meters [17], [18].

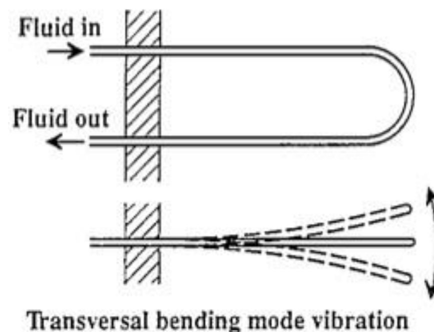

Fig. 4: Design of a conventional U-tube resonator filled with a viscous fluid [18].

In 2003, Manalis' group successfully designed the first micro- and nanomechanical U-tube resonators, also called suspended microchannel resonators (SMR) [19]. These hollow resonant structures containing an embedded U-shaped microfluidic channel differ from the vibrating density meter in the way that the channel is very thin, which enables the detection of biological molecules that bind to the channel walls (Figure **5**). In this work, with a channel of 27 pL (1 pL = 10^{-12} L) volume, they achieved a surface mass resolution of 10^{-17} g/cm2, comparable

to most commercial quartz crystal microbalance (QCM) [20], probably the most widely used mass sensing method nowadays [4]. But for the case of the SMR, the volume of sample needed is minimal, in the picoliter range.

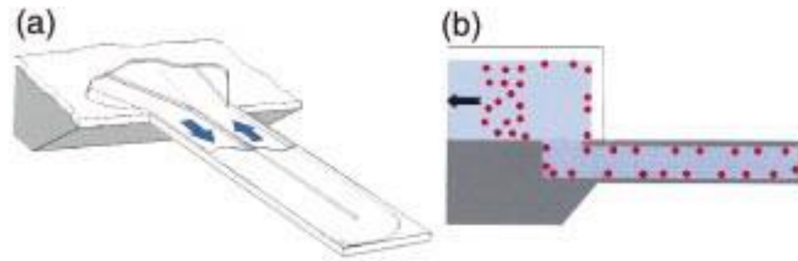

Fig. 5: (a) Suspended microfluidic channel as resonator. (b) Analytes are detected based on their mass density difference relative to the surrounding fluid [19].

In 2006, Burg and Manalis presented a vacuum-packaged SMR [21]. An optimized version of the first SMR suitable for vacuum operation. They showed that the quality factor was increased by more than six times when compared to the operation in air. In addition, they were able to improve frequency stability on the time scale of thirty minutes by five times compared to their previous work. This is very important for detecting slow binding molecules at low concentration.

In a later work, Burg et al [16] demonstrated that SMR enables the weighing of single nanoparticles, single bacterial cells and sub-monolayers of adsorbed proteins. An improvement in mass resolution of six orders of magnitude over a state-of-the-art QCM was achieved, with a quality factor of 15,000. In this work, the authors demonstrated biological measurements through the two mass measurement modes enabled by a fluid-filled microcantilever: surface-based and flow through detection scheme (see Figure **6**). In the first, the inside walls of the channels were functionalized with antibodies to measure the binding to the respective antigens. In the latter, the mass of bacteria and synthetic nanoparticles was measured when in transit through the SMR. The resonance frequency drops by an amount that depends not only on the particle density and volume, but also on the position of the particle along the resonator. When particles reach the tip, the frequency shift is at a maximum.

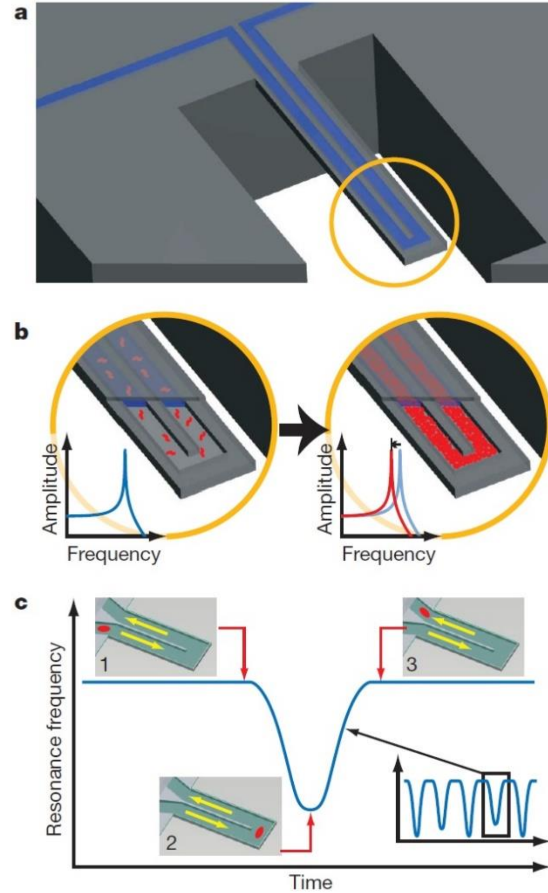

Fig. 6: Representation of the two mass measurement modes of a SMR. a) A SMR translates mass changes into changes in the resonance frequency. Fluid continuously flows through the channel delivering biomolecules, cells or synthetic particles. b) Surface adsorption mechanism: molecules that bind to the channel wall accumulate inside the device. This enables specific detection by way of immobilized receptors. c) Particles flow through the cantilever without binding to the surface. The observed signal depends on the position of particles along the channel. The exact mass excess of a particle can be quantified by the peak frequency shift induced at the apex (inset 2) [16].

In 2011, Manalis group measured the buoyant mass of cells in two fluids with different densities with the purpose of determining the density, mass and volume of a large number of single cells [22]. The buoyant mass m_b is defined as the mass of a particle over that of fluid it displaces and can be expressed by

$$m_b = m\left(1 - \frac{\rho_f}{\rho}\right) \quad (4)$$

where m is the mass of the particle, ρ_{fluid} is the density of the fluid and ρ is the density of the particle. The cantilever oscillates at a frequency that is proportional to its mass.

When a cell is passing through the microchannel, a change in the frequency occurs and it is proportional to the buoyant mass of the cell. Figure **7** illustrates the measurement principle. It

is important to note that this work differs from the previous ones using SMRs [23], [24] due to the fact that the density of a single cell could be measured, instead of the average density of a cell population. It was found that the cell-to-cell variation in density is 100-fold smaller than the mass or volume variation. This means that the cell density is an excellent indicator of cellular processes that would not be detectable by mass or volume measurements.

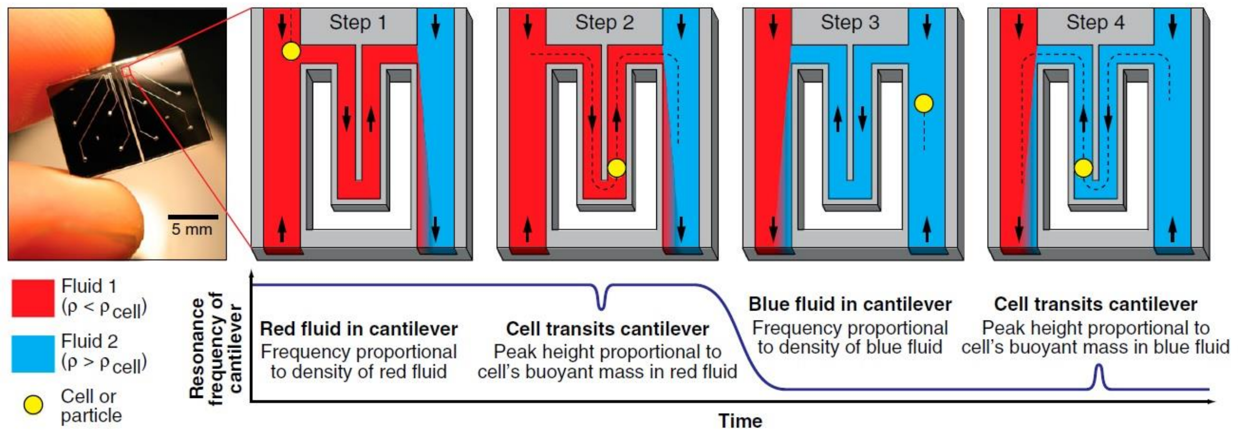

Fig. 7: SMR (left) measures the buoyant mass of the particle in two fluids with different densities. The buoyant masses of the cell in the two fluids are calculated from the height of the peak in the resonance frequency (steps 2 and 4). From the measurements of fluid density and cell buoyant mass, the absolute mass, volume, and density of the cell are calculated [22].

More recently, the same group introduced a new device to measure single cell mass, volume and density [25]. The principle is the same as the previous work, but instead of using one SMR, the new device is a dual SMR; i.e. two resonators connected by a serpentine fluidic channel, as shown in Figure **8**. The new design was developed to achieve a high-throughput cellular analysis method.

Other state-of-the-art applications of the SMR include monitoring the growth of single cells [26], characterizing deformability and surface friction of cancer cells [27] and viscosity measurements [28].

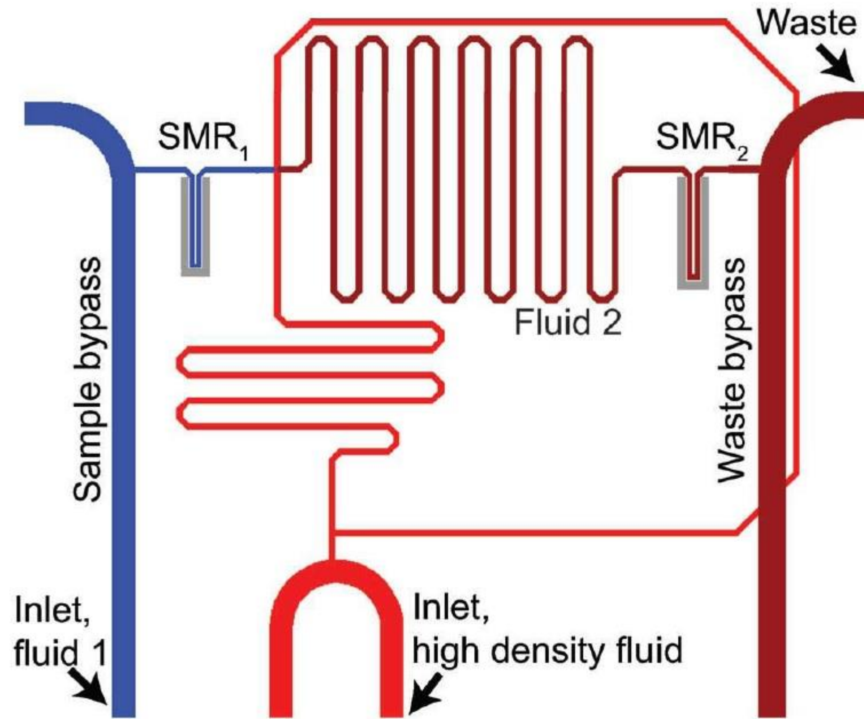

Fig. 8: Dual SMR schematic. A single cell flows into the SMR1 for the first buoyant mass measurement in fluid 1. The cell then travels to a cross-junction where a high density fluid is introduced and mixes with fluid 1 in the serpentine channel. As the particle flow through SMR2 in this mixed fluid (fluid 2) the second buoyant mass measurement takes place [25].

1.3 Energy dissipation

Fluid damping has always limited the use of resonating microcantilevers immersed in liquid as a micro- and nanomechanical sensor. As discussed in the previous section, fluid damping imposes a severe degradation to the signal-to-noise of measurements by lowering the mass responsivity and the quality factor of these sensors. The SMR proposed by Manalis' group constitutes an alternative to overcome these limitations. It was observed that the energy dissipation in these novel devices was four orders of magnitude lower than the energy dissipation in the conventional immersed microcantilevers [16].

When studying the fluid dynamics of such devices, Burg et al [29] discovered surprising connections between the fluid properties, energy dissipation and the device dimensions. It was observed a non-monotonic energy dissipation due to the fluid in such devices, in contrast to the case for the conventional microcantilever immersed in liquid, where the quality factor (inverse scaled energy dissipation) is always degraded with increasing viscosity. As a direct consequence of this discovery, it is possible to enhance the quality factor upon miniaturization, which was never the case for the microcantilevers immersed in fluid. This leads to the

development of devices with even enhanced sensitivity to environmental changes, e.g. mass variations in liquid.

A theoretical model to explain the physics mechanisms of the energy dissipation in the SMRs was proposed by Sader et al and validated through measurements [30]. This model provided a self-consistent treatment of the fluid and solid mechanics by combining the Navier-Stokes equations with Euler-Bernoulli beam theory. It is important to note that the model focused on energy dissipation due to the fluid only, neglecting then the dissipative mechanisms happening in the solid cantilever structure.

Consider the case of a rectangular cantilever whose length L is much larger than its width w and thickness h, with a thin embedded channel containing fluid whose height h_{fluid} is much smaller than its width w_{fluid}. In this case, the quality factor of the fundamental mode of vibration resulting from the flow of a viscous fluid inside the channel is given by

$$Q_{fluid} = F(\beta)\left(\frac{\rho}{\rho_{fluid}}\right)\left(\frac{h}{h_{fluid}}\right)\left(\frac{w}{w_{fluid}}\right)\left(\frac{L}{h_{fluid}}\right)^2 \quad (5)$$

where ρ_{fluid} and ρ are respectively the fluid density and the cantilever average density.

For a special case where the channel midplane lies on the neutral axis of the cantilever and the fluid inside the channel is incompressible, the dimensionless function $F(\beta)$ is well approximated by

$$F(\beta) \approx \frac{38.73}{\beta} + 0.1521\sqrt{\beta} \quad (6)$$

which is a function of the Reynolds number β

$$\beta = \frac{\rho_{fluid} h_{fluid}{}^2}{\mu}\omega \quad (7)$$

where μ is the fluid shear viscosity and ω is the angular velocity of the cantilever vibration.

The Reynolds number β indicates the importance of the fluid inertia. The dimensionless function $F(\beta)$ is termed the normalized quality factor and it is related to the quality factor via the geometric and material properties of the fluid and cantilever, as can be inferred from equation **(5)**. A plot of the normalized quality factor is shown in Figure **9**. Equation **(6)** corresponds to the sum of two extreme solutions. The first term is the solution for the small β regime ($\beta \ll 1$) while the second term is the solution for the large β regime ($\beta \gg 1$). As it can

be deduced from Figure **9** that the quality factor is a non-monotonic function of the Reynolds number. This is equivalently to say that, for a fixed geometry, the energy dissipation is a non-monotonic function of the fluid viscosity.

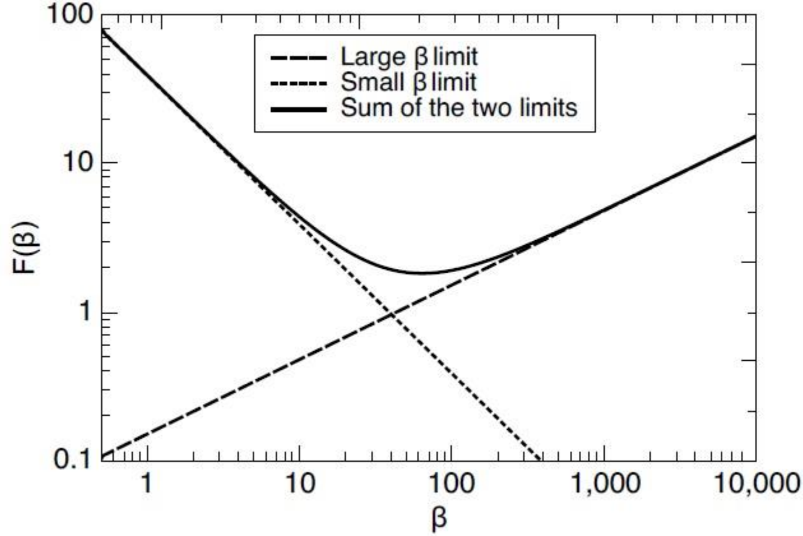

Fig. 9: Plot of the normalized quality factor vs Reynolds number, for on-axis channel [1].

In the large β regime, the energy dissipation increases (quality factor drops) with increasing viscosity (decreasing β). This is expected intuitively as the fluidic behavior is dominated by the inertia inside the vibrant cantilever. This inertia flow generates viscous boundary layers, which are sources of energy dissipation. When viscosity increases, the thickness of the viscous boundary layers is increased, and hence, the energy dissipation. On the other hand, the behavior in the small β regime is apparently counter-intuitive, as an enhancement in viscosity (reduction in β) reduces the energy dissipation (quality factor increases). In this regime, the effect of fluid inertia disappears, and the fluid behaves like a rigid-body, meaning that there is no generation of viscous boundary layers.

This behavior explained above, represented by Figure **9**, considered an on-axis fluidic channel. This means that the channel midplane lies on the neutral axis of the beam. Neutral axis, by definition, is the axis wherein the beam experiences zero strain and stress. When there is a small asymmetry of the embedded channel cantilever about its neutral axis, one says that the channel has an off-axis placement, z_0. This parameter is defined as the distance between the channel midplane and the neutral axis of the cantilever beam and it is normally due to finite fabrication tolerances. In the same work, Sader et al took the off-axis placement of the channel into consideration. It was demonstrated that z_0 strongly affect the quality factor as it can be seen in the equation below for an approximated normalized quality factor

$$F(\beta) \approx \begin{cases} \frac{38.73\beta}{\beta^2+564.6Z_0^2\left(1+\frac{\beta^2}{8400}\right)} & : \ \beta \to 0 \\ \frac{\sqrt{\beta}}{6.573+1.718Z_0^2} & : \ \beta \to \infty \end{cases} \quad (8)$$

where Z_0 is the ratio between the off-axis placement z_0 and the channel height h_{fluid}.

A plot of the normalized quality factor is shown in Figure **10** for $Z_0 = 0.1$. In the small β regime the quality factor increases with increasing β until a maximum is reached, then the quality factor starts decreasing for an increase in β. This can be explained as it follows. Before this maximum in β, oscillatory inflow/outflow within the channel due to off-axis placement dominates the inertial mechanisms explained for the on-axis case. On the other hand, increasing β further (larger than the maximum) will decrease the quality factor as the inertial mechanisms dominates the inflow/outflow in the channel. In the large β regime, the quality factor increases with increasing β, as for the case of the on-axis channel. It can be inferred that the off-axis placement dominates the behavior only for the small β regime.

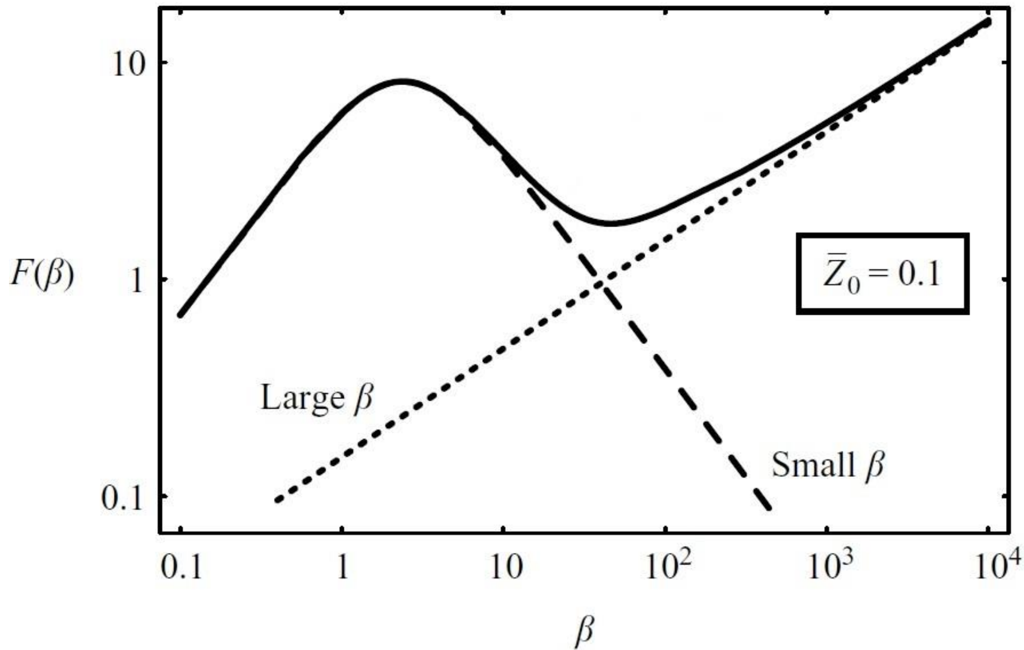

Fig. 10: Plot of the normalized quality factor vs Reynolds number, for Z0 = 0.1 [30].

Another breakthrough finding from the same work was the effect of the fluid compressibility on the fluids dynamics and consequently on the energy dissipation. It was discovered that compressibility only affects the off-axis flow problem. Hence, it has an effect only in the small β regime. For the compressibility effect, two variables need to be considered. The normalized wavenumber γ that indicates the importance of acoustic effects can be defined as

$$\gamma = \left(\frac{\omega L}{c}\right)^2 \tag{9}$$

where c is the speed of sound.

The other variable is termed compressibility number α and dictates when the fluid compressibility significantly affects the flow. It is defined as the ratio between γ and β [30]. Hence, α and γ are directly proportional. Figure **11** shows the plot of the normalized quality factor for a typical value of γ and for a range of different off-axis positions between 0 and 0.1. Comparing the curve for $Z_0 = 0.1$ with the incompressible solution in Figure **10**, it is clear that the compressibility strongly affects the small β regime. Instead of one maximum in quality factor, two maxima can be seen in the case where compressibility is considered. It can be also observed that the quality factor always ultimately increases at lower β, independent of the value of Z_0, which is not the case for the incompressible flow where the quality factor decreases with decreasing β for the small β regime.

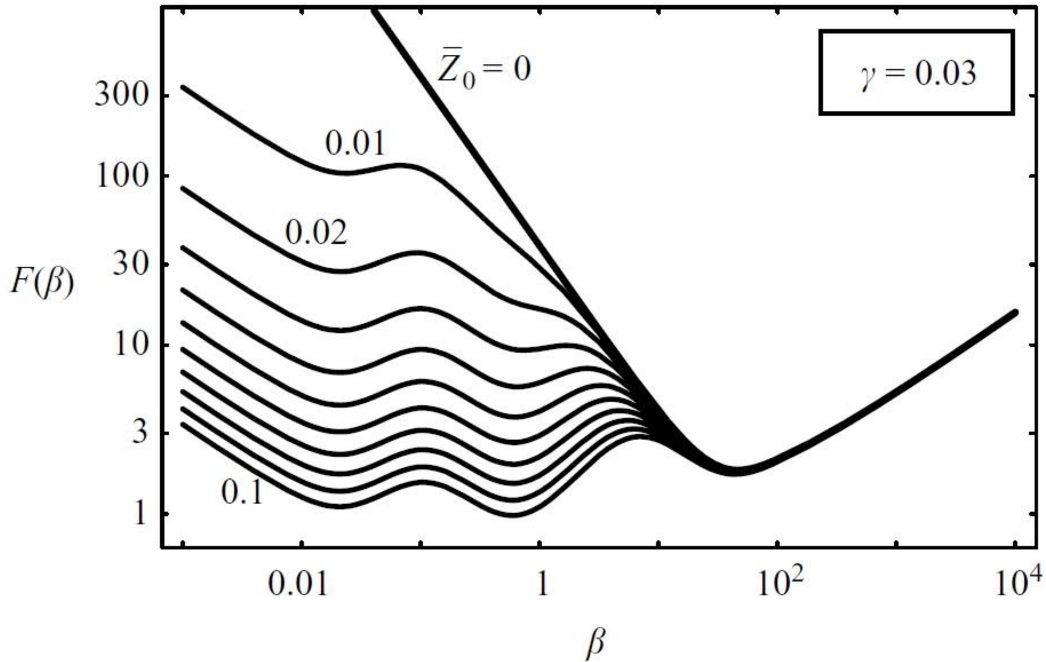

Fig. 11: Plot of the normalized quality factor vs Reynolds number, for $\gamma = 0.03$ and various off-axis placement between 0 and 0.1, with increments of 0.01 [30].

The effect of varying the compressibility for a fixed interval of Z_0 is shown in Figure **12**. It is clear that compressibility reduces dissipation due to off-axis placement. In other words, the quality factor increases with increasing γ.

The validation of this theoretical model was demonstrated by comparison with detailed

measurements taken on two SMR of different dimensions using fluids whose viscosities were varied over three orders of magnitude. As the off-axis placement of the fluid channel was unknown, it was used as a fitting parameter in the comparison.

To summarize the findings in this work, it was discovered that not only the fluid properties of viscosity and density play a role in the fluid dynamics, but also the fluid compressibility. The non-monotonicity in energy dissipation is a result of competing effects due to fluid inertia and fluid compressibility. In the high inertia regime, i.e. large β regime, energy dissipation always increases with increasing viscosity. In the low inertia regime, however, energy dissipation oscillates with increasing viscosity.

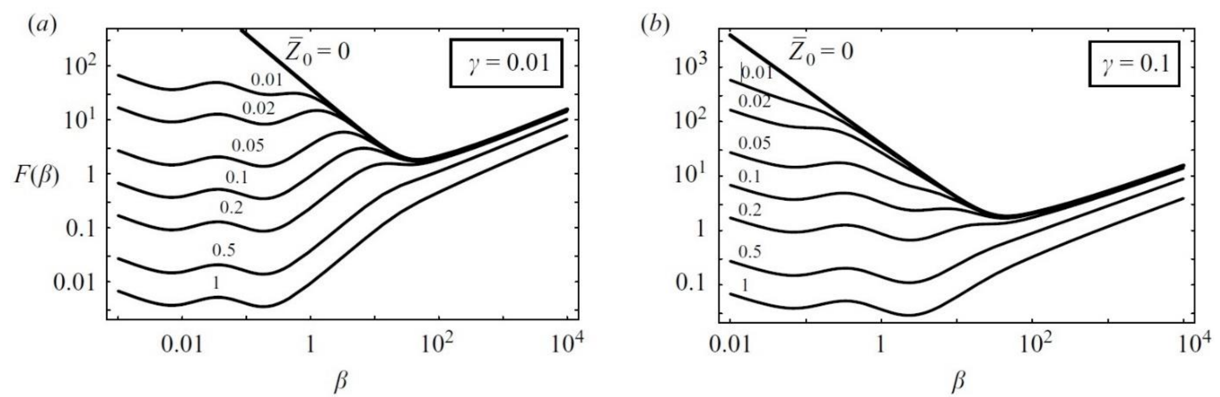

Fig. 12: Plot of the normalized quality factor vs Reynolds number, for values off-axis placement between 0 and 1 (a) γ =0.01, (b) γ =0.1 [30].

2 Preliminary studies and initial considerations

2.1 Preliminary studies

To understand better the effect of the off-axis channel placement, the normalized quality factor *F(β)* with relation to Z_0 was initially plotted for different values of the Reynolds number β. The data were extracted from [30]. Figure **13** shows this plot for $\gamma = 0.01$. As expected, the off-axis channel placement strongly affects the normalized quality factor, and consequently the energy dissipation. This effect is much enhanced for small values of β, as it can be seen from the decay of the curves.

The effect of the fluid compressibility with respect to Z_0 was also studied in more details. Plots of the normalized quality factor versus the off-axis placement of the channel for different values of γ, at fixed β`s are shown from Figure **14** to Figure **16**. Comparing the plots, it can be inferred that the quality factor is enhanced with increasing γ. In addition, as β is increased, the effect of the compressibility becomes less significant.

It can be concluded from these preliminary studies that the predominant variation of the normalized quality factor as a function of Z_0 occurs for values of Z_0 between 0 and 0.2.

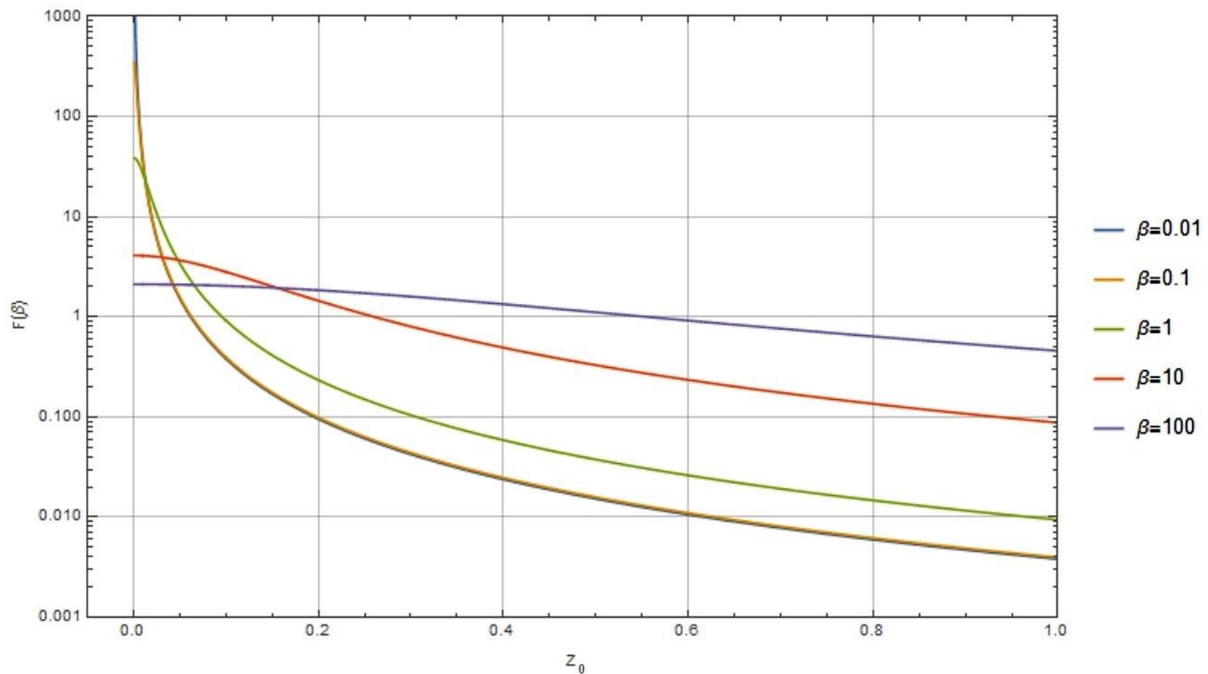

Fig. 13: Semi-log graph of the normalized quality factor vs off-axis placement, for different values of Reynolds number β.

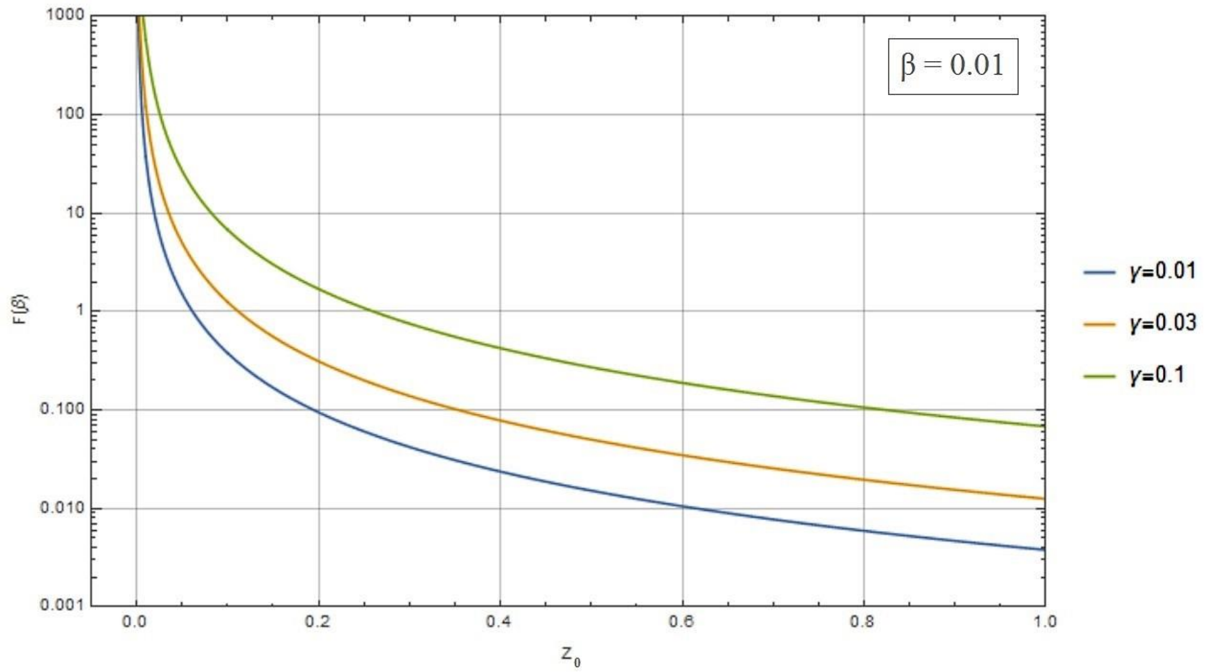

Fig: 14: Normalized quality factor vs off-axis placement, for different values of γ and β = 0.01.

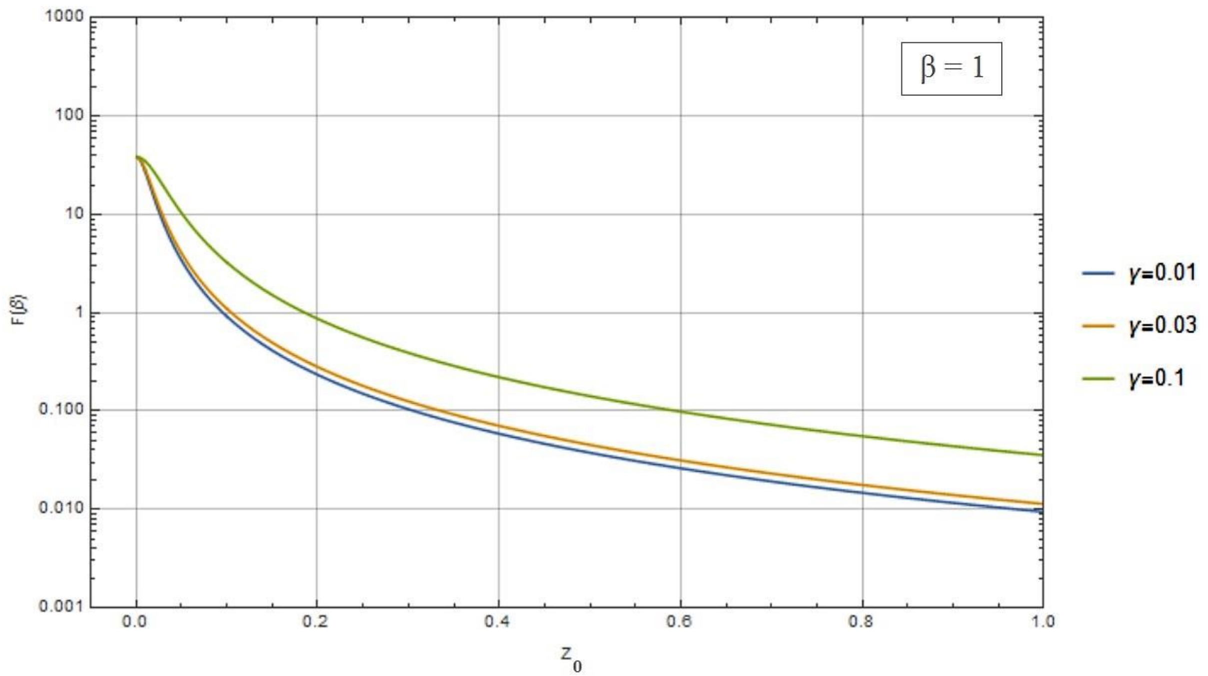

Fig. 15: Normalized quality factor vs off-axis placement, for different values of γ and β = 1.

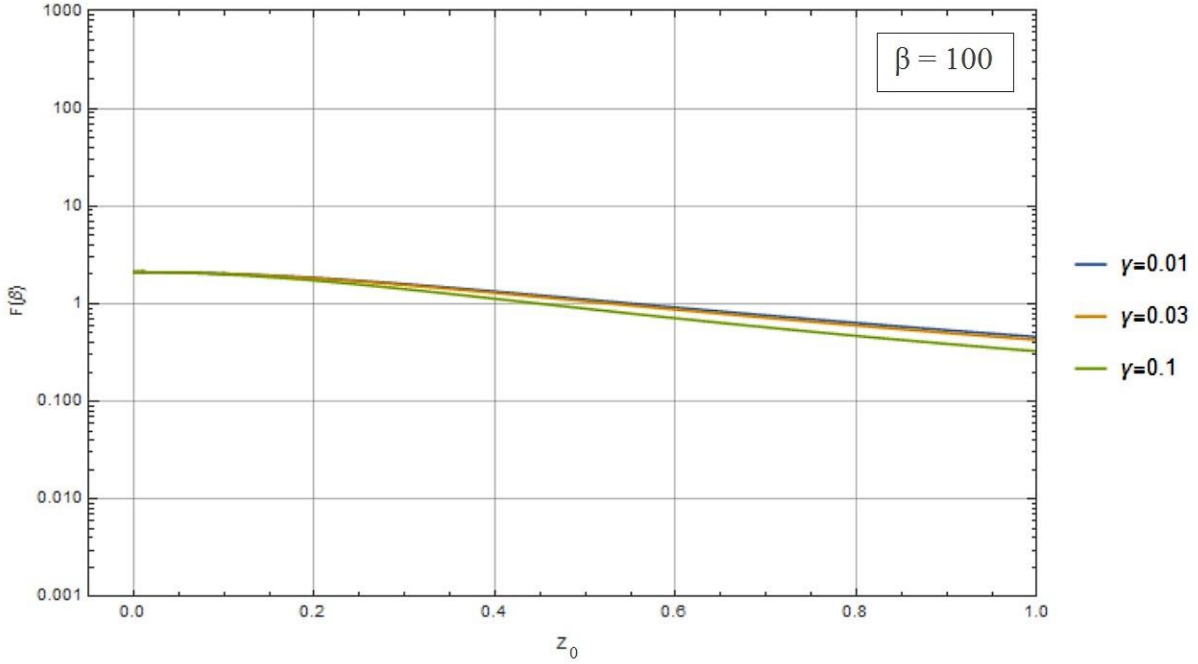

Fig. 16: Normalized quality factor vs off-axis placement, for different values of γ and $\beta = 100$.

2.2 Initial considerations

2.2.1 Microchannels

Three 4-inch (100 mm) wafers were used for fabricating the suspended microchannel resonators. The wafers will be hereinafter referred to as their IDs: 7304, 63236 and 63238. Prior to this work, microfabrication processes were carried out on these wafers up to the definition of the microchannels. These processes included material deposition, e-beam lithography and etching. The detailed process flow can be found in appendix A. The last process previously conducted was a chemical vapor deposition of a layer of low stress silicon nitride, in order to close the microchannels. Figure **17** illustrates the schematic cross-section of the wafer. The wafer is comprised of layers of silicon, silicon nitride and polysilicon. Figure **18** shows a scanning electron microscope (SEM) image of a wafer which underwent the same process flow of wafers 7304, 63236 and 63238.

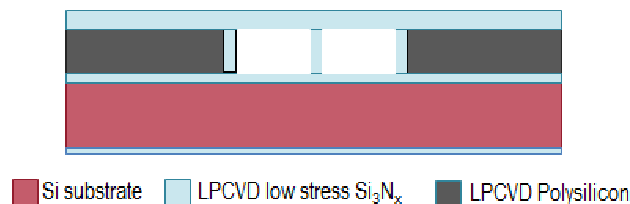

Fig. 17: Schematic of the wafer. LPCVD stands for low pressure chemical vapor deposition.

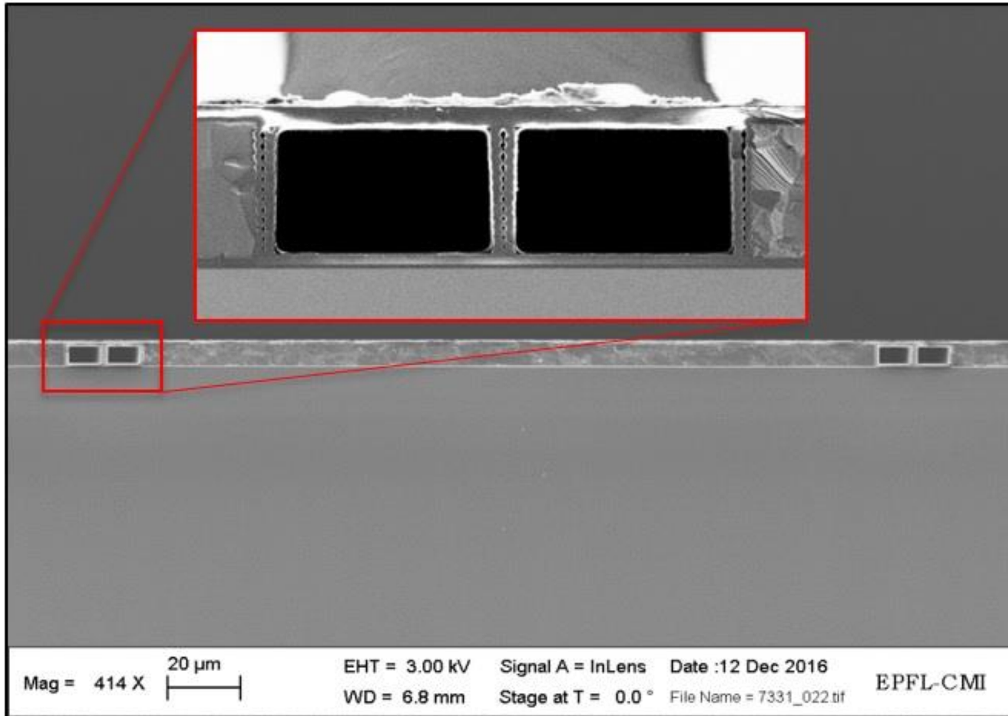

Fig. 18: SEM image of the wafer (image provided by Annalisa De Pastina from EPFL).

Each wafer contains sixteen chips as shown in Figure **19**. There are four different designs among the chips, in which serpentine beams, doubly-clamped beams and cantilevers can be defined. Four inlets were defined for each chip. In the picture, we can also observe the features on the sides of the mask design. They are alignment marks which help the alignment of the subsequent layers. In this work, two designs were used, in which cantilevers were defined, as the theoretical model from Sader et al. [30] studied only the energy dissipation in singly-clamped beams. The two designs differ only in the number of cantilevers. Figure **20** illustrates these two designs and Figure **21** shows an image of a chip fabricated using one of the designs. As it can be seen, channels with four different lengths were fabricated. They are 250 μm, 500 μm, 750 μm and 1000 μm long.

Fig. 19: Wafer layout showing the 16 chips. Image from CleWin.

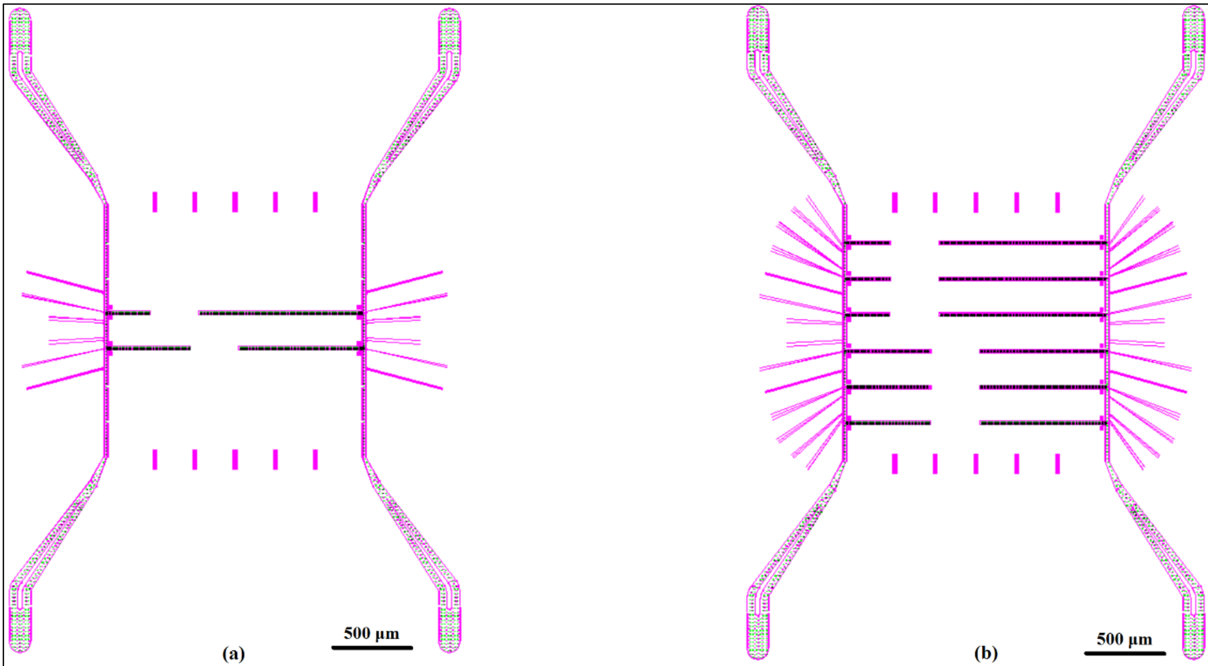

Fig. 20: Two chip designs that were used for fabricating SMRs. a) 4-cantilever chip, b) 12-cantilever chip. Image from CleWin.

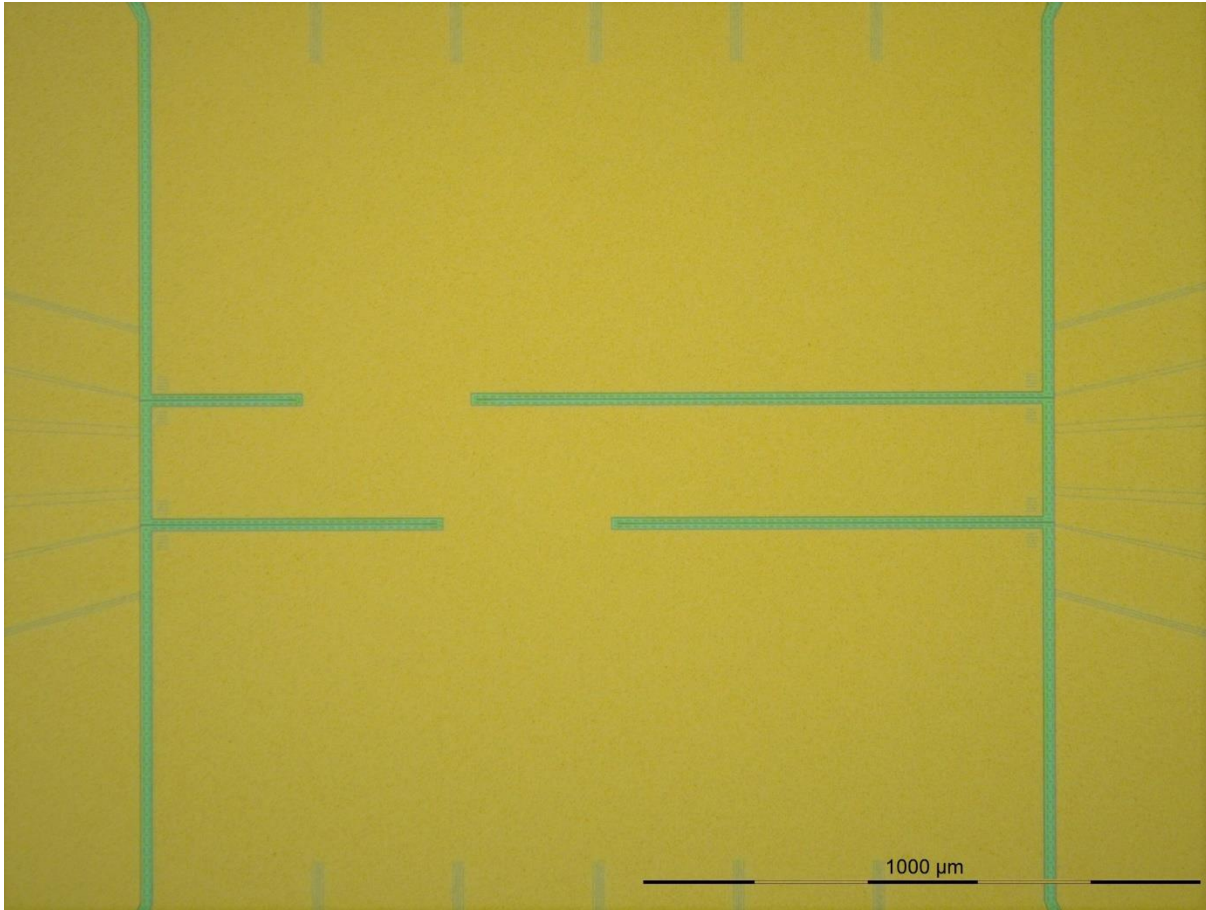

Fig. 21: 4-cantilever chip. Starting point of the fabrication process. Image taken with the Optishot microscope, with a magnification of 5x.

2.2.2 Neutral axis and off-axis placement

As it was explained in section 1.3, the off-axis placement z_0 is the distance between the beam neutral axis and the channel midplane. The dimensions of the cantilever and the channel, as well as the thicknesses of the layers must be known to calculate the neutral axis. Table **1** lists the thickness of the layers deposited during the fabrication of the microchannels. The thickness of the top silicon nitride varied from wafer to wafer. The cantilever and channel widths according to the design should be respectively 30 μm and 10 μm. The channel thickness would ideally be the thickness of the polysilicon layer, whereas the cantilever thickness would be the sum of the bottom silicon nitride, polysilicon and top silicon nitride layers (see Figure **17**).

Table 1: Layers of the wafers with respective thicknesses.

Layer	Thickness (µm)
Bottom silicon nitride	0.5
Polysilicon	6
Top silicon nitride	1.7 – 2

When depositing top silicon nitride to close the channel, however, part of the material was deposited on the internal walls of the channels, creating an internal layer of silicon nitride. Consequently, the channel dimensions were found to be smaller than what was designed. With the purpose of finding the thickness of the internal silicon nitride layer, (i.e. the exact channel dimensions) the wafers were observed under the SEM. Figure **22** illustrates one of the measurements.

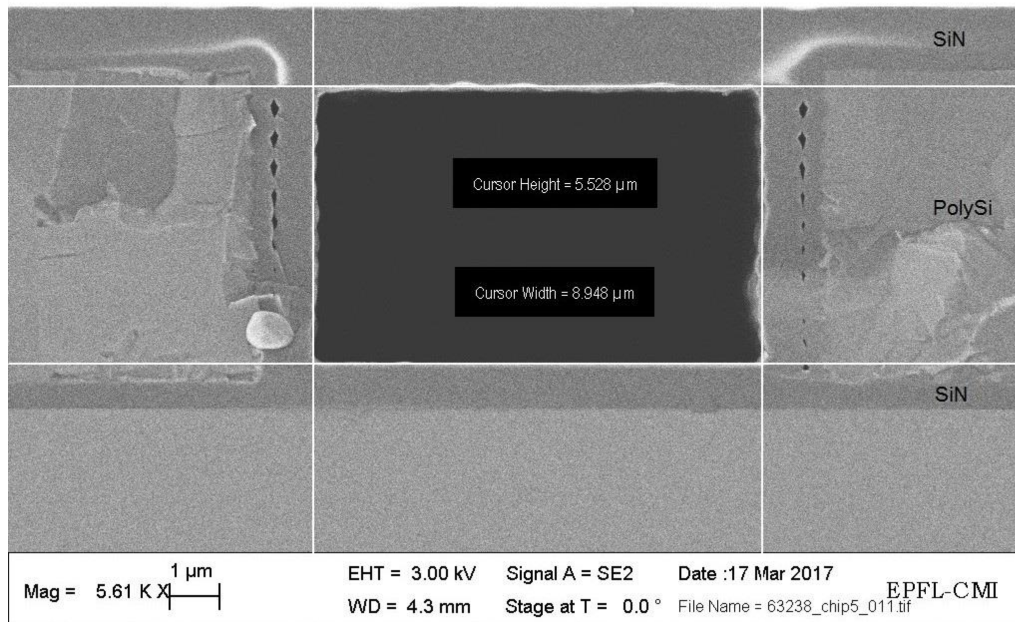

Fig. 22: Cross-section of one of the channels on wafer 63238. Image taken with the SEM.

Table **2** shows the thickness of the silicon nitride layer on top of the microchannels as well as the internal layer of silicon nitride for the three wafers, after the measurements with the SEM. The neutral axis was calculated using the values shown in Table **2** and the value of Z_0 was found to be approximately 0.2 for wafers 63238 and 7304 and 0.25 for wafer 63236. The calculations were carried out using the software Mathematica and can be found in appendix B.

Table 2: Thickness of top layer and internal silicon nitride layer for the different wafers.

Wafer	Top silicon nitride (µm)	Internal silicon nitride (µm)
63236	1.8	0.25
63238	1.3	0.3
7304	1.4	0.7

To fabricate suspended microchannel resonators with different values of Z_0 (off-axis placement z_0 over the channel thickness), the neutral axis should have different values. In other words, the

thickness of the top layer of silicon nitride should be modulated. A range of Z_0 was then selected and the thickness of the top layer of silicon nitride was calculated for these Z_0's. For values of Z_0 between 0 and 0.2, a predominant variation in the normalized quality factor is observed, as discussed in section 2.1. Considering this and the fact that it would be interesting to observe what occurs with the quality factor for negative values of off-axis placement, a range of Z_0 between -0.05 and 0.2 was selected (0.25 for wafer 63236).

Figure **23** shows the plot of Z_0 in function of the amount of layer of silicon nitride to be etched for wafer 63238. To achieve a Z_0 of zero (on axis case) for example, 800 nm of the top layer of silicon nitride must be etched. Figure **24** and Figure **25** illustrate the plots for wafers 7304 and 63236 respectively.

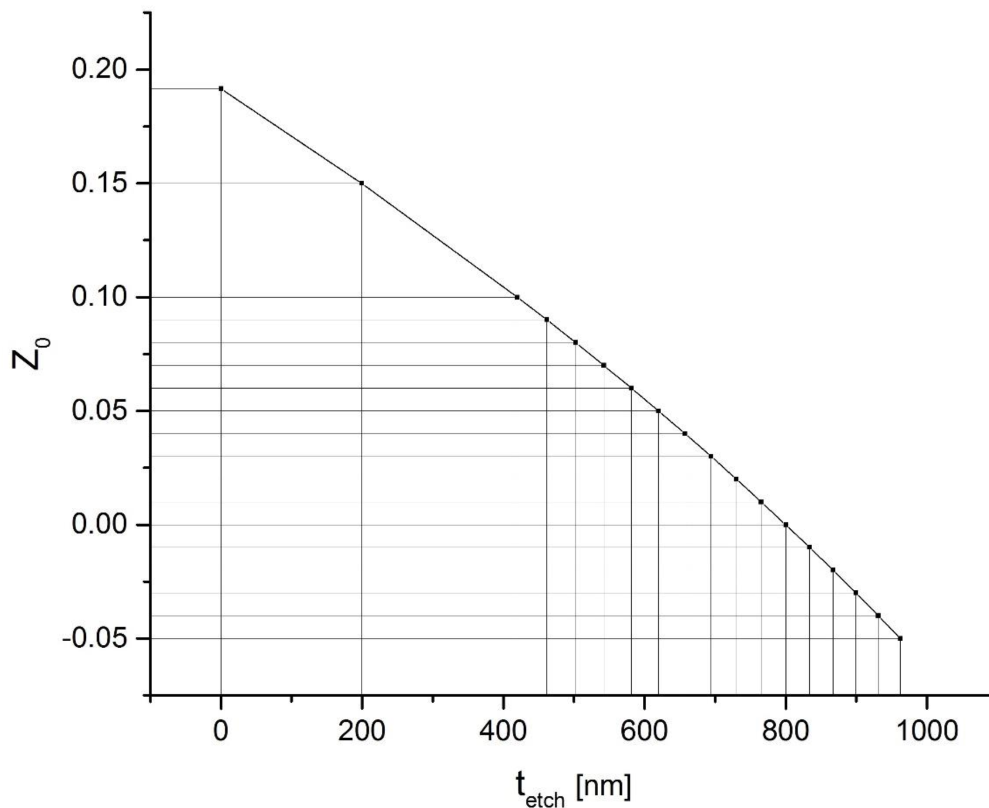

Fig. 23: Plot of Z_0 vs thickness of silicon nitride to be etched for wafer 63238.

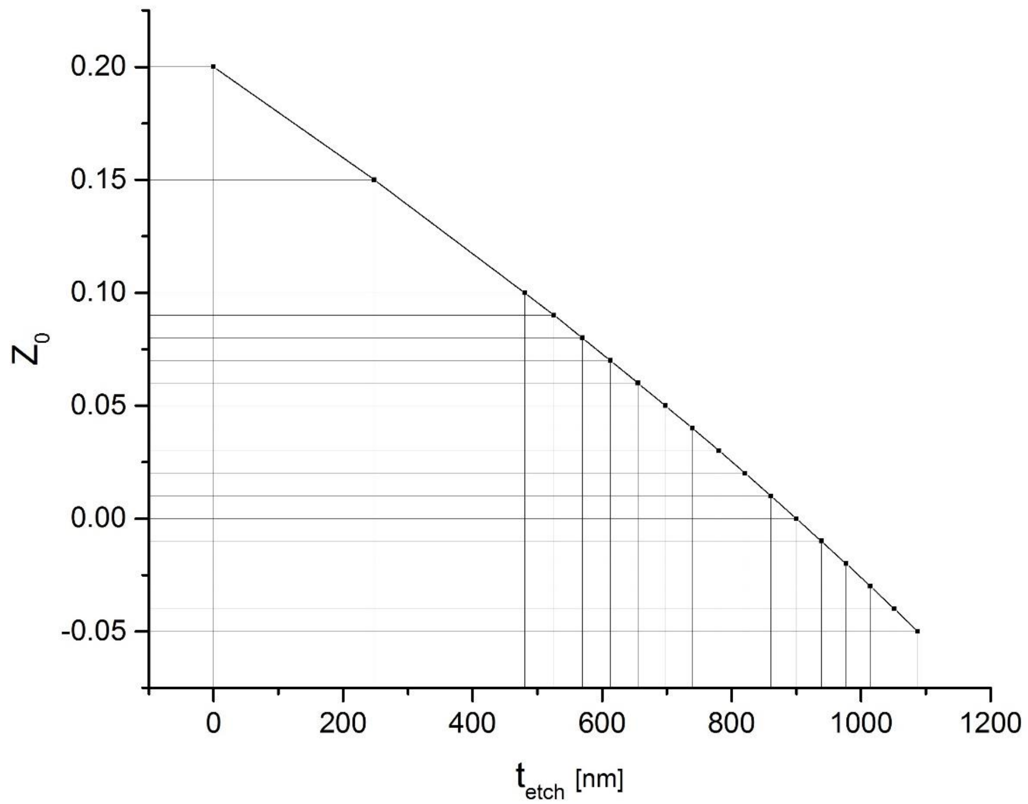

Fig. 24: Plot of Z_0 vs thickness of silicon nitride to be etched for wafer 7304.

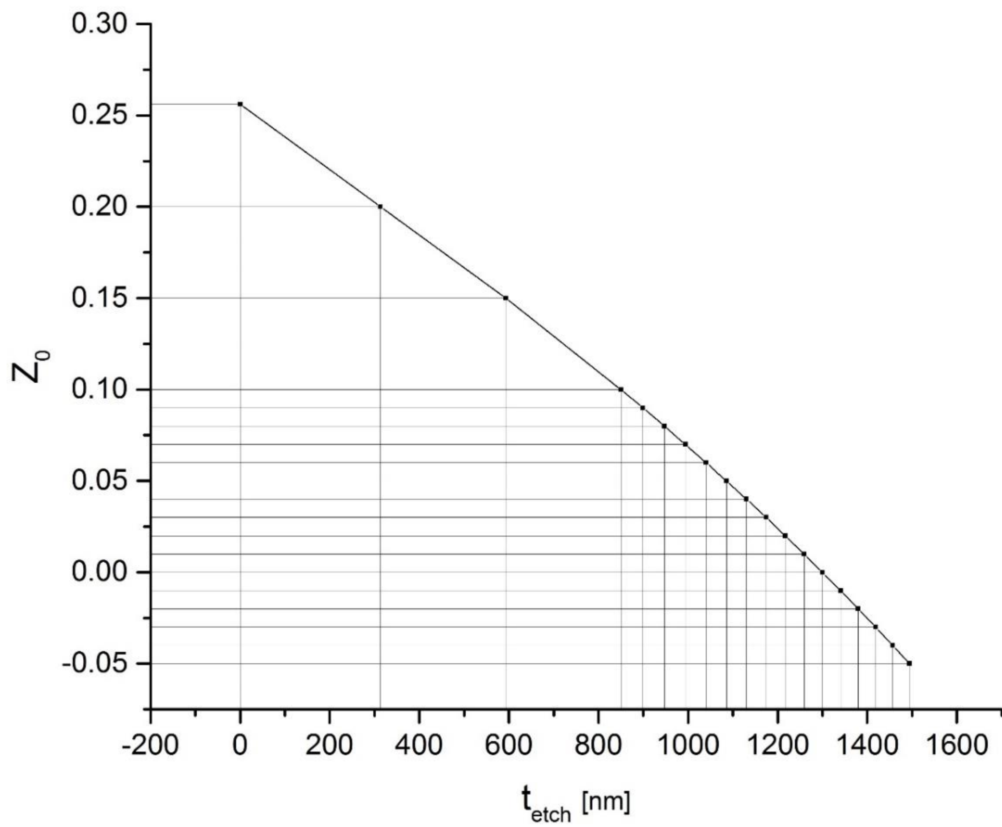

Fig. 25: Plot of Z_0 vs thickness of silicon nitride to be etched for wafer 63236.

2.2.3 Estimating the Reynolds number β

Equation **7** can be used to calculate the Reynolds number for the resonator designed in this work. First, a mixture of water and glycerol was considered, as it was used in [30]. Besides the properties of the fluid (density and shear viscosity), the angular velocity of the cantilever vibration (ω) and the channel thickness are needed to calculate β. The fluid properties of a mixture of water and glycerol can be found in the literature [31], while ω is related to the resonance frequency by the equation below.

$$\omega = 2\pi f_0 \tag{10}$$

The resonance frequency for different mixtures of water and glycerol was simulated using COMSOL Multiphysics software and the designed dimensions of the channel and cantilever. Table **3** lists the fluid properties at 20 °C and the simulated resonance frequency for different glycerol-water solutions considering the four different resonators (channels have four different lengths). From Table **3**, it can be inferred that viscosity is the parameter that changes the most when changing the percentage of glycerol in a glycerol-water solution. Table **4** displays the expected values of β for the designed resonators. It is important to note that the channel thickness used was the one designed (6 µm), but in reality, this value is slightly smaller and depends on the wafer, as discussed in the last section.

Using a glycerol-water mixture enables the viscosity and β to be varied over three orders of magnitude. It is also possible to achieve larger values of β using less viscous fluids, such as acetone and diethyl ether.

Table 3: Simulated frequency of the four resonators for different glycerol-water solutions.

Glycerol (%)	**Density (g/cm³)**	**Viscosity (mPa·s)**	**Frequency (kHz)**			
			250 µm channel	**500 µm channel**	**750 µm channel**	**1000 µm channel**
0	0.99823	1.005	173.31	46.87	21.05	11.893
10	1.0221	1.31	172.34	46.684	20.967	11.846
20	1.0469	1.76	171.32	46.493	20.883	11.799
30	1.0727	2.5	170.29	46.297	20.796	11.750
40	1.0993	3.72	169.23	46.098	20.708	11.700
50	1.1263	6	168.17	45.899	20.62	11.650
60	1.1538	10.8	167.11	45.698	20.531	11.600
70	1.18125	22.5	166.06	45.501	20.443	11.551
80	1.2085	60.1	165.04	45.307	20.357	11.502
90	1.2351	219	164.05	45.120	20.275	11.455
95	1.24825	523	163.57	45.028	20.234	11.432
100	1.26108	1410	163.10	44.939	20.195	11.410

Table 4: Reynolds number of the four different resonators for glycerol-water solutions.

Glycerol (%)	β			
	250 µm channel	**500 µm channel**	**750 µm channel**	**1000 µm channel**
0	38.94	10.53	4.73	2.67
10	30.41	8.24	3.70	2.09
20	23.05	6.25	2.81	1.59
30	16.53	4.49	2.02	1.14
40	11.31	3.08	1.38	0.78
50	7.14	1.95	0.87	0.49
60	4.04	1.10	0.49	0.28
70	1.97	0.54	0.24	0.13
80	0.75	0.20	0.092	0.052
90	0.21	0.057	0.025	0.014
95	0.089	0.024	0.011	0.0062
100	0.033	0.0091	0.0041	0.0023

3 Fabrication

The objective of the microfabrication process was to obtain suspended microchannel resonators with different values of channel off-axis placement. This was achieved by etching the low stress silicon nitride layer on top of the microchannel, and by releasing the structures.

Figure **26** depicts the process flow conducted during this work. All the steps were performed in the cleanroom of the Center of Micronanotechnology (CMi) at École Polytechnique Féderale de Lausanne (EPFL). The first step is a photolithography process in order to define a central window around the resonators. Prior to the next step, the wafers are cleaved into chips. Step 2 is a dry etching process on the chips to obtain different values of channel off-axis placement, followed by the removal of the photoresist (PR). Step 3 is a second photolithography process in order to define the cantilevers and the inlets. Finally, steps 4 and 5 are dry etching processes to release the structures, followed by another photoresist removal. In the upcoming sections, the steps will be explained in detail. The main issues faced during the fabrication processes are also reported. All the steps with the equipment, parameters and recipes used are summarized can be found in appendix A.

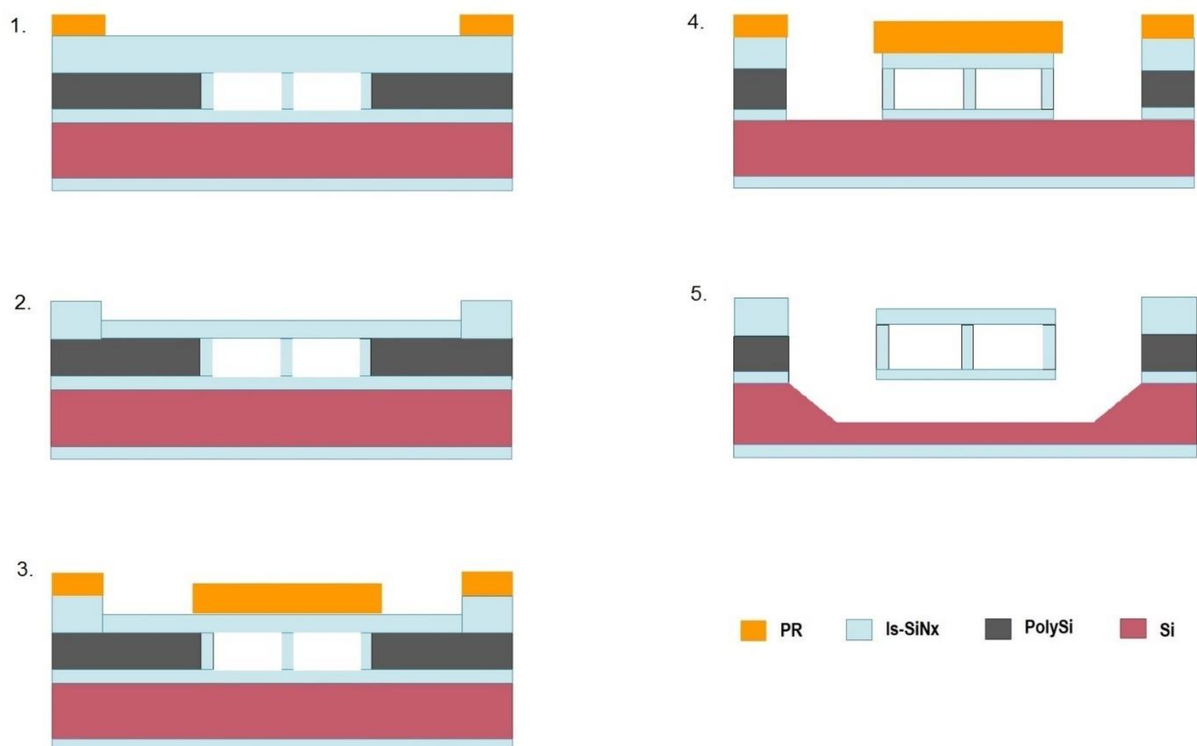

Fig. 26: Representation of the microfabrication process.

3.1 Central window definition - First photolithography

Photolithography is a patterning process that transfers geometrical forms on a mask to a substrate. It uses UV-light to transfer the pattern to a light sensitive chemical (photoresist) on top of the substrate. The photolithography is comprised of three main steps: spin coating, exposure and development (photoresist removal). The ACS200 Gen3, an automated tool, was used for the photoresist coating and development. The three wafers were coated with 5 µm of the positive photoresist AZ ECI 3027, using the program 0129 of the ACS200 Gen3. This program consists of a Hexamethyldisilane (HMDS) treatment, spin coating at 1200 rpm and a soft bake at 100 °C for 2.5 minutes. The HMDS treatment promotes good photoresist-to-wafer adhesion, while the softbake evaporates the excess of photoresist solvent.

This first photolithography aims to define a window around the resonators. This is needed for the subsequent etching process. Instead of etching the whole area of the chip making the device very fragile, only the area of interest, inside this window, is etched. This photolithography also delimitates the area of each chip. On figure **27** the mask design, created in CleWin 4, is illustrated. The central window has a dimension of 1.57 x 1.55 mm. The features on the sides of the mask design are alignment marks which help the alignment of the mask with the layer already present on the wafer during the exposure.

The exposure was performed on the MLA 150, a maskless aligner. This tool uses a continuous semiconductor laser-diode emitting at 405 nm which is focused on the wafer using a single writehead. The mask design file generated by the CleWin (.cif) was converted into the tool's standard format using the high quality mode. The two parameters of exposure are dose and defocus. The dose controls the intensity of the laser beam while the defocus defines the location of the camera focus. A dose of 230 mJ/cm^2 and a defocus of -3 were used. As the photoresist is positive, exposure to the UV-light changes its chemical structure in such a fashion that it becomes soluble and can be washed away during development.

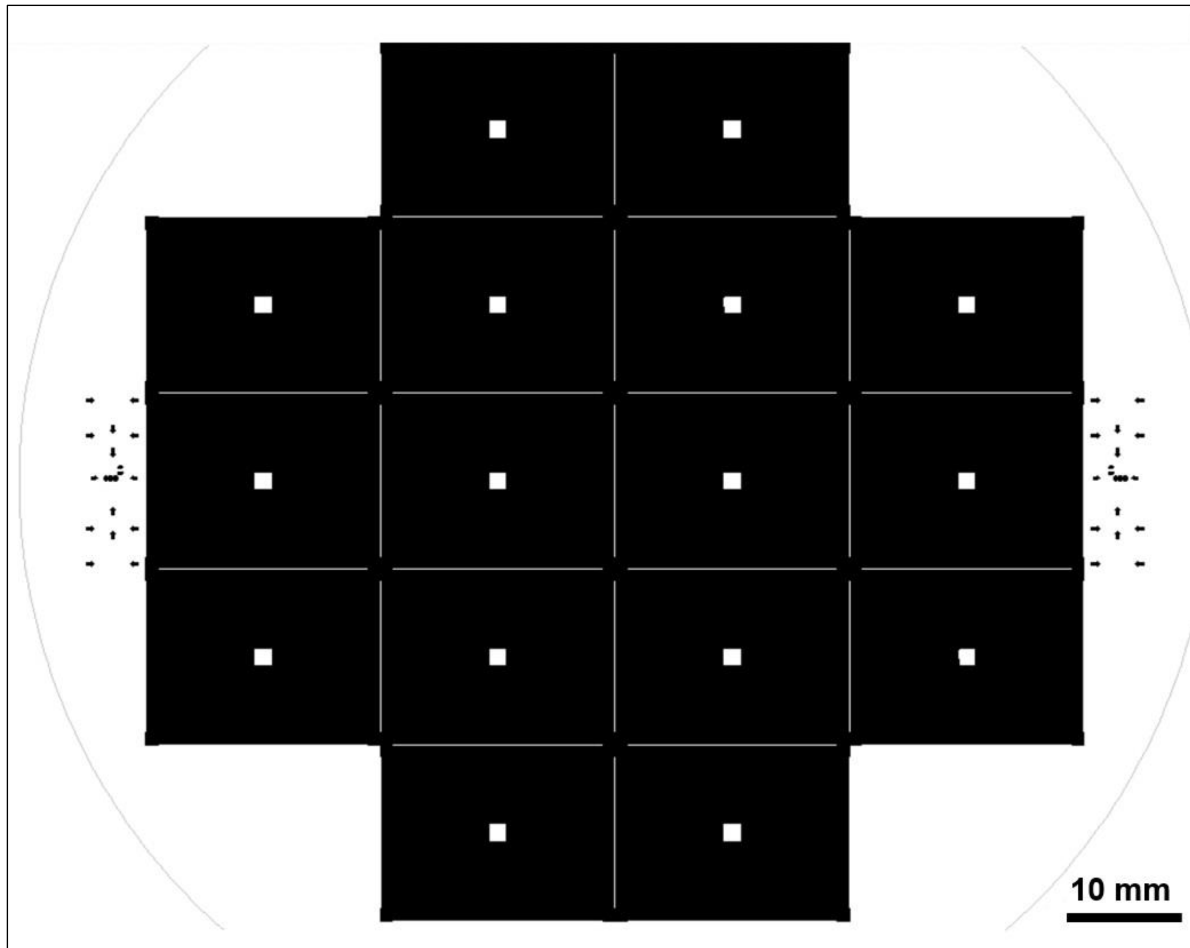

Fig. 27: First mask design showing the central window and area of each chip. Image from CleWin.

The development was carried out on the ACS200 Gen3 with the program 0929. The developer used for the resist AZ ECI 3027 was the AZ 726 MIF.

Prior to the next fabrication step, the wafers were cleaved into chips. A pen with a diamond tip was used to scratch the wafers, with the help of tweezers to bend and cleave them. The cleavage is a critical step, because if not done carefully, the channels could be permanently damaged. As this is a manual process, the chips vary slightly in size.

After the development, the wafers were inspected at the Optishot 200 optical microscope. Figure **28** illustrates the successful cross alignments achieved on wafer 63238. Figure **29** shows the photoresist features on chip 11 of wafer 63238. Wafers 7304 and 63236 exhibited similar

results.

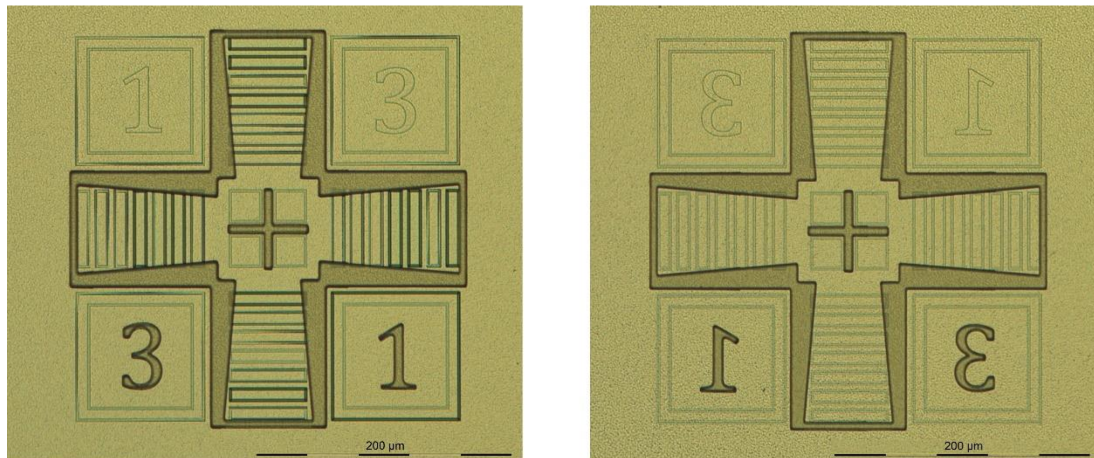

Fig. 28: Successful alignment of the first mask to the layer already present on wafer 63238 (3 to 1 alignment marks). Left cross and right cross pictures taken with the Optishot microscope with a magnification of 20x

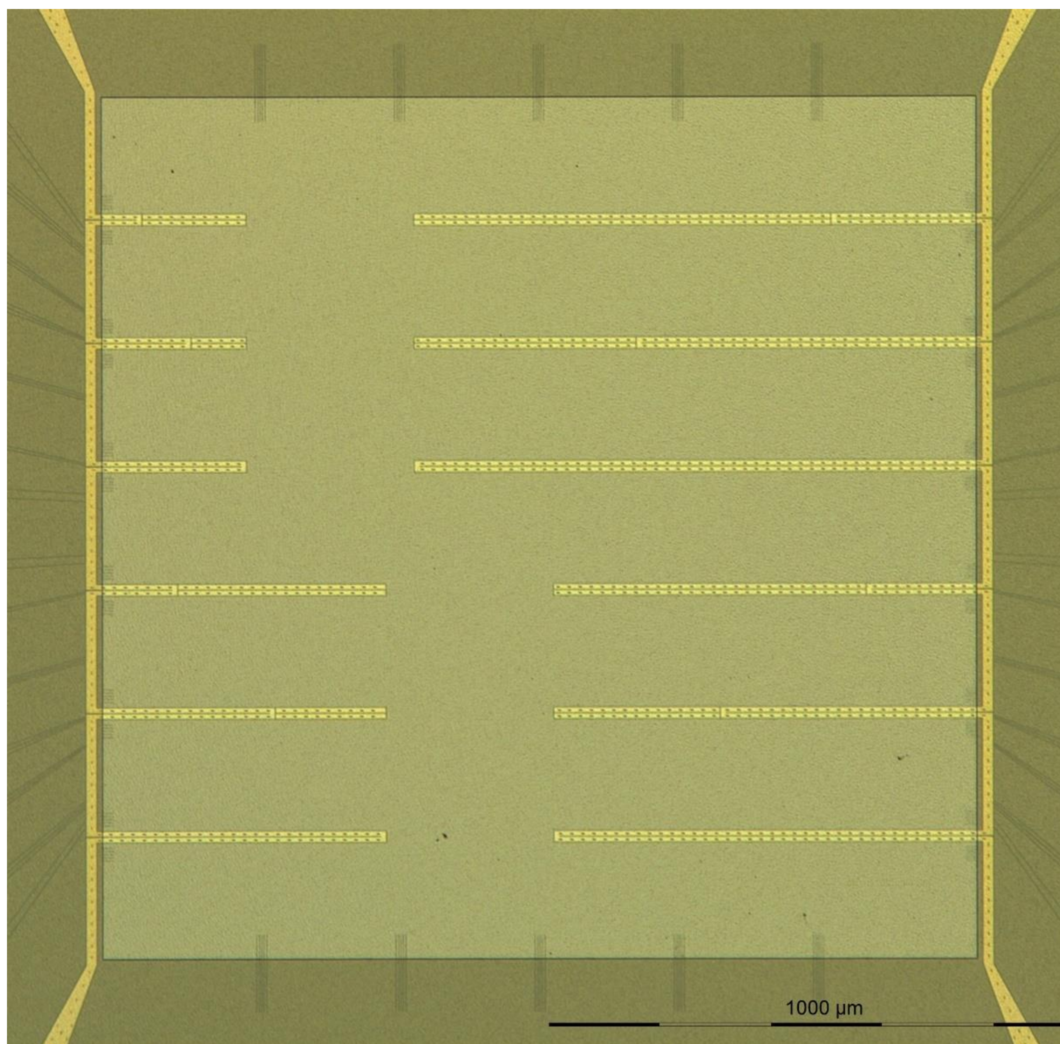

Fig. 29: Chip 11 after development. Image taken with Optishot microscope with a magnification of 5x.

3.2 Top silicon nitride etching and photoresist strip

Before the etching (removal) of the top layer of silicon nitride, the chips had to be attached to carrier wafers. The carriers are 4-inch silicon wafers provided by CMi. QuickStick^{TM} 135, a temporary mounting wax, was used to glue the chip on top of the carrier wafer. This wax is solid at room temperature. For the bonding, a hotplate at 135°C is needed. At this temperature, the QuickStick melts and the chip can be glued to the wafer. After a short time, within a few seconds, the wafer can be removed from the hotplate. Each chip was attached to the center of a carrier wafer. To ensure a good bonding and thermal conductivity between the chip and the wafer, it is important to guarantee that the whole area on the back of the chip is covered with glue and that the layer of glue is thin. To achieve that, the corners of the chips, were pressed with the help of tweezers, while the wafer was on the hotplate. After bonding, the excess of wax on the wafer was removed with a foam swab embedded in acetone.

The etching was carried out in the SPTS Advanced Plasma System (APS) machine. This tool is a dry etcher dedicated to dielectrics such as silicon dioxide and silicon nitride. The system is based on a high density plasma source and uses a mixture of gases to perform the etching. Prior to the etching of the chips, tests were conducted to confirm the etch rate for silicon nitride and photoresist. Two 4-inch test wafers, one coated with low-stress silicon nitride and the other with photoresist (AZ ECI 3027) were used for the tests. The program selected in the SPTS tool was "*Si_3N_4 smooth*" that uses a mixture of trifluoromethane (CHF_3) and sulfur hexafluoride (SF_6), and the time of the process was two minutes. To determine the etch rate, the thicknesses of silicon nitride and photoresist were measured before and after the etching using the Nanospec tool, a film thickness measurement system. Table **5** shows the etch rates found in comparison with the rates provided by the CMi staff. The selectivity of silicon nitride with respect to photoresist was found to be approximately 2:1.

Table 5: Etch rates for silicon nitride and photoresist with recipe Si_3N_4.

Material	**Recipe**	**Etch rate measured**	**Etch rate (CMi)**
Silicon nitride	Si_3N_4 smooth	200 nm/min	160 - 220 nm/min
Photoresist	Si_3N_4 smooth	90 nm/min	80 nm/min

With the value of the etch rate for the silicon nitride and the graphs of Z_0 as function of thickness of silicon nitride from section 2.2.2, the time of the etching process could be easily calculated.

The first chips processed were chips 7, 8, 11 and 12 of wafer 63238. Table **6** lists the parameters used for the etching as well as the expected Z_0 for each chip. Chip 7 was not etched.

Table 6: Etching parameters and desired Z_0 for the first four processed chips.

Chip ID	**Recipe**	**Time (min)**	**Expected thickness etched (nm)**	**Z_0**
7	-	-	-	0.2
11	Si_3N_4 smooth	2	400	0.1
12	Si_3N_4 smooth	3	600	0.05
8	Si_3N_4 smooth	4	800	0

Once the etching was finished, the photoresist needed to be stripped off. This was carried out using two different processes: a high frequency oxygen plasma – Tepla Gigabatch tool – and wet etching (Shipley remover 1165). These two processes are needed because during the previous dry etching, the surface of the photoresist becomes very hard. Using only the wet etching would take a lot of time to remove all the photoresist.

The wafers with the chips attached were placed, one by one, inside the plasma stripper in high power oxygen plasma for 3 minutes, using the recipe *"PR_Strip_High"*. Then, they were transferred to the wet bench. The wet bench consists of four baths, two containing the remover Shipley 1165 and the other two filled with distilled water, for rough and fine rising. Figure **30** illustrates the four baths and the process sequence. The wafers were immersed for 10 minutes in the baths filled with the photoresist remover at 70°C (5 minutes in each bath) followed by an immersion in the fine rising tank (cascade tank) for 6 minutes. The rough rising, known as quick dump rinse was skipped as it could damage the microchannels. The wafers were left for drying in air, and then placed again inside the plasma stripper in low power oxygen plasma for 3 minutes, using the recipe *"PR_Strip_Low"*. This last process was carried out to ensure that all traces of photoresist were removed.

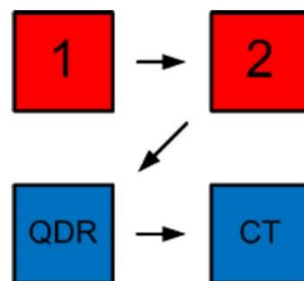

Fig. 30: Schematic of the wet bench. Baths 1 and 2 filled with remover Shipley 1165; QDR: Quick Dump Rise (rough rinsing), CT: Cascade Tank (fine rinsing). QDR was skipped [32].

Before proceeding to the second photolithography, the thickness of silicon nitride etched was measured for each chip using the Bruker Dektak XT, a mechanical profilometer. Figure **31** illustrates one of the measurements performed. To check the thickness etched, the step was measured between the areas inside and outside of the central window. The former is where the etching took place, and the latter was the area protected with photoresist during the etching.

Table **7** shows the results of the thickness of silicon nitride etched for chips 8, 11 and 12 measured with the profilometer. At least three measurements were performed for each chip and the average was calculated.

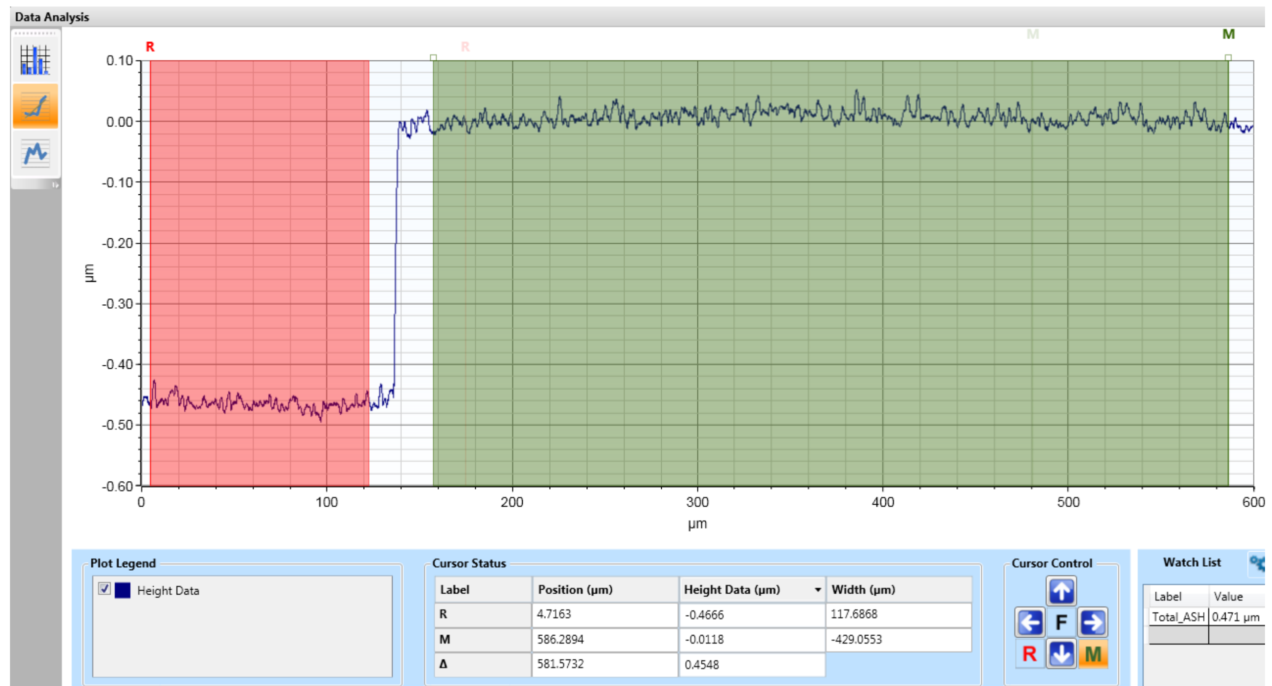

Fig. 31: Measurement of the thickness etched on chip 12. A step of 455 nm was measured. The expected value was 600 nm.

Table 7: Comparison between the expected and the actual thickness of silicon nitride etched

Chip ID	Expected thickness etched (nm)	Actual thickness etched (nm)
11	400	420
12	600	460
8	800	550

As shown in Table **7**, the actual thicknesses etched for chips 8 and 12 were far from the value expected. When investigating the reasons for this difference, it was found that the etch rate for the recipe *"Si_3N_4 smooth"* used in the SPTS APS tool is load-dependent, i.e. the etch rate is inversely proportional to the amount of exposed material being etched. Moreover, this recipe

etches silicon two times faster than silicon nitride. As the carrier wafers used were silicon wafers, the SPTS tool etched also the silicon of the wafer, strongly affecting the etch rate of the silicon nitride on top of the chips.

The next two chips of wafer 63238 (IDs: 6 and 10) were then etched using a different recipe to obtain new values of Z_0. The recipe *"SiO_2 PR 2:1"* was used. This recipe is based on a mixture of Helium (He) and Octafluorocyclobutane (C_4F_8) and etches a very small amount of silicon compared to silicon nitride. After etching, the photoresist was stripped and the thickness of silicon nitride etched was measured in the same fashion as explained above for the first four chips. Table **8** lists the thickness etched for chips 6 and 10, after measurements with the mechanical profilometer.

Table 8: Etching parameters and measurements for chips 6 and 10

Chip ID	Recipe	Time (min)	Thickness etched (nm)	Z_0
6	SiO_2 PR 2:1	7	600	0.05
10	SiO_2 PR 2:1	9	800	0

3.3 Cantilever and inlets definition - Second photolithography

The second photolithography aims to define the cantilevers and the inlets on each chip. Different from the first photolithography, the surface preparation and the coating were not carried out in the automated tool ACS200 Gen 3. As this second photolithography is at chip level, a manual coater was preferred. Before the coating, a HMDS treatment was carried out using the tool ATMsse OPTIhot VB20 (see Figure **32**). The recipe *"HMDS standard"* was used for all chips. Following, coating was performed in the manual coater ATMsse OPTIspin SB20. (see Figure **33**). The photoresist AZ ECI 3027 was dispensed with a pipette, covering the whole area of the chip. Based on the spin curve of the AZ ECI 3027, the recipe *"STD-1200-RPM"* was selected to achieve a thickness of 5 µm (see Figure **34**). After coating, softbake was performed in a hotplate at 90°C for 3 minutes.

Fig. 32: ATMsse OPTIhot tool used for surface preparation [33].

Fig. 33: ATMsse OPTIspin used for coating. The hotplate used for softbake is on the right [34].

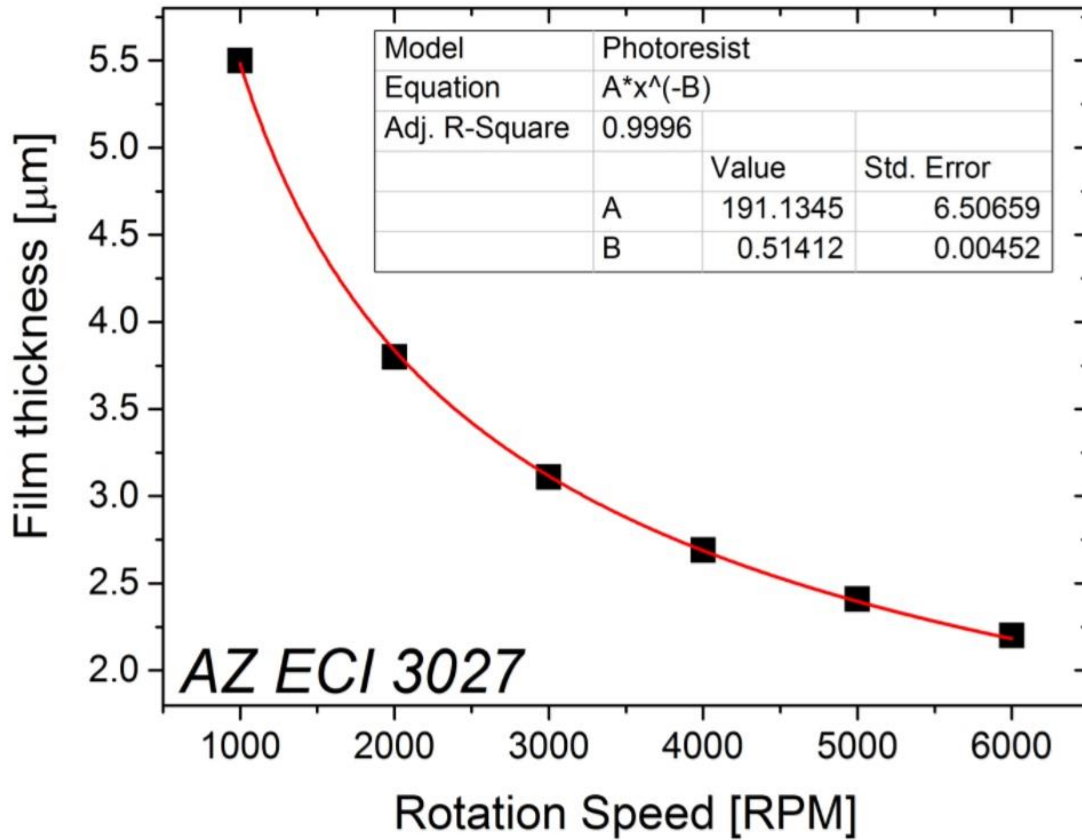

Fig. 34: Spin curve of the photoresist AZ ECI 3027. A rotation speed of 1200 rpm is needed to achieve a film thickness of 5 µm [35].

The exposure was performed using the MLA 150. The mask designs were converted to the tool's standard file using the high-quality mode. Figure **35** shows the mask design layer for the chip with 12 cantilevers. The mask for the other type of chip can be seen in Figure **36.** The features on the sides of the masks are alignment marks to help the alignment with the previous layer. The parameters of exposure were an optimized dose of 350 mJ/cm^2 and a defocus of -3.

The development was performed manually, using a beaker filled with developer AZ 726 MIF. The wafers were immersed in the beaker for 3 minutes and then rinsed with deionized water. After that, they were left for drying in air.

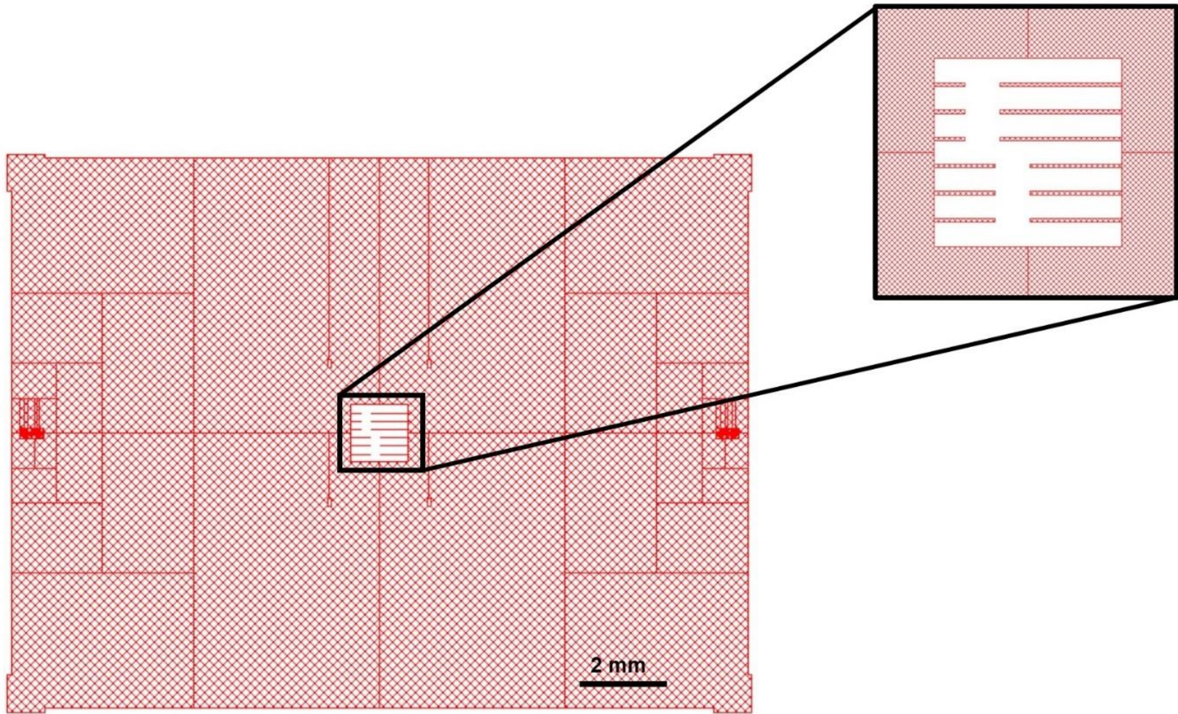

Fig. 35: Design mask for the second photolithography process for chips with 12 cantilevers. Inset shows the cantilevers in detail. Image from CleWin.

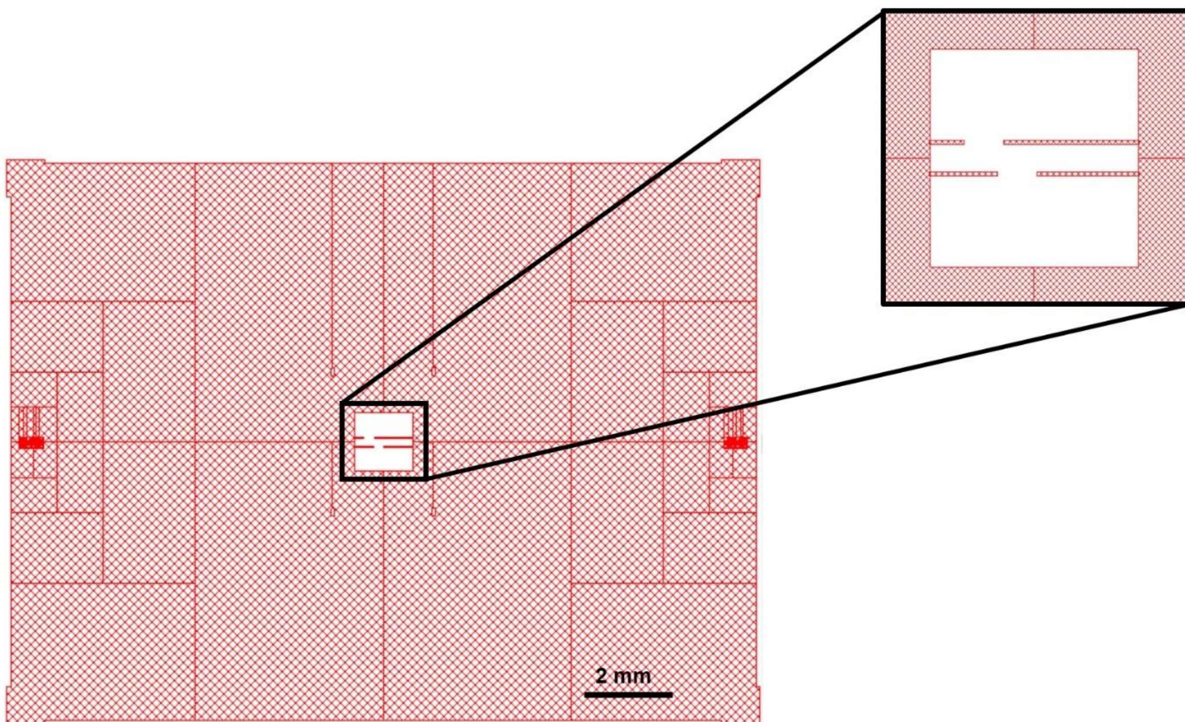

Fig. 36: Design mask for the second photolithography process for chips with 4 cantilevers. Inset shows the cantilevers in detail. Image from CleWin.

After the development, the chips were inspected at the Optishot 200 optical microscope. Figure **37** and Figure **38** shows respectively chip 12 and chip 10 after the photolithography process. Figure **39** compares the feature sizes of an inlet on chip 10 with the CleWin design. It can be noticed that the dimensions of the inlet correspond to the ones from the design. The inlet is also well centered with respect to the channel. The critical features, however, are the photoresist areas that will protect the cantilevers during the release. Figure **40** compares the results for these features on chip 12 with the CleWin design. A small misalignment can be observed. As the area entirely covers the channel, this misalignment is not a problem for the following fabrication step.

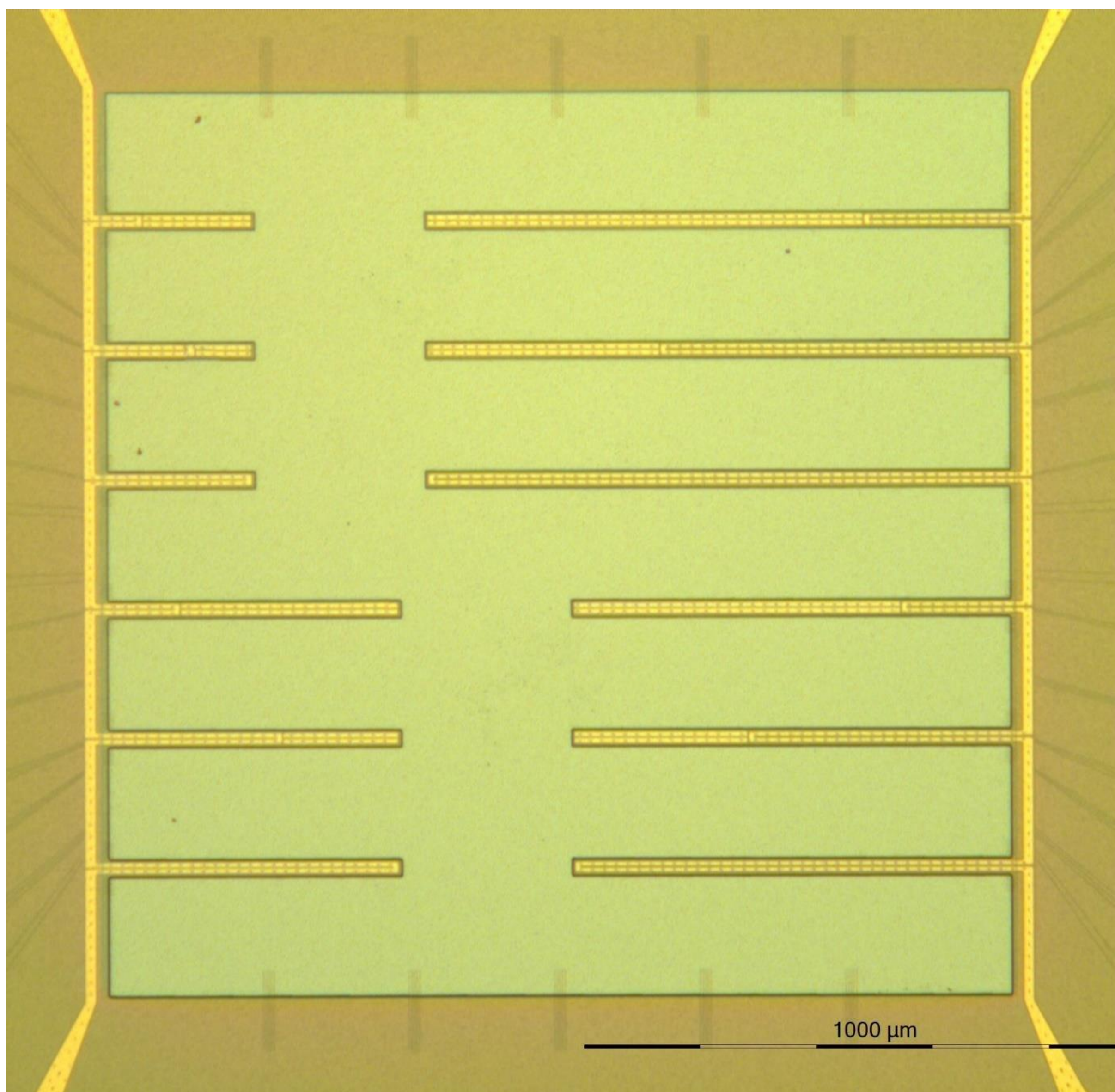

Fig. 37: Chip 12 after the development. Image taken with the Optishot microscope with a magnification of 5x.

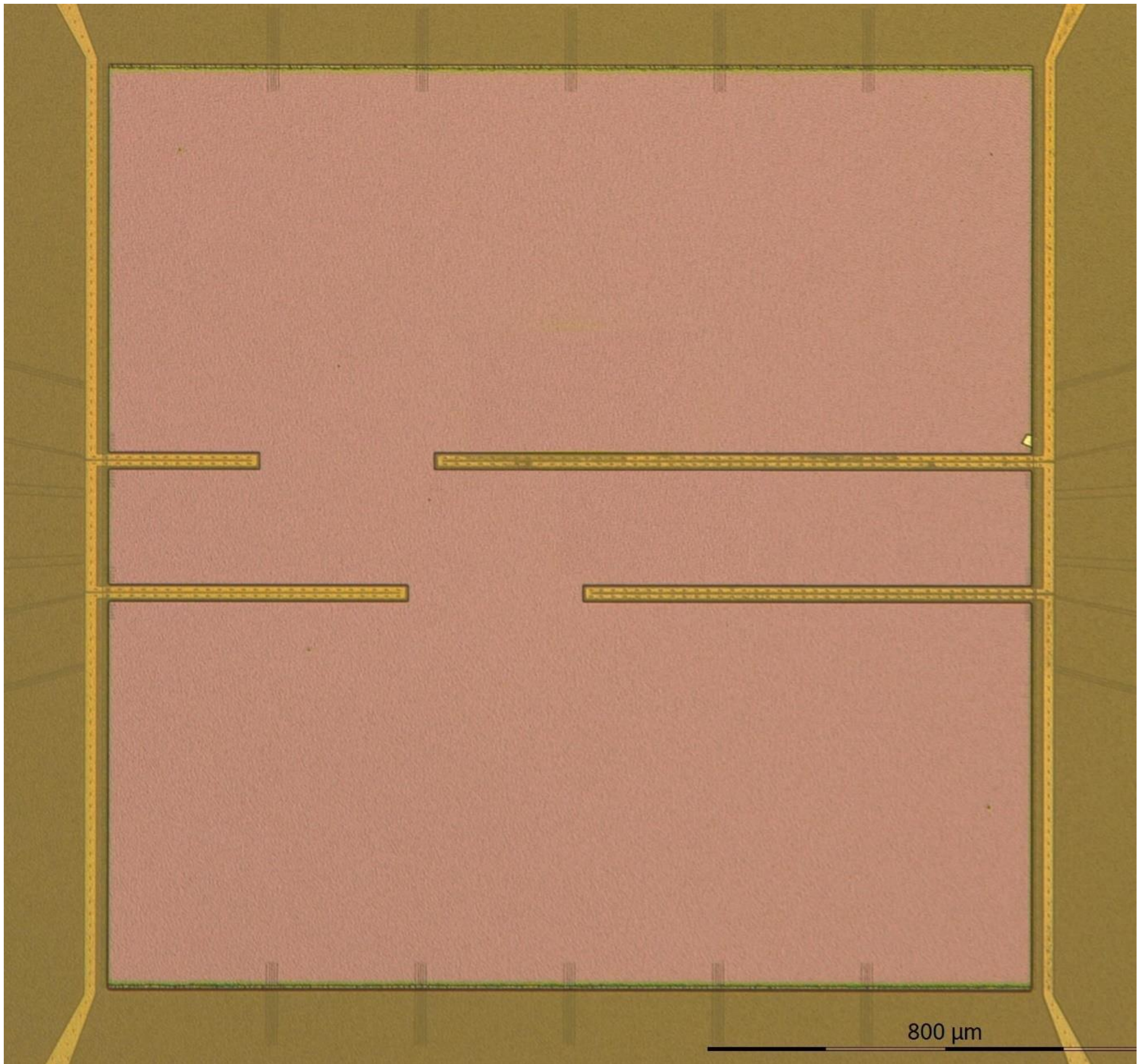

Fig. 38: Chip 10 after the development. Image taken with the Optishot microscope with a magnification of 5x.

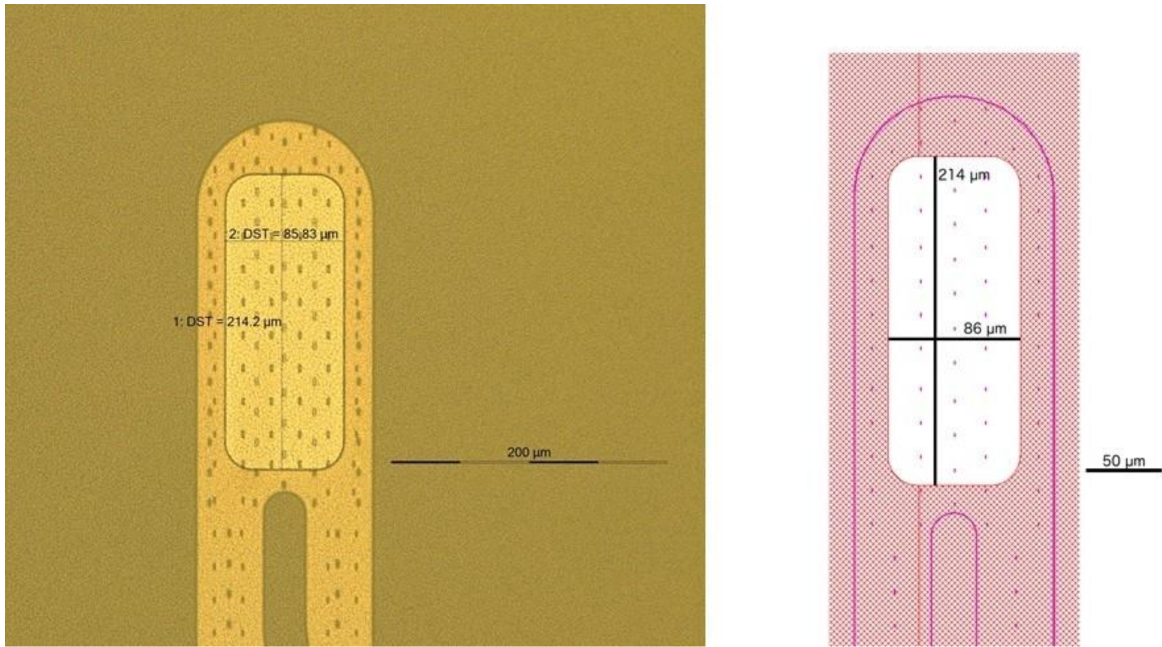

Fig. 39: Comparison between the photoresist features of an inlet on chip 10 (left) and the CleWin design (right). Image on the left was taken with the Optishop microscope with a magnification of 20x.

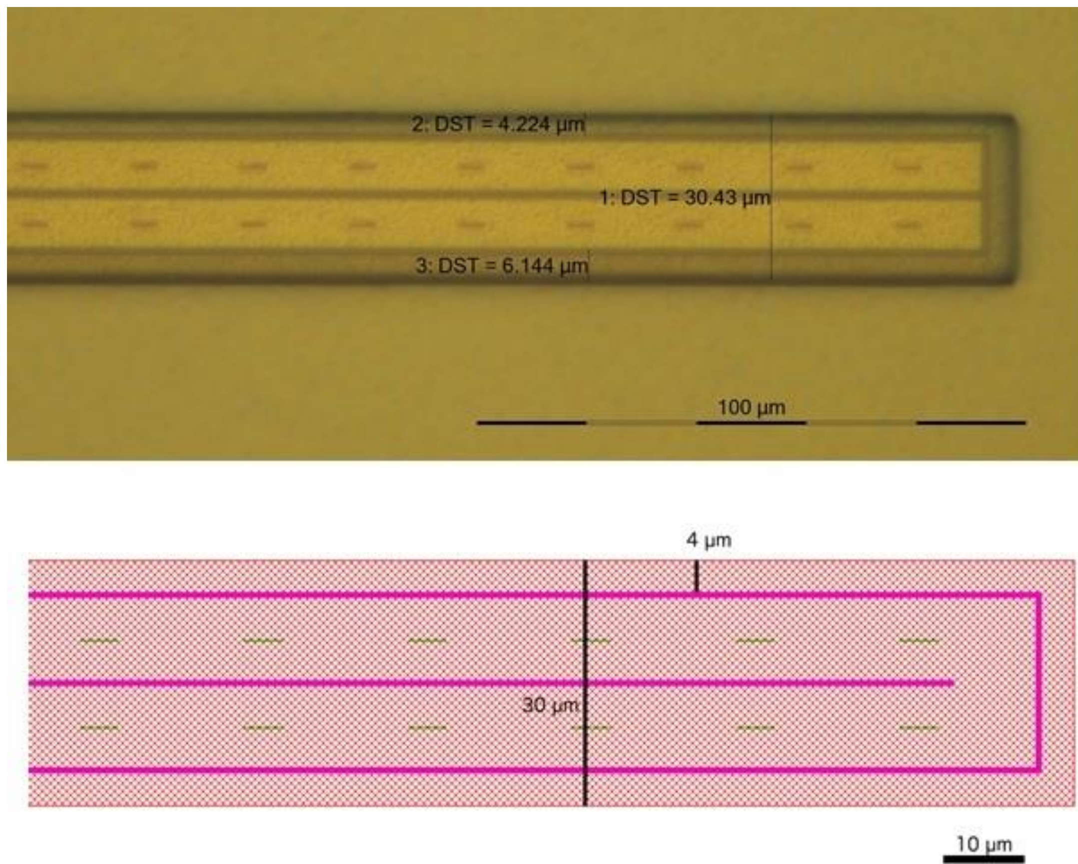

Fig. 40: Comparison between photoresist area on top of a cantilever on chip 12 (top) and the CleWin design (bottom). Image on top was taken with the Optishot microscope with a magnification of 50x.

3.4 Cantilever release and inlet opening

The last steps of the microfabrication were dry etching processes to release the cantilevers and open the inlets. As shown in the process flow in Figure **26**, the top layer of silicon nitride, the polysilicon layer and the bottom layer of silicon nitride need to be removed prior to the isotropic etching of the bulk silicon. The etching processes were performed in the Alcatel AMS 200, an optimized Deep Reactive Ion Etching (DRIE) system for silicon and silicon on insulator wafers.

Three different processes were used for the different layers. A continuous C_4F_8-based anisotropic etching process, labelled as *"SiO2 PR 1:1"*, was performed to remove the top and bottom layers of silicon nitride. To remove the polysilicon layer, a Bosch process was used. The Bosch process is a pulsed etching that alternates repeatedly between two steps: an active SF_6-based etching process and a deposition of a passivation layer, using C_4F_8. Each step lasts a few seconds. The process named "*SOI_ACC_ADP"* was the one used in this work, in which the SF_6-based step lasts 6 seconds, while the C_4F_8-based step lasts 2 seconds. The third process is a SF_6-based silicon isotropic etching named "*Si_release*". The etch rates for the three processes are listed in Table **9**. It was important to monitor the etching of the photoresist, to avoid its total removal.

Table 9: Etching rates for processes used in AMS 200

Recipe	**Etch rate**	**Selectivity to photoresist**
SiO2 PR 1:1	280-320 nm/min	1:1
SOI_ACC_ADP	3-4.5 µm/min	75:1
Si_release	2 µm/min in lateral 4 µm/min in vertical	100:1

With the etch rates and knowledge of the thickness of each layer, the time for each process could be easily estimated. For all the chips, the duration of the processes was the same, except for the etching of the top layer of silicon nitride, which varied from chip to chip. Table **10** summarizes the process carried out in the AMS 200. Between each step the chips were observed under an optical microscope to check the removal of the layers. A difference in color, that could be observed with naked eyes, would also indicate the layer removal, since silicon and polysilicon have a characteristic grey color. For removing the bulk silicon, a Bosch process is performed before the isotropic silicon etching, to help the penetration of SF_6, accelerating the

release of the cantilevers.

Table 10: Etching steps carried out to release the cantilevers

Layer	Recipe	Time (min)
Top silicon nitride	SiO2 PR 1:1	3 - 5
Polysilicon	SOI_ACC_ADP	2
Bottom silicon nitride	SiO2 PR 1:1	2
Silicon	SOI_ACC_ADP	3
	Si_release	5

After etching, the resist was stripped off. Combining wet etching and high frequency oxygen plasma, as performed before, was not advisable this time, as immersing the chips in baths could cause the collapse and stiction of the released cantilevers. Only the Tepla Gigabatch was used. Two steps of 3 minutes of the recipe *"PR_Strip_High"* were performed to remove all the photoresist deposited of the chips. Figure **41** shows chip 11 after the removal of the resist.

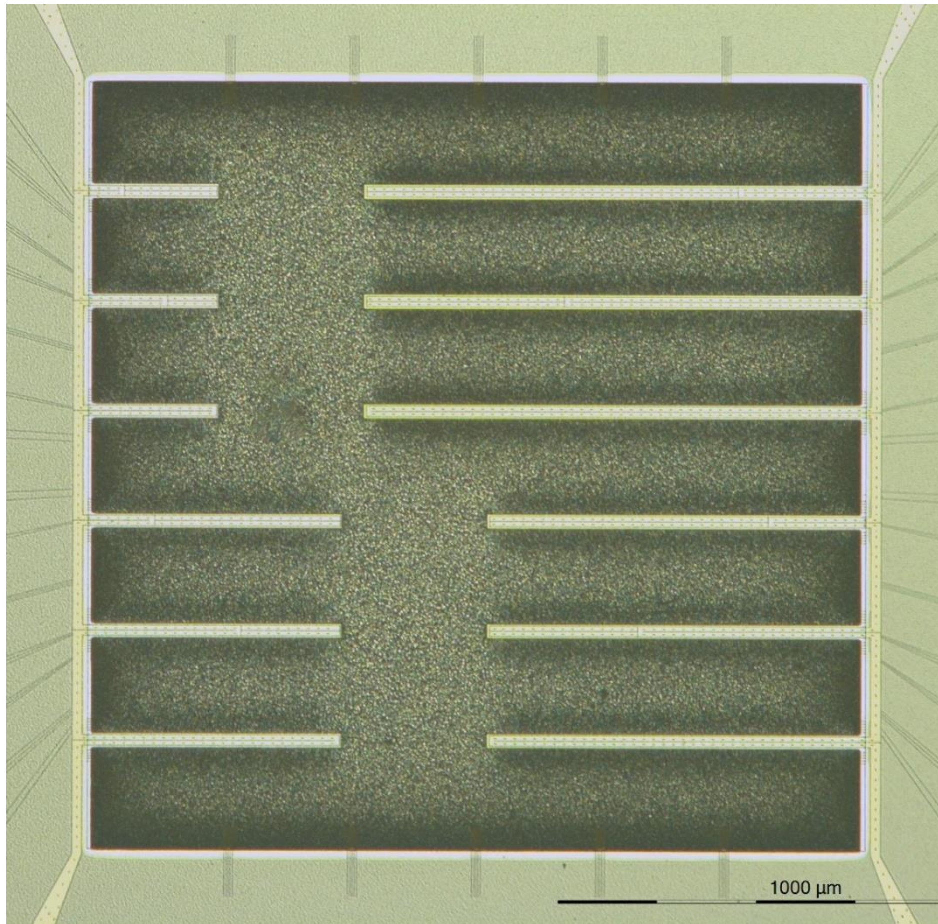

Fig. 41: Chip 11 after photoresist strip, showing the released cantilevers. Image taken with Optishot microscope with a magnification of 5x.

Finally, the chips were detached from the carrier wafers and observed with the SEM (Zeiss Leo 1550). A hotplate at 135°C was used for melting the QuickStick and detach the chip from the wafer. Figure **42** shows a SEM picture of chip 11. The two inlets openings at the bottom can be seen. Figure **43** illustrates the area of the cantilevers with a higher magnification. The cantilevers are very flat and all of them were released. Figure **44** shows one of the inlets of chip 11. The clamp and the tip of the one cantilever are shown respectively in Figures **45** and Figure **46**. It can be observed that the cantilever is not very sharp at the clamping, indicating that the second photolithography could be improved.

Figure **47** illustrates a SEM picture of chip 10, in which the four released cantilevers can be observed.

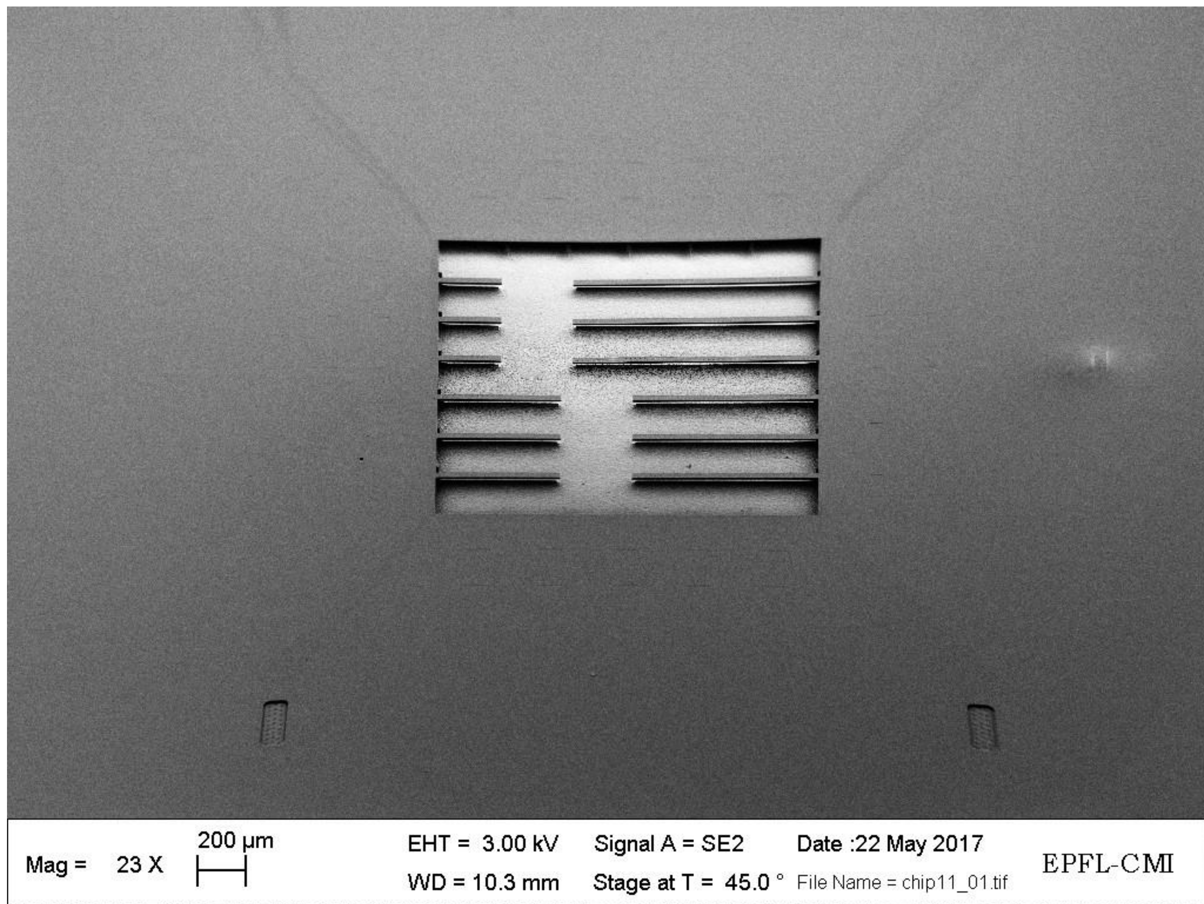

Fig: 42: Chip 11 after photoresist stripping. Image taken with the SEM.

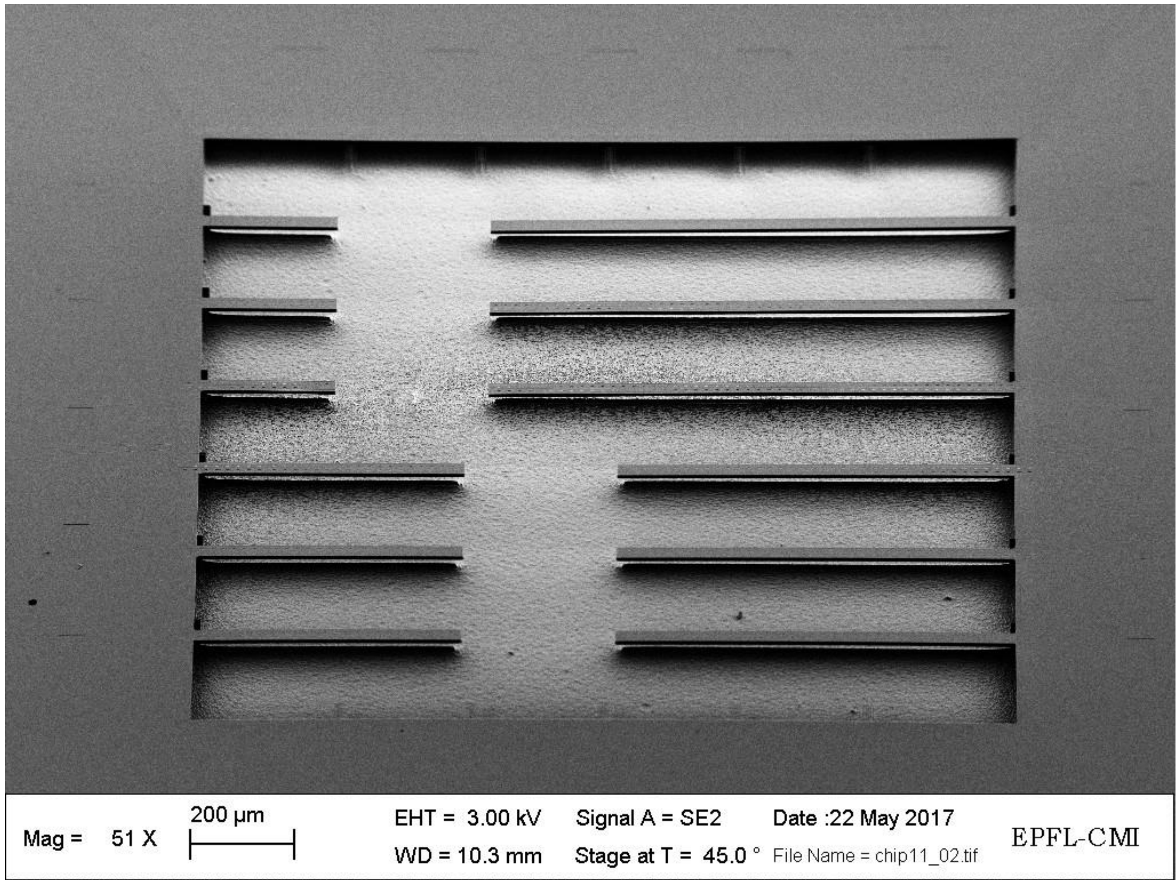

Fig. 43: Released cantilevers of chip 11. Image taken with the SEM.

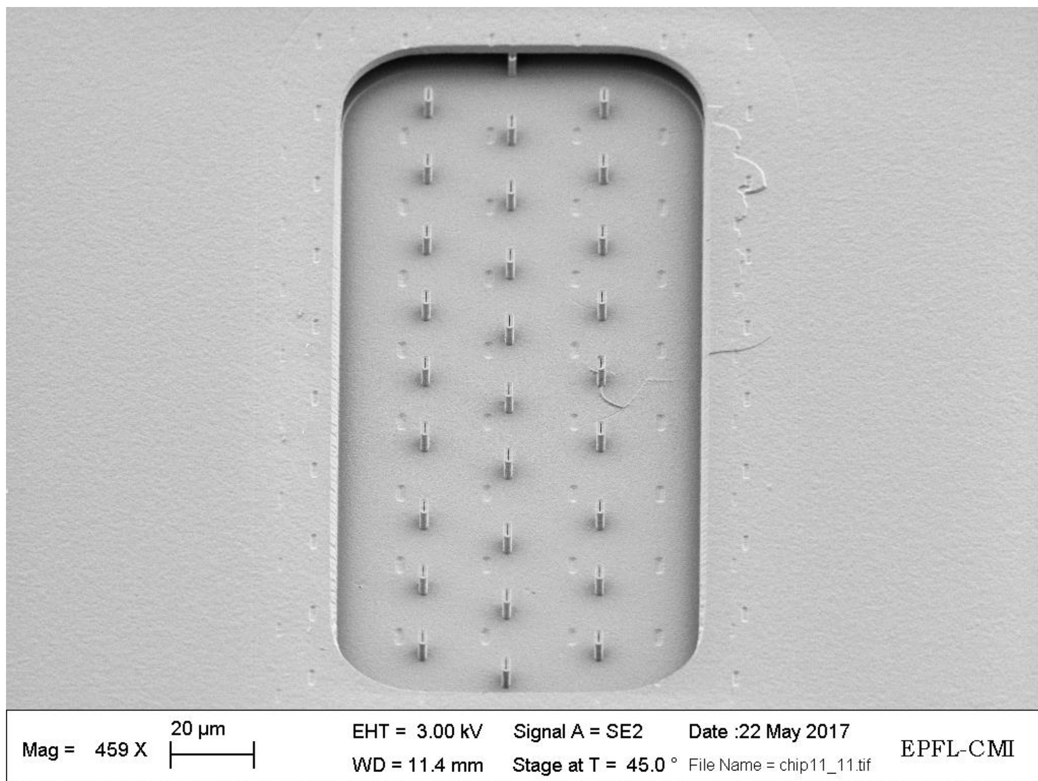

Fig. 44: Inlet opening of chip 11. Pillars and apertures from previous microfabrication processes can be seen. Image taken with the SEM.

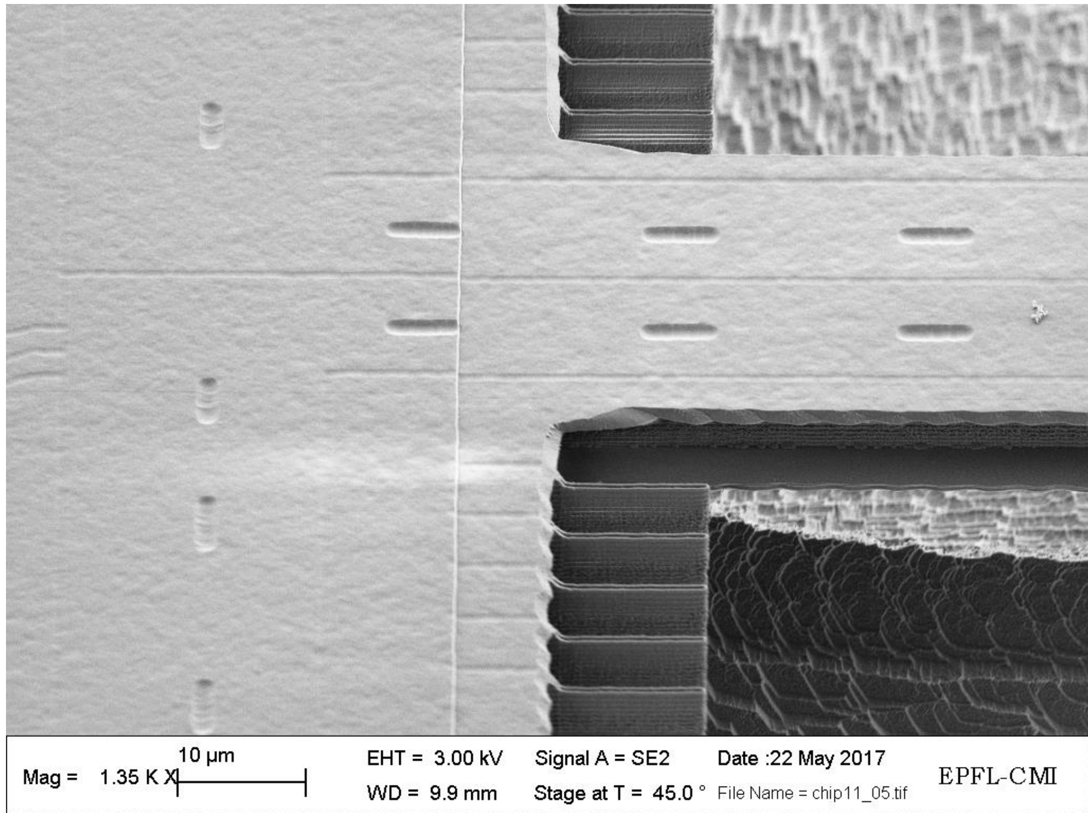

Fig. 45: Zoom at the clamping of a cantilever of chip 11. Image taken with the SEM.

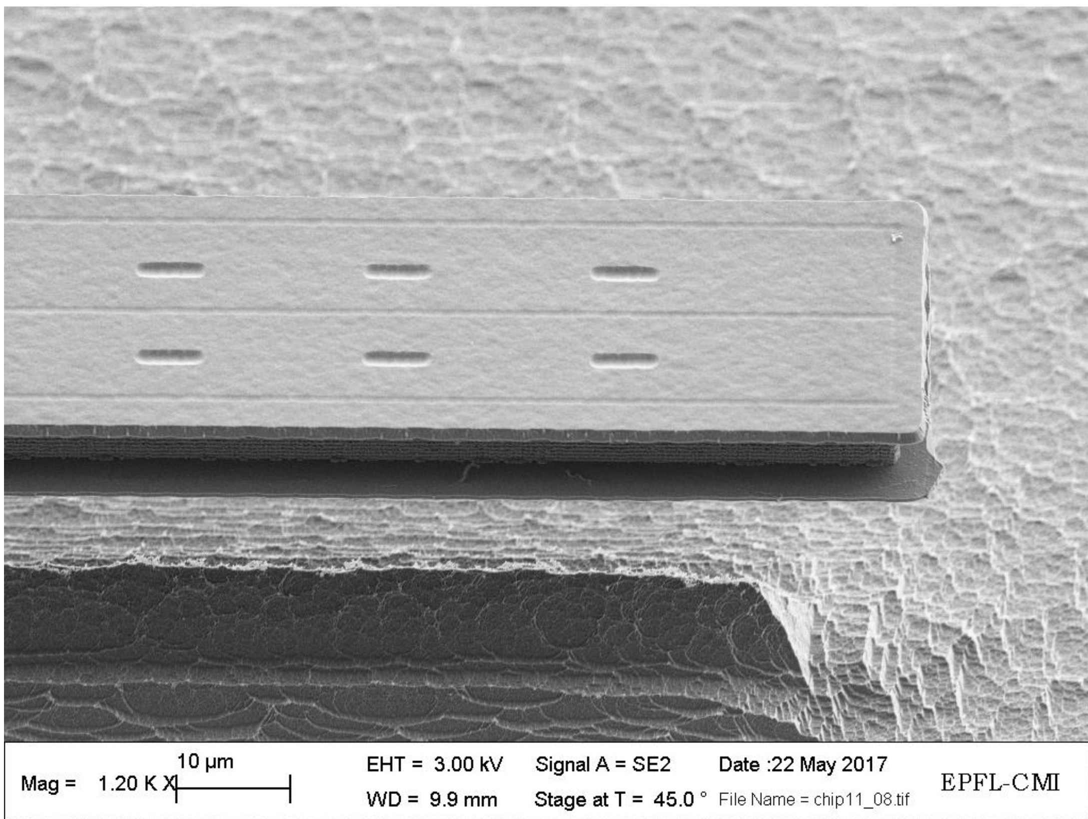

Fig. 46: Zoom at the tip of a cantilever of chip 11. Image taken with the SEM.

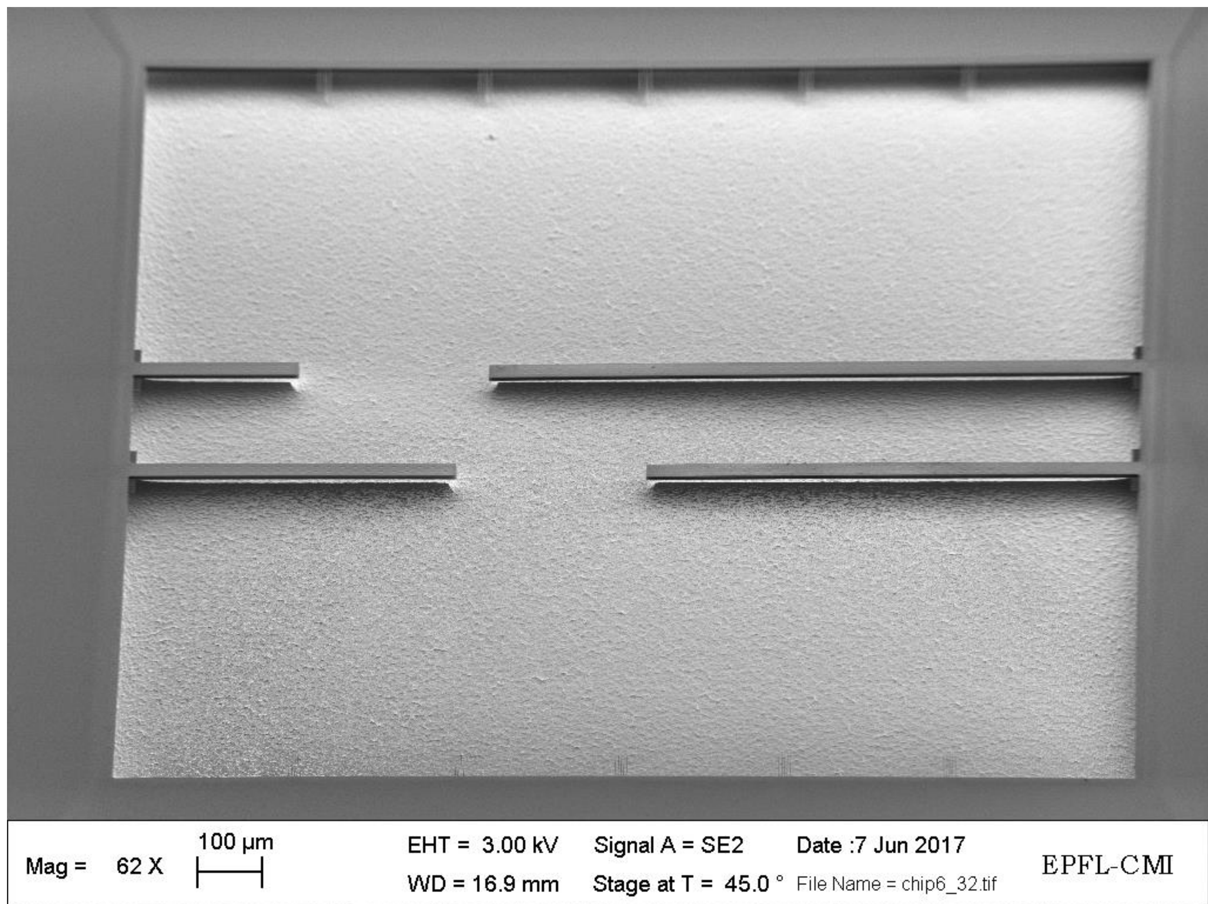

Fig. 47: Chip 10 after the photoresist stripping. Image taken with the SEM.

3.5 Main challenges

Some problems arose during the microfabrication processes. The first obstacles faced were related to the attachment of the chips to their carrier wafers using the QuickStick. During the first tests, using test chips, it was noticed a reflow of the photoresist due to the hotplate high temperature (135 °C). Reflow is the thermal softening and roundening of the photoresist structures. This effect is undesired as it reduces the structures resolution. This problem was circumvented by changing the temperature of the hotplate to 110 °C. This change provided more time to place the chip on top of the carrier wafer before reflow could take place. In this temperature, the QuickStick still melts, enabling the bonding.

Another problem involving the QuickStick was the burning of photoresist during the etching in the SPTS APS. A burned photoresist is much more difficult to strip off. In the SPTS APS tool, the wafer is clamped and cooled during etching, while the chamber is at high temperature due to the plasma source. If the contact between the wafer and the chip is thermally good, the chip will be kept cooled together with the wafer. That was not the case for the first test chips

where the resist on top of the chip was burned after the etching process. To deal with this problem, the chip-to-wafer bonding was optimized to guarantee a thin layer of QuickStick covering the whole area on the back of the chip.

Probably the most difficult challenge was related to the etching rate in the SPTS APS. As discussed before, the first recipe used was load-dependent. The fact that the carrier wafers used were silicon wafers strongly affected the etch rate of the silicon nitride on top of the chips. This problem was minimized by changing the recipe in the etching tool.

There was also a problem during the second photolithography process. In the exposure, initially the same parameters of the first photolithography were used in the MLA 150 tool. However, underexposure, was observed for the first chips. Figure **48** shows chip 8 after development. An excess of photoresist remaining after development is a clear indication of underexposure. To overcome this issue, the exposure dose needed to be increased. An optimized dose of 350 mJ/cm^2 was then used for all the chips. For the first chips, where underexposure occurred, the photoresist was stripped off and photolithography was carried out using the new value of exposure dose.

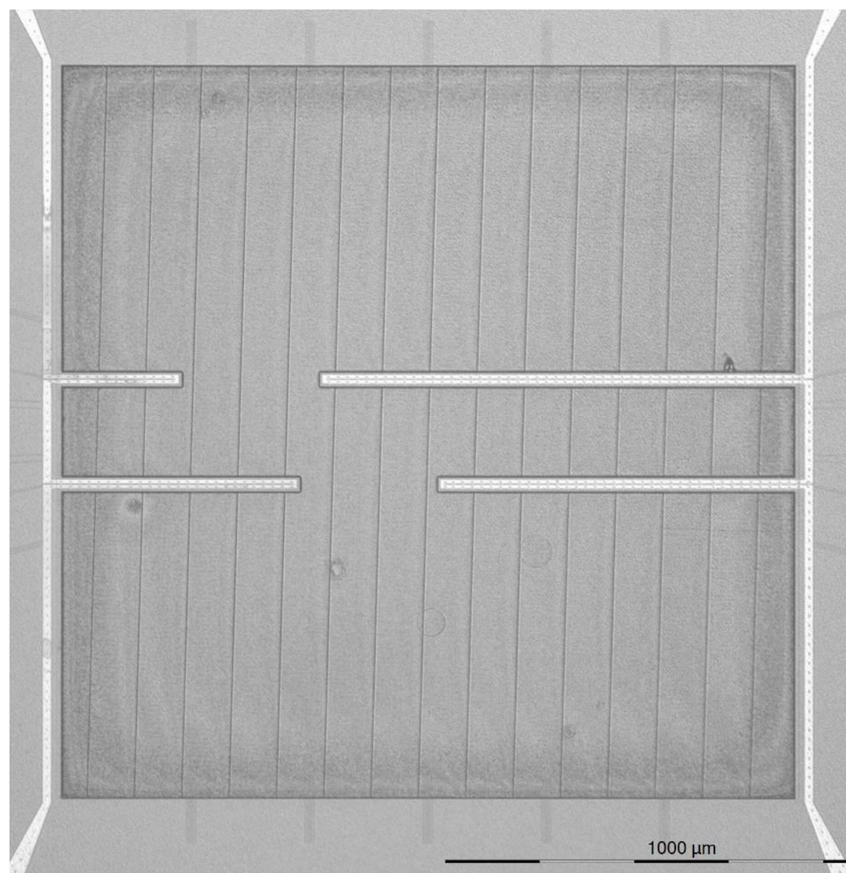

Fig. 48: Chip 8 after development. Excess of resist indicates underexposure. Image taken with Optishot microscope with a magnification of 5x.

3.6 Summary

Suspended microchannel resonators with different off-axis placement were successfully fabricated using the process flow shown in Figure **26**. The chips processed were from wafer 63238. Table **11** summarizes the values of Z_0 obtained.

Table 11: Chips processed with the respective Z_0

Chip ID	**Thickness etched (nm)**	**Z_0**
10	800	0
6	600	0.05
8	550	0.07
12	460	0.09
11	420	0.1
7	0	0.2

4 Microfluidic interface

After the fabrication of the SMRs with different Z_0's, a microfluidic interface needed to be designed in order to fill them with liquid. This interface should be low-cost, easy to implement, vacuum compatible and reusable.

When it comes to microfluidics, a network made of polydimethylsiloxane (PDMS) is usually the first choice. PDMS is by far the most popular material in the academic microfluidic community because it is easy to fabricate, inexpensive, flexible, optic transparent and biocompatible [36]. A microfluidic network made of PDMS bonded to the chip surface was used by Burg and Manalis on their first SMRs to obtain a continuous fluidic delivery to the suspended microchannels [19]. However, PDMS is not suitable for vacuum operation due to its air permeability. This is why the same authors developed a vacuum-packaged SMR later [21]. In this approach, the resonator was vacuum packaged on the wafer scale using glass frit bonding. This solution is not suitable in this work, as it requires a considerable time for processing the glass wafer and cleanroom equipment, increasing remarkably the costs. Moreover, in this stage of the project, chips are being handled, instead of wafers.

As the SMRs fabricated in this work have opening inlets and aiming to keep the microfluidic solution simple, techniques involving fabrication and bonding of a cover layer on top of the chip surface were not considered. Instead, two direct approaches were selected based on what has been used in the literature. It is important to note that tests are currently being carried out to fill the chips with liquid using these two approaches. The approaches are described in detail in the next sub-sections.

4.1 Immersion and sealing

A very simple approach is to immerse the chip into a solution and then close the inlets using epoxy adhesive. Epoxy adhesive DP100 Plus Clear from 3M™ Scotch-Weld™ was selected due to its high shear strength and good peel performance properties as well as its solvent resistance (it is resistant to acetone and isopropyl alcohol, for example).

This technique, currently being tested, is an easy method to fill the microchannels with liquid. Potential air bubbles and stiction of the cantilevers when immersing the chip into the liquid, however, need to be checked prior to the use of this approach to the fabricated SMRs.

4.2 Fluidic connectors

This approach consists of attaching fluidic connectors on top of the inlet openings and deliver

the fluid through commercial tubings with the aid of syringes. The main challenge faced for realizing this microfluidic interface was the lack of space between the inlets and between an inlet and the sensing area containing the resonators. Figure **49** illustrates the layout of a 12-cantilever chip with the dimensions of interest. The sensing area is a square with sides of 1.55 mm, the inlets with dimensions of 86 x 214 μm are separated from each other by a distance of 2.68 mm in the horizontal and 3.84 mm in the vertical. All the chips were designed with these dimensions.

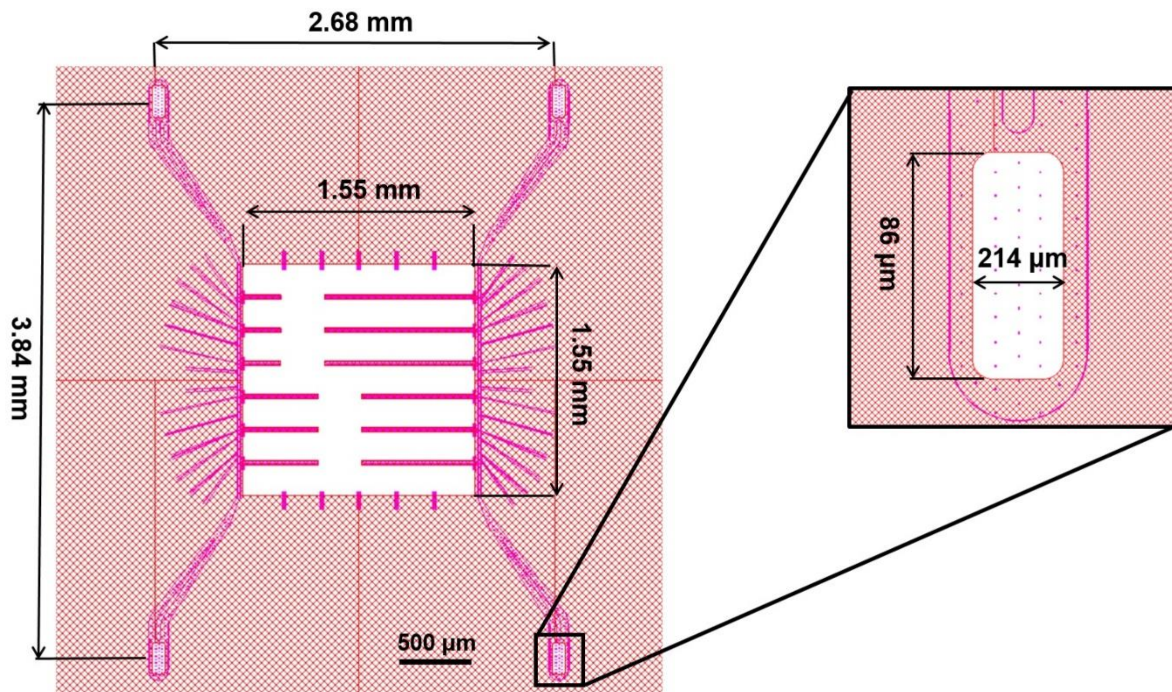

Fig. 49: Closer look of the chip layout. Inset: inlet dimensions. Image from CleWin.

Commercial connectors have been used to build strong connections to chip surfaces. Barton et al. [37] used NanoPort^{TM} connectors from IDEX Health and Science (formerly Upchurch Scientific) to deliver fluid to suspended nanochannel resonators. The authors could fill the NanoPorts with liquids of different densities for resonance measurements in a vacuum chamber. These connectors are made of inert and biocompatible polyetheretherketone (PEEK) and perfluoroelastomer polymers. PEEK is vacuum compatible and has excellent chemical resistance to many commonly solvents such as water, acetone and isopropanol.

Figure **50** shows the NanoPort model N-333. As it can be seen it is comprised of three elements: a head piece, a ferrule and a base. This assembly is designed to be used with a 1/6” OD (outside diameter) tubing. The tubing is held in place by the ferrule when the head piece is tightened. The connector is bonded to the surface of the chip by a pre-formed epoxy adhesive ring,

provided together with the connector (see Figure **51**). These connectors, however, are too big to be used with the SMRs fabricated in this work.

Smaller commercial connectors can be found in the market. For example, the CapTite^{TM} connectors from LabSmith. They have a slim bonded port connector for use in tight spaces. This connector interfaces to 360 µm OD capillary tubes via one-piece fitting, as shown in Figure **52**. Plugs manufactured by the same company can be used to close the connector, after filling with liquid. An epoxy adhesive is used to attach the port to the chip surface. The use of this bonded port, however, is limited due to its dimensions and price. The slim bonded port connector has an external diameter of 2.8 mm, which is slightly larger than the distance between the two inlets (2.68 mm) of our SMRs.

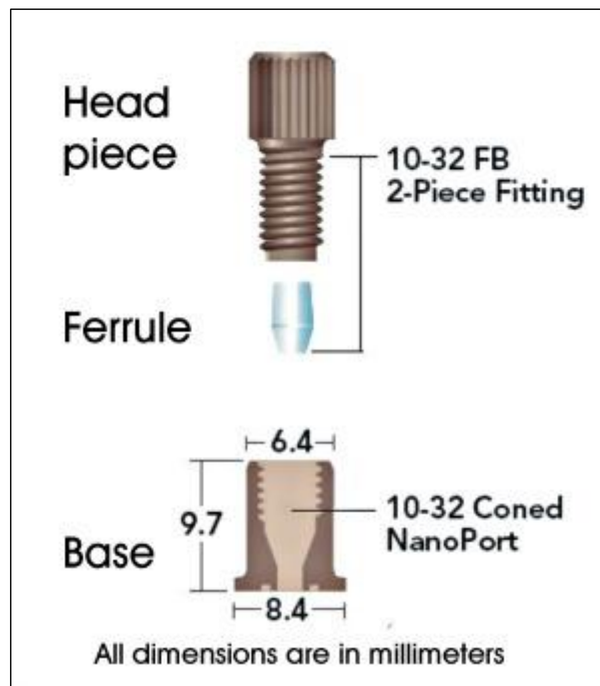

Fig. 50: NanoPort model N-333 [38].

Fig. 51: Examples of NanoPorts. The ring can be seen on the left; mounted NanoPort attached to the chip on the center; NanoPorts with tubing shown on the right [39].

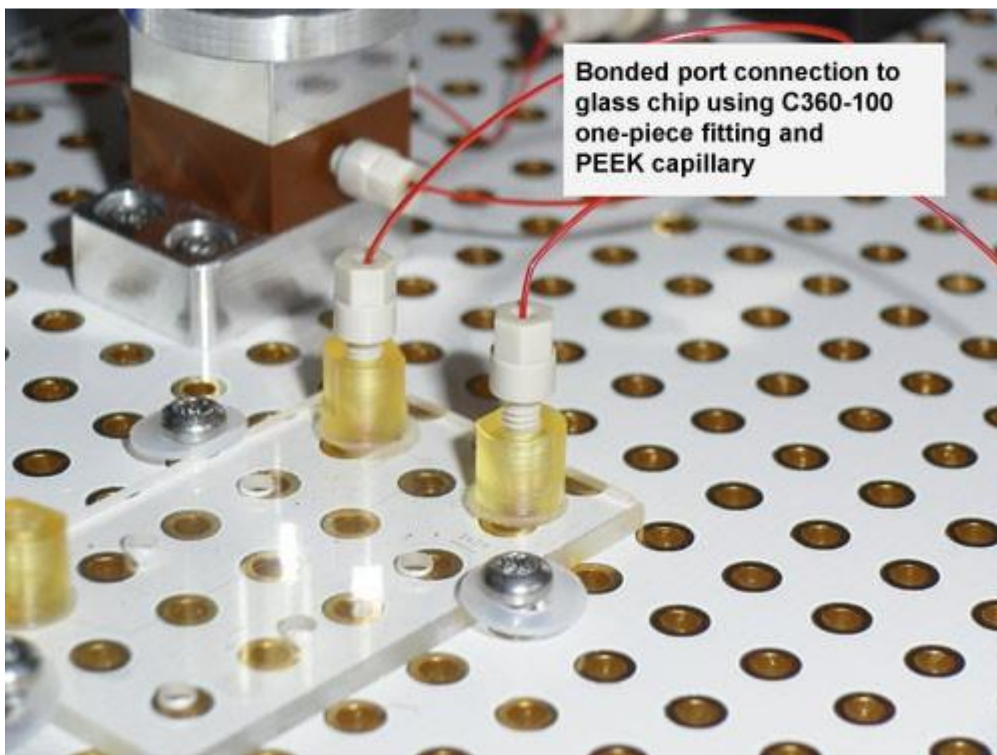

Fig. 52: Slim bonded port from LabSmith attached to a chip. The port interfaces to capillary tubing via one-piece fitting [40].

The solution found was then design and fabricate our own connectors. Two different connectors were drawn using SolidWorks. One consists of a cylinder to interface with a commercial needle (Microlance^{TM}) and the other is a truncated cone to interface with a commercial tubing. The idea was to deliver the fluid with the aid of a syringe. The designs are shown in Figure **53**. The external diameter of the part of the connector in contact with the chip was limited to 2 mm due to the space between the inlets. The drawings with all the dimensions can be found in appendix C.

The connectors were 3D-printed by the Additive Manufacturing Workshop (AMW) from EPFL using stereolithography technique [41]. The material used was RC70, a high temperature resistant resin for building tough and stiff parts at very high resolution [42]. Epoxy adhesive DP100 Plus Clear from 3M™ Scotch-Weld™ was used to bond the connectors to the surface of the chip as well as to connect the needles and the tubings to the connectors.

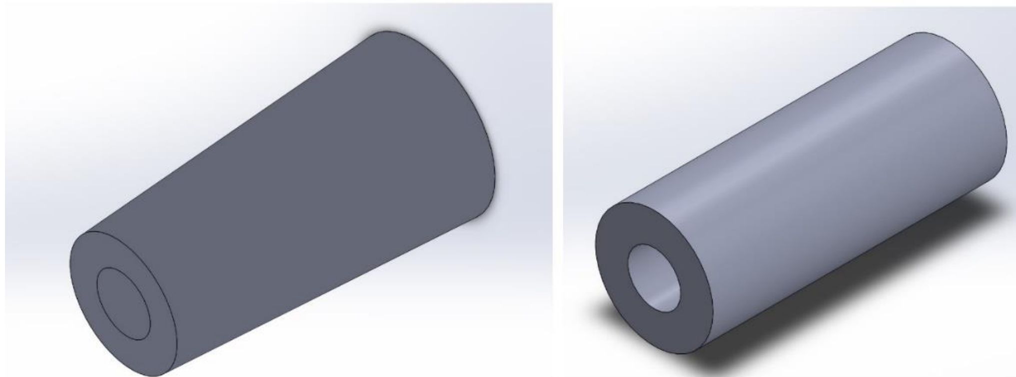

Fig. 53: Connectors designed using SolidWorks. Left: truncated cone to be attached to a tubing (OD = 1.6 mm). Right: cylinder to be attached to a needle (OD = 0.9 mm).

Tests have been performed to check the alignment of the connectors to the inlet openings as well as the sealing using the epoxy adhesive to guarantee the delivery of the fluid. The alignment was successfully achieved using an optical microscope. The proper bonding of the connectors to the surface of the chip, however, is still being optimized using test samples. Figure **54** shows two connectors attached to needles and bonded to a test wafer.

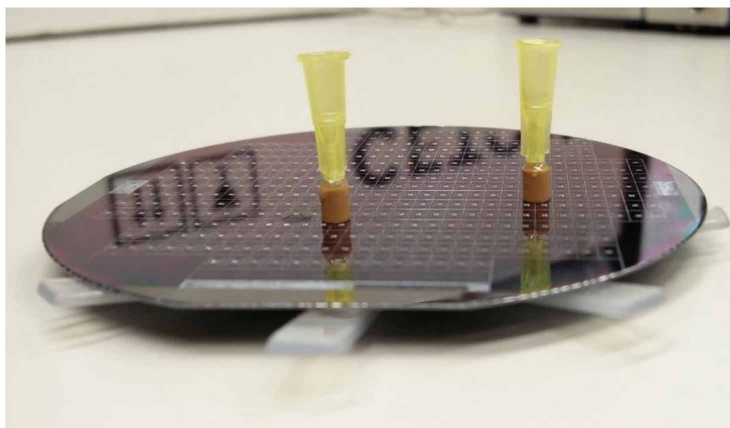

Fig. 54: Connectors bonded to a test wafer.

5 Characterization

5.1 Actuation and detection

A piezoelectric chip and a laser-Doppler vibrometer were used respectively for actuation and detection of the mechanical motion of the resonators.

Piezoelectricity is a material property, discovery in 1880 by Jacques and Pierre Curie [43]. It is the property of a material to generate an electric potential in response to an applied mechanical stress and vice-versa, i.e. the material deforms upon the application of an electric field.

Laser-Doppler vibrometry (LDV) is a non-contact optical technique used for determining the vibrational velocity and displacement at a fixed point. This technology uses the Doppler-effect to measure vibrations. When light is scattered from a moving object, its frequency is slightly shifted. A high-precision interferometer within the vibrometer detects the frequency shifts of the backscattered laser light [44].

Figure **55** illustrates the basic principle of the vibrometer. The laser beam is split into two parts: a reference beam and a measurement (test) beam. The reference beam is pointed directly to the photodetector, whereas the test beam is focused onto the vibrating object. Light is scattered from the moving object, containing the characteristics of the motion. The superposition of this light with the reference beam onto the photodetector creates a signal revealing the Doppler shift in frequency. Further signal processing and analysis provides the vibrational velocity and displacement of the object. As an object moving away and towards the interferometer would generate the same interference pattern, a Bragg cell is used to shift the light frequency, enabling the system to determine the direction of movement.

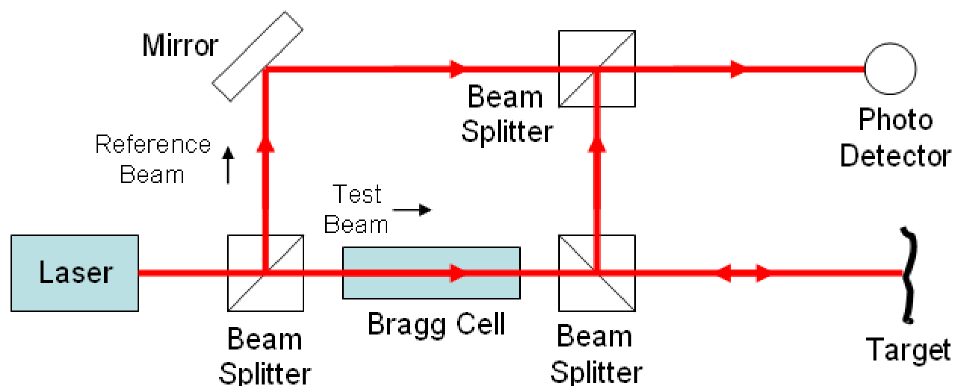

Fig. 55 Schematic of a typical LDV.

5.2 Resonance frequency measurement

The experimental setup used for performing the resonance frequency measurements is composed of a piezoelectric chip, a chamber, a vacuum pump, an optical microscope, a LDV, a lock-in amplifier and a computer. Figure **56** depicts the schematic of the setup.

The LDV is composed of a sensor head unit and a controller (processing unit). OFV-551 fiber-optic sensor head and OFV-5000 vibrometer controller from Polytec GmbH were the tools used. This sensor head utilizes fiber optics and output lens to deliver the laser beam to the measurement point on the resonator and to collect the reflected light as the input to the interferometer. The vibrometer controller was connected to the lock-in amplifier (UHFLI, Zurich Instruments). Figure **57** illustrates these three components.

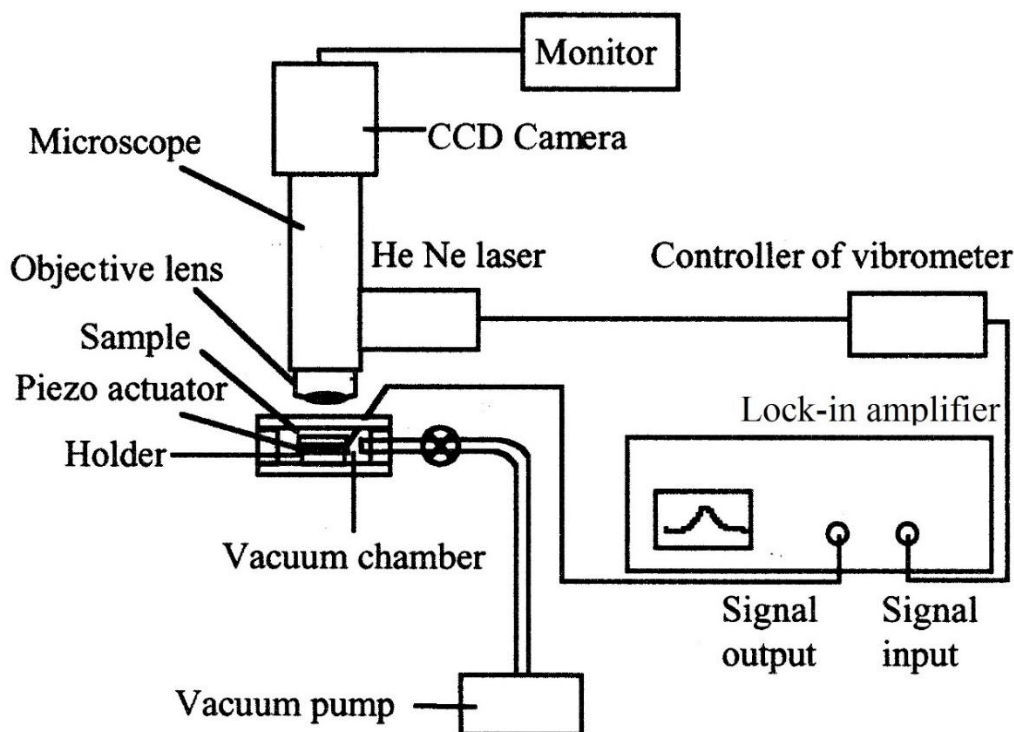

Fig. 56 Experimental setup for measuring the resonance frequency. Cantilever vibrations are actuated by a piezo crystal and detected by LDV [45].

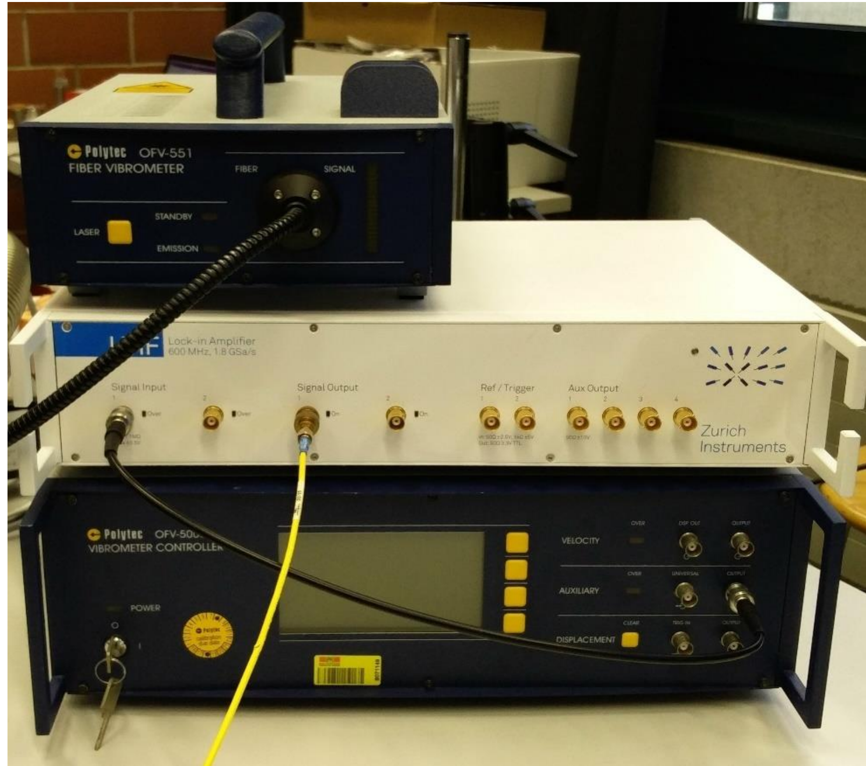

Fig. 57: Sensor head, vibrometer controller and lock-in amplifier. The yellow cable from the amplifier is connected to the piezo crystal, while the fiber optic from the sensor head goes to the microscope.

The chip was placed on top of a platform inside the chamber. The piezoelectric chip (TA0505D024W, Thorlabs Inc) was attached on top of the chip, close to the edge to not break the SMRs (see Figure **58**). A double-sided tape was used for the bonding. For measurements in vacuum, the chamber was closed and the pump turned on. A vacuum gauge was added to detect the pressure inside the chamber. It takes a few hours (3 to 4 hours) to achieve high vacuum (10^{-4} mPa). With the help of the microscope, the laser beam is focused on the cantilever (usually at the tip). The mechanical motion of the resonator is driven using the small piezoelectric crystal, powered by the lock-in amplifier. The frequency response data was then obtained performing a sweep using the lock-in amplifier control software LabOne. Measurements were performed at atmospheric pressure and in vacuum on an empty chip (no fluid).

MatLab codes were used to generate the frequency response plots and to extract the quality factor Q. The codes can be found in appendix D. The measured frequency curves were fitted with a Lorentzian function. Thus, Q could be extracted based on the -3dB bandwidth method.

Figure **59** shows the frequency response at the tip of the 250 µm long cantilever of chip 8 measured in vacuum. The maximum vibration amplitude was achieved at approximately 218.5 kHz, which is the resonance frequency of the cantilever. A comparison of the frequency response to the corresponding Lorentzian is shown in Figure **60**. It can be seen that the fit

agrees with the measured frequency response. Measurements were also performed on the 500 µm long cantilever of chip 8. Figures **61** and Figure **62** illustrates the frequency response in air and in vacuum, respectively, fitted with the Lorentzian function. Comparing the two plots, it can be inferred that while the resonance frequency is approximately constant, the quality factor for the measurement in vacuum is higher than Q in air. The peak in Figure **62** is higher and sharper than the peak in Figure **61**.

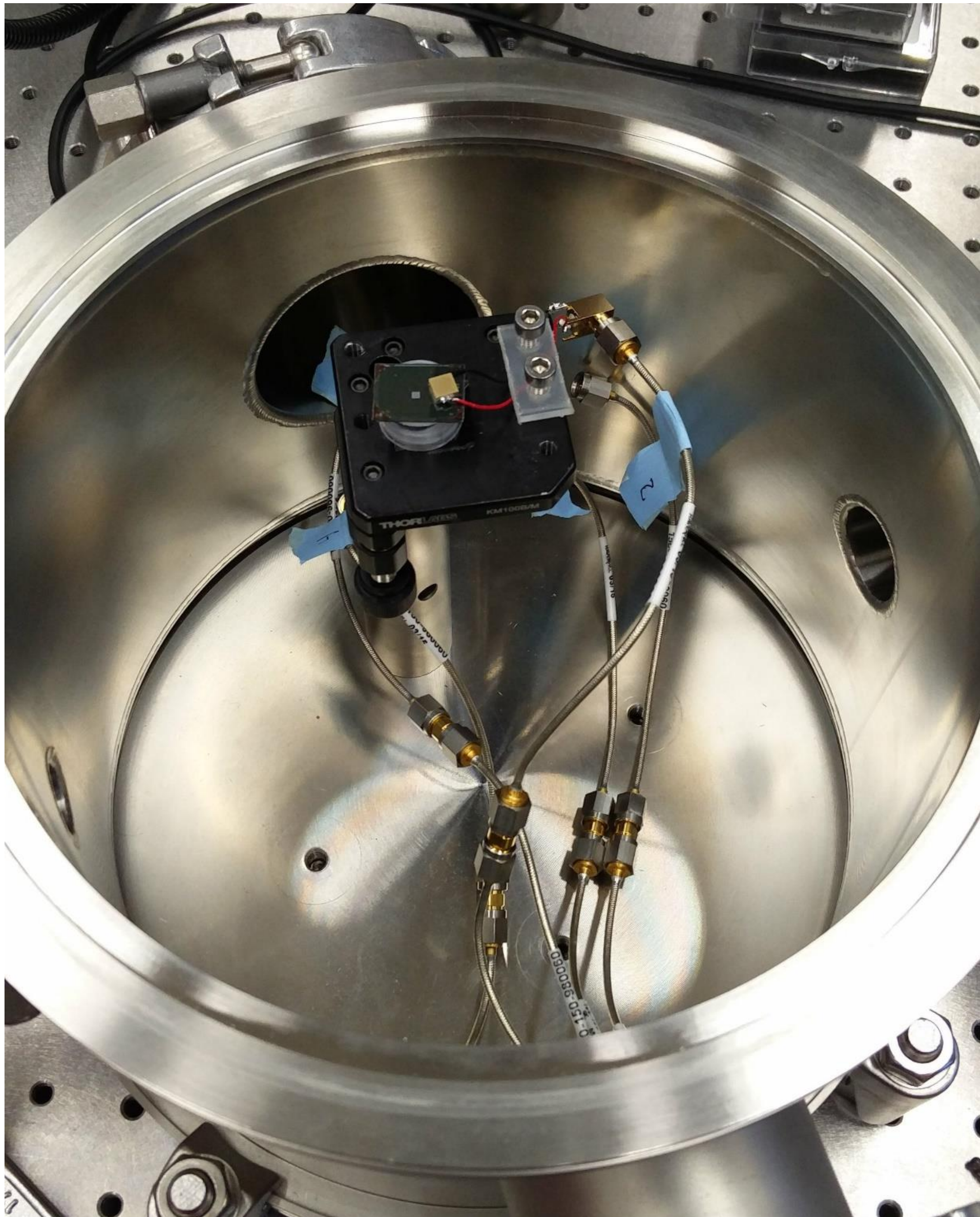

Fig. 58: Chamber environment. The platform, the sample and the piezo chip are shown.

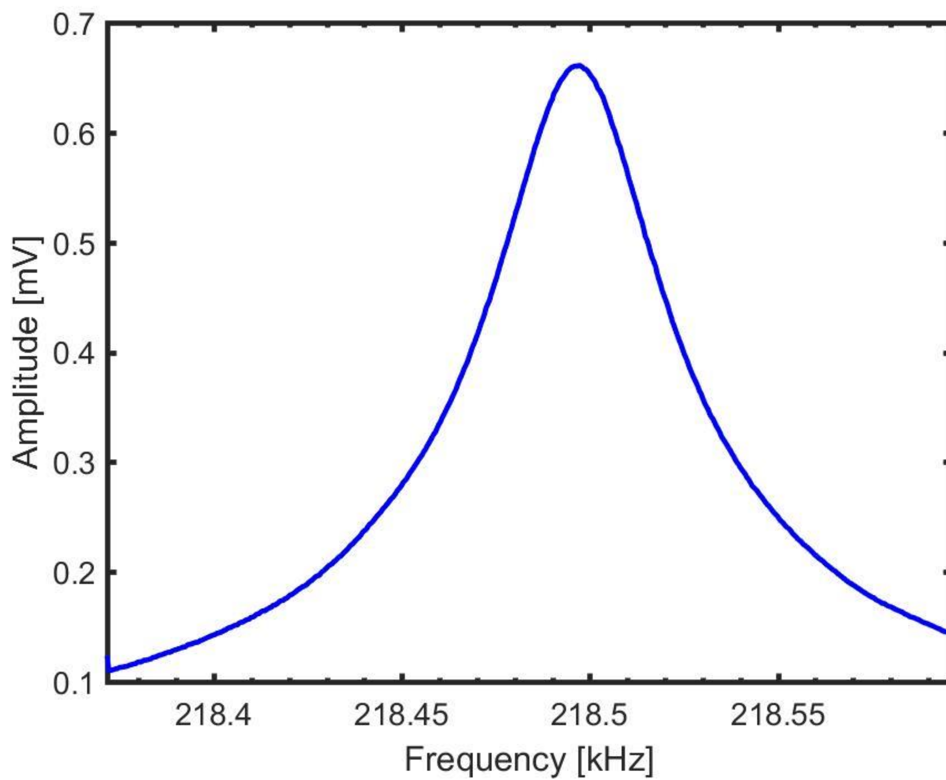

Fig. 59: Frequency response at the tip of a 250 µm cantilever, showing the first resonance frequency. Measurement performed in vacuum ($2{\cdot}10^{-4}$ mPa) with an actuation voltage of 50 mV.

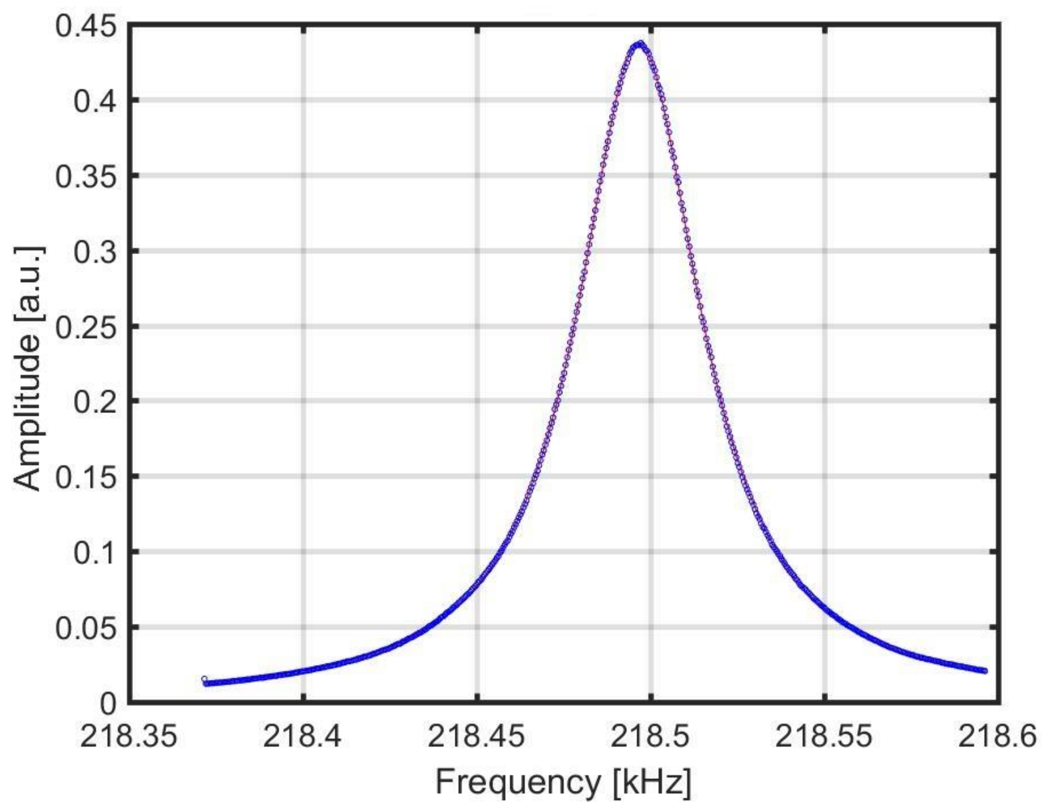

Fig. 60: Fitting of the frequency response with a Lorentzian function (red curve).

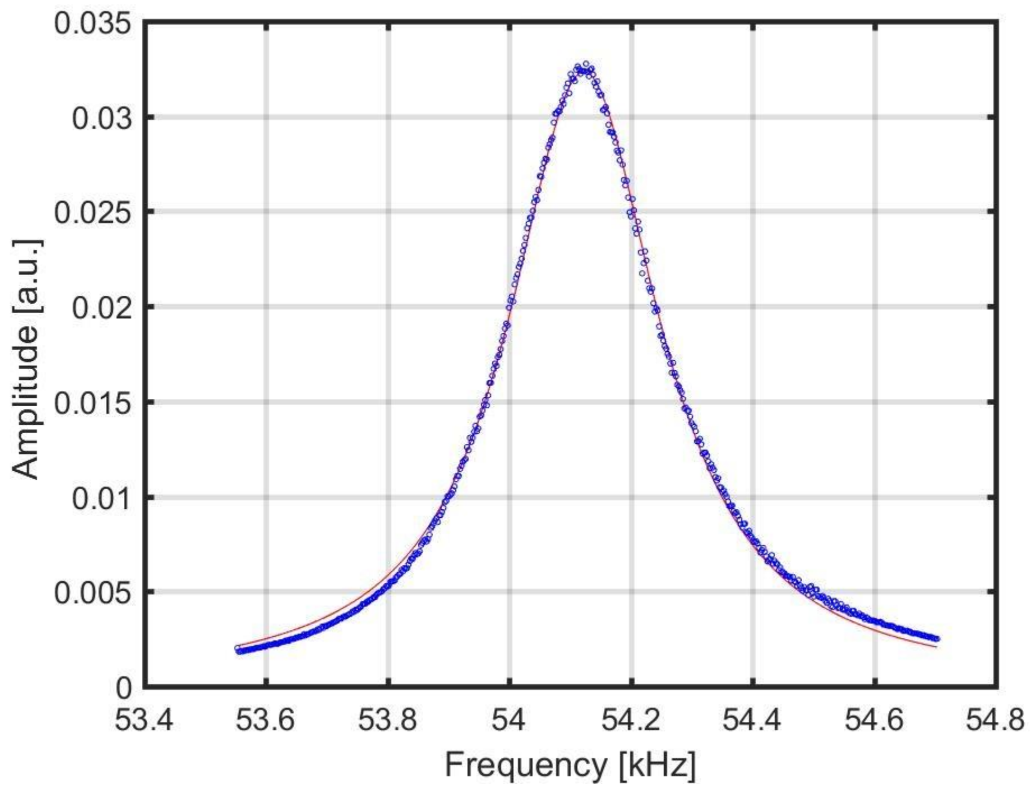

Fig. 61: Frequency response at the tip of a 500 µm cantilever with a Lorentzian fit (red curve). Measurement performed at atmospheric pressure with an actuation voltage of 100 mV.

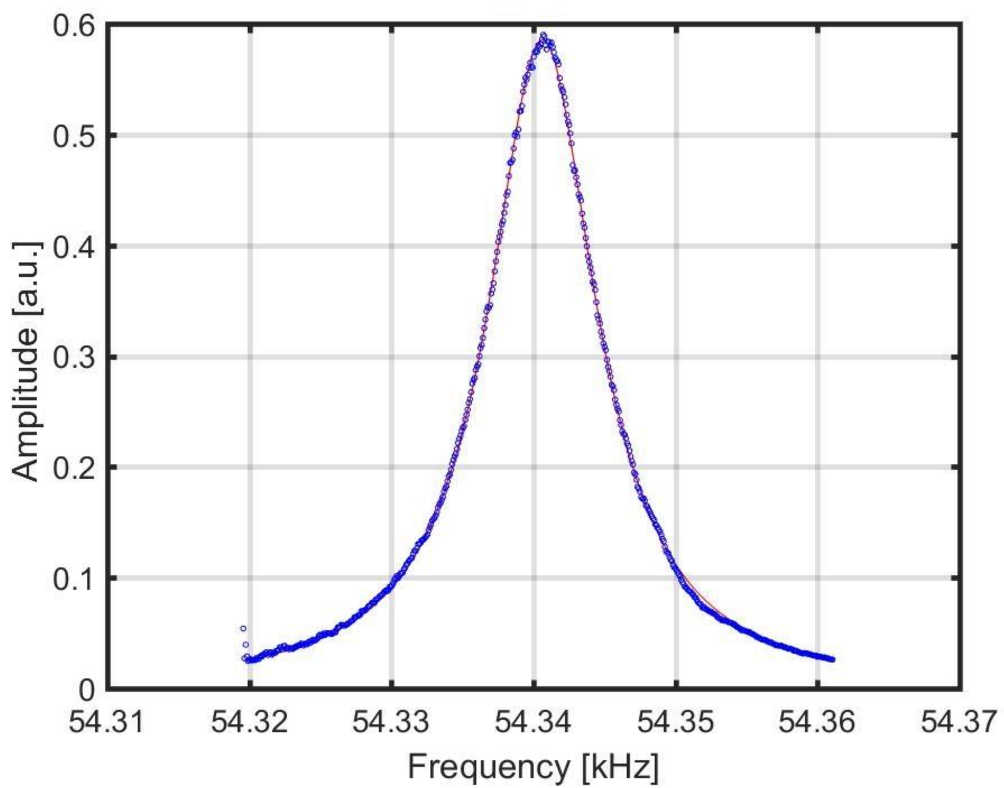

Fig. 62: Frequency response at the tip of a 500 µm cantilever with a Lorentzian fit (red curve). Measurement performed in vacuum ($2\cdot10^{-4}$ mPa) with an actuation voltage of 25 mV.

Table **12** summarizes the measured resonance frequencies and compares with the resonance frequencies simulated in COMSOL Multiphysics. The measured frequencies agree quite well with the simulated ones, with an error of approximately of 2 % for the smaller cantilever and 5 % for the 500 μm cantilever.

Table 12: Comparison between simulated and measured resonance frequency.

Cantilever	Simulated Frequency (kHz)	Measured Frequency (kHz)
250 μm	222.12	218.49
500 μm	57.18	54.34

Table **13** lists the quality factors of both cantilevers for measurements in vacuum and at atmospheric pressure. The quality factor achieved in vacuum were more than one order of magnitude larger than the ones in air. This illustrates the importance of the medium for mechanical resonators. Vacuum must be guaranteed for applications using SMRs, in order to eliminate the dissipative effects of air, as discussed in the first chapter.

Table 13: Comparison between quality factors measured in air and in vacuum.

Cantilever	Q_{air}	Q_{vacuum}
250 μm	338	5058
500 μm	179	5919

6 Conclusions and outlook

A theoretical model concerning the energy dissipation of microfluidic cantilever beam resonators was presented. It was shown that the fluid properties of density and viscosity as well as the fluid compressibility affect the fluid dynamics in these types of resonators. Moreover, it was shown that the non-monotonicity in energy dissipation is a result of competing effects due to fluid inertia and fluid compressibility.

After preliminary studies and considerations about the neutral axis, off-axis placement and Reynolds number of the microchannels used as starting point of this work, a microfabrication process was proposed. Suspended microchannel resonators with six different values of channel off-axis placement were successfully fabricated. By modulation the thickness of the top layer of silicon nitride, values of Z_0 ranging between 0 and 0.2 were obtained.

Two techniques to fill the SMRs with fluid were selected according to availability and chip layout. Because of the chip's dimensions and the short distances between the inlets, the use of commercial connectors was not possible. Connectors were designed in SolidWorks and then manufactured using 3D printing technology (stereolithography). Preliminary tests have been carried out using the two selected techniques.

Using a laser-Doppler vibrometer, measurements of the resonance frequency were performed on empty SMRs. The resonators were actuated by a piezoelectric crystal and the quality factor was determined by fitting the frequency response to a Lorentzian curve. Measurements were performed at atmospheric pressure and in vacuum for two cantilevers with different lengths (250 µm and 500 µm). The measured resonance frequencies agreed with the simulated resonance frequencies, exhibiting a maximum error of 5 %. Quality factors up to 6,000 were achieved for measurements in vacuum, compared to quality factors of hundreds achieved in air.

As prospective work, measurements of the resonance frequency will be carried out on SMRs having different channel off-axis placement, filled with different fluids, such as water, water-glycerol solution and acetone. By extracting the quality factor of these resonators, the influence of Z_0 will be proved and a comparison with the theoretical model will be drawn.

Bibliography

[1] S. Schmid, L. G. Villanueva, and M. L. Roukes, *Fundamentals of nanomechanical resonators*. Cham: Springer, 2016.

[2] G. Yoshikawa *et al.*, "Two dimensional array of piezoresistive nanomechanical Membrane-type Surface stress Sensor (MSS) with improved sensitivity," *Sensors (Switzerland)*, vol. 12, no. 11, pp. 15873–15887, 2012.

[3] S. Schmid, M. Kurek, and A. Boisen, "Towards airborne nanoparticle mass spectrometry with nanomechanical string resonators," *Proc. SPIE 8725, Micro- and Nanotechnology Sensors, Systems, and Applications V*, vol. 8725, p. 872525-872528, Jun. 2013.

[4] J. Tamayo, P. M. Kosaka, J. J. Ruz, Á. San Paulo, and M. Calleja, "Biosensors based on nanomechanical systems," *Chem. Soc. Rev.*, vol. 42, no. 3, pp. 1287–1311, 2013.

[5] J. Melin, P. Enoksson, T. Corman, and G. Stemme, "Resonant silicon sensors", *J. Micromech. Microeng*, vol. 1, pp. 113–125, 1991.

[6] Y. T. Yang, C. Callegari, X. L. Feng, K. L. Ekinci, and M. L. Roukes, "Zeptogram-scale nanomechanical mass sensing," *Nano Lett.*, vol. 6, no. 4, pp. 583–586, 2006.

[7] A. Gupta, D. Akin, and R. Bashir, "Single virus particle mass detection using microresonators with nanoscale thickness," *Appl. Phys. Lett.*, vol. 84, no. 11, pp. 1976–1978, 2004.

[8] T. Thundat, E. A. Wachter, S. L. Sharp, and R. J. Warmack, "Detection of mercury vapor using resonating microcantilevers," *Appl. Phys. Lett.*, vol. 66, no. 13, pp. 1695–1697, 1995.

[9] B. Ilic, H. G. Craighead, S. Krylov, W. Senaratne, C. Ober, and P. Neuzil, "Attogram detection using nanoelectromechanical oscillators," *J. Appl. Phys.*, vol. 95, no. 7, pp. 3694–3703, 2004.

[10] J. E. Sader, "Frequency response of cantilever beams immersed in viscous fluids with applications to the atomic force microscope," *J. Appl. Phys.*, vol. 84, no. 1, pp. 64–76, Jun. 1998.

[11] C. P. Green and J. E. Sader, "Torsional frequency response of cantilever beams immersed in viscous fluids with applications to the atomic force microscope," *J. Appl. Phys.*, vol. 92, no. 10, pp. 6262–6274, 2002.

[12] T. Braun *et al.*, "Micromechanical mass sensors for biomolecular detection in a physiological environment," *Phys. Rev. E - Stat. Nonlinear, Soft Matter Phys.*, vol. 72, no. 3, pp. 1–9, 2005.

[13] H. Zhang, M. S. Marma, E. S. Kim, C. E. McKenna, and M. E. Thompson, "A film bulk acoustic resonator in liquid environments," *J. Micromechanics Microengineering*, vol. 15, no. 10, pp. 1911–1916, 2005.

[14] M. Li, T. X., and R. L., "Ultra-sensitive NEMS-based cantilevers for sensing, scanned probe and very high-frequency applications," *Nat Nano*, vol. 2, no. 2, pp. 114–120, Feb. 2007.

[15] J. Tamayo, A. D. L. Humphris, A. M. Malloy, and M. J. Miles, "Chemical sensors and biosensors in liquid environment based on microcantilevers with amplified quality factor," *Ultramicroscopy*, vol. 86, no. 1–2, pp. 167–173, 2001.

[16] T. P. Burg *et al.*, “Weighing of biomolecules, single cells and single nanoparticles in fluid,” *Nature*, vol. 446, no. 7139, pp. 1066–1069, 2007.

[17] H. Stabinger, “Density Measurement using modern oscillating transducers,” *South Yorkshire Trading Standards Unit*, Sheffield, 1994.

[18] P. Enoksson, G. Stemme and E. Stemme, “Fluid density sensor based on resonance vibration,” *Sens. Actuators A*, vol. 47, no. 1, pp. 327-331, 1995.

[19] T. P. Burg and S. R. Manalis, “Suspended microchannel resonators for biomolecular detection,” *Appl. Phys. Lett*, vol. 83, no. 13, pp. 2698-2700, 2003.

[20] Q-Sense AB. Västra Frölunda, Sweden [Online]. Available: http://www.q-sense.com [Accessed: 01- Jun- 2017]

[21] T. P. Burg *et al.*, “Vacuum-Packaged Suspended Microchannel Resonant Mass Sensor for Biomolecular Detection,” *J. Microelectromechanical Syst.*, vol. 15, no. 6, pp. 1466–1476, 2006.

[22] W. H. Grover, A. K. Bryan, M. Diez-Silva, S. Suresh, J. M. Higgins, and S. R. Manalis, “Measuring single-cell density,” *Proc. Natl. Acad. Sci.*, vol. 108, no. 27, pp. 10992–10996, 2011.

[23] M. Godin, A. K. Bryan, T. P. Burg, K. Babcock, and S. R. Manalis, “Measuring the mass, density, and size of particles and cells using a suspended microchannel resonator,” *Appl. Phys. Lett.*, vol. 91, no. 12, pp. 1–4, 2007.

[24] A. K. Bryan, A. Goranov, A. Amon, and S. R. Manalis, “Measurement of mass, density, and volume during the cell cycle of yeast,” *Proc. Natl. Acad. Sci.*, vol. 107, no. 3, pp. 999–1004, 2010.

[25] A. K. Bryan *et al.,* “Measuring single cell mass, volume, and density with dual suspended microchannel resonators,” *Lab Chip*, vol. 14, pp. 569-576, 2014 .

[26] M. Godin *et al.*, “Using buoyant mass to measure the growth of single cells,” *Nat. Methods*, vol. 7, no. 5, pp. 387–390, May 2010.

[27] S. Byun *et al.*, “Characterizing deformability and surface friction of cancer cells,” *Proc. Natl. Acad. Sci.* , vol. 110, no. 19, pp. 7580–7585, May 2013.

[28] M. F. Khan *et al.*, “Online measurement of mass density and viscosity of pL fluid samples with suspended microchannel resonator,” *Sensors Actuators B Chem.*, vol. 185, pp. 456–461, 2013.

[29] T. P. Burg, J. E. Sader, and S. R. Manalis, “Nonmonotonic energy dissipation in microfluidic resonators,” *Phys. Rev. Lett.*, vol. 102, no. 22, pp. 1–4, 2009.

[30] J. E. Sader, T. P. Burg, and S. R. Manalis, “Energy dissipation in microfluidic beam resonators,” *J. Fluid Mech.*, vol. 650, pp. 215-250, 2010.

[31] G. P. Association, *Physical Properties of Glycerine and Its Solutions*. Glycerine Producers’ Association, 1963.

[32] CMI - Center of MicroNanoTechnology. Manual for Ultrafab Wetbench, 2017. [Online]. Available: https://cmi.epfl.ch/etch/UTF.php. [Accessed: 01- Jun- 2017].

[33] CMI - Center of MicroNanoTechnology. ATMSSE OPTIHOT VB20 HMDS HOTPLATE. [Online]. [Accessed: 01- Jun- 2017].

[34] CMI - Center of MicroNanoTechnology. ATMSSE OPTISPIN SB20 MANUAL COATER. [Online]. Available: https://cmi.epfl.ch/photo/sb20_coater.php. [Accessed: 01- Jun- 2017]

[35] CMI - Center of MicroNanoTechnology. AZ ECI 3000 COATING. [Online]. Available:https://cmi.epfl.ch/photo/photo_process/files/AZ_ECI_3000_spincurve.php. [Accessed: 01- Jun- 2017].

[36] Y. Temiz *et al.*, "Lab-on-a-chip devices: How to close and plug the lab?," *Microelectronic Engineering*, vol. 132, pp. 156-175, 2015.

[37] R. A. Barton, B. Ilic, S. S. Verbridge, B. R. Cipriany, J. M. Parpia, and H. G. Craighead, "Fabrication of a nanomechanical mass sensor containing a nanofluidic channel," *Nano Lett.*, vol. 10, no. 6, pp. 2058–2063, 2010.

[38] Translume. Nanoport Fluid Connectors. [Online]. Available: http://translume.com/index.php/resources/item/200-nanoport-fluid-connectors. [Accessed: 01- Jun- 2017].

[39] CorSolutions, How to Make Microfluidic Connections [Online]. Available: http://www.mycorsolutions.com/fitting-and-connector-tutorial.html. [Accessed: 01- Jun- 2017].

[40] Mengel Enginnering. Bonded port connector. [Online]. Available: http://www.mengelengineering.dk/index.php/bonded-port-connector.html. [Accessed: 01- Jun- 2017].

[41] C. W. Hull, "Apparatus for production of three-dimensional objects by stereolithography," U.S. Patent 4575330 A, March 11, 1986.

[42] Envisiontec. RC70. [Online]. Available: https://envisiontec.com/3d-printing-materials/perfactory-materials/rc70/ [Accessed: 01- Jul- 2017].

[43] J. Curie and P. Curie. "Development by pressure of polar electricity in hemihedral crystals with inclined faces, " *Bull. soc. min. de France*, vol. 3, pp. 90, 1880.

[44] R. Prislan, "Laser Doppler vibrometry and modal testing," Faculty of Math and Phys. Univ. Ljubljana, Ljubljana, 2008.

[45] J. Yang, T. Ono, and M. Esashi, "Energy Dissipation in Submicrometer Thick Single-Crystal Silicon Cantilevers," *J. Microelectromech. Syst.*, vol. 11, no. 6, pp. 775–783, 2002.

Appendices

A. Fabrication details

Microchannel definition

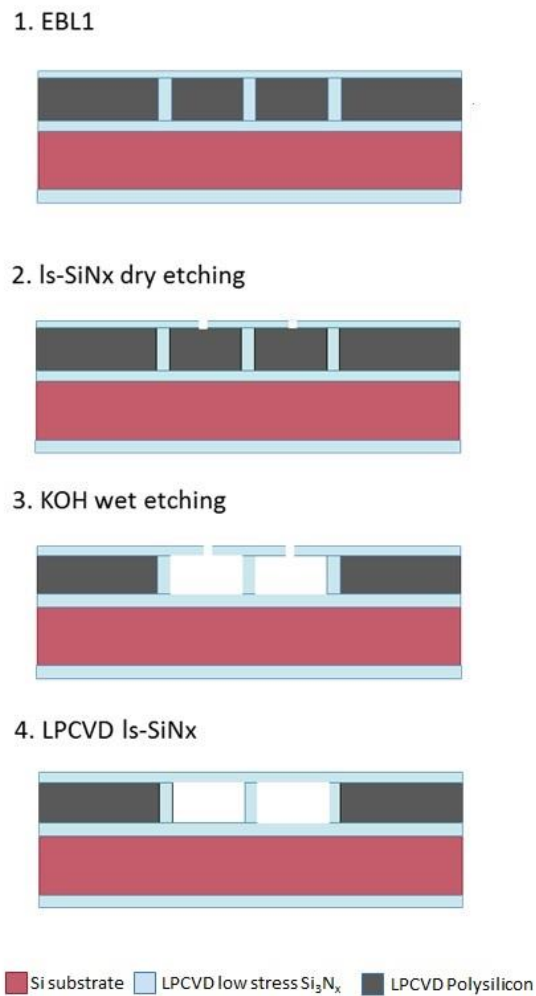

Fig. 63: Representation of the process flow to define the microchannels. EB1 stands for e-beam lithography 1 (Image provided by Annalisa De Pastina from EPFL).

Run-card

Table 14: Detailed run-card for the microfabrication process.

Step	Description	Zone/Tool	Program and Parameters	Remarks
1	**Photolithography (1st)**			
1.1	Coating	Z1/ACS200	Program 0129	HMDS and softbake included in the program
1.2	Exposure	Z5/Heidelberg MLA150	Dose = 220mJ/cm^2, Defocus = -3	
1.3	Development	Z1/ACS200	Program 0929	
1.4	Inspection	Z1/Optical Microscope		Check resolution and alignment
2	**Cleavage**			
2.1	Wafers cleavage	Z1/Cleavage table		Follow cleavage lines. Be gentle
3	**Silicon nitride etching**			
3.1	Top silicon Nitride etch	Z2/SPTS		
3.2	Etching check	Z4/Dektak Profilometer		Check SiN thickness etched (after PR strip)
4	**PR strip (1st)**			
4.1	O2 Plasma	Z2/Tepla	PR_Strip_High, t = 3 min	
4.2	Wet etching	Z2/UFT	UFT resist	Skip QDR
4.3	O2 Plasma	Z2/Tepla	PR_Strip_Low, t = 3 min	
5	**Photolithography (2nd)**			
5.1	HMDS	Z13/VB20 HMDS hotplate	Recipe HMDS STD	
5.2	Coating	Z13/SSE Manual Coater	Program STD-1200-RPM	Resist: ECI AZ 1027. Sofbake at 90°C for 3 min
5.3	Exposure	Z5/Heidelberg MLA150	Dose = 350mJ/cm^2, Defocus = -3	
5.4	Development	Z13/Wet bench	Remover AZ 726 MIF, t = 3 min	
5.5	Inspection	Z13/Optical Microscope		Check resolution and alignment
6	**Top silicon nitride etching**			
6.1	Silicon Nitride Dry Etch	Z2/ AMS	Program SiO2 PR 1:1, time depends on the chip	ER = 280nm-300nm/min
6.2	Inspection	Z6/Optical Microscope		Check if the layer was removed
7	**Polysilicon dry etching**			
7.1	Bosch process	Z2/ AMS	Program SOI ACC ADP, t = 2 min	ER = 3-4.5 µm/min
7.2	Inspection	Z2/Optical microscope		Check if the layer was removed
8	**Bottom silicon nitride etching**			
8.1	Silicon Nitride Dry Etch	Z2/ AMS	Program SiO2 PR 1:1, t = 2 min	ER = 280nm-300nm/min

8.2	Inspection	Z2/Optical microscope		Check if the layer was removed
9	**Silicon dry etching**			
9.1	Bosch process	Z2/ AMS	Program SOI ACC ADP, t = 3 min	
9.2	SF6 Isotropic dry etching	Z2/ AMS	Program Si_release, t = 5min	Divide in two steps (2min+3min)
9.3	Inspection	Z2/Optical microscope		Check release and underetch
10	**PR strip (2nd)**			
10.1	Plasma O2 clean	Z2/Tepla	Strip_High , t = 6 min	Divide in two steps (3min+3min)
10.2	Inspection	Z1/SEM ZEISS LEO		Check release, underetch and cantilever profiles

B. Mathematica Code - Calculation of Silicon Nitride to be Etched

```
(*
Calculation of the amount of top layer to be etched with respect to values of Z0

Numerical values relative to wafer 63238


Main Equations:
```

- Neutral Axis: $\overline{y} = \frac{\sum \overline{y}_i * A_i}{A_i}$

```
For our case:

NeutralAxis =
(1/(bcanti*tSiN1+2*bchannel*internalSiN+3*btrench*tPolySi+4*internalSiN*tPolySi+2*b
channel*internalSiN+bcanti*tSiN2))*((bcanti*tSiN1*(tSiN1/2)+
2*bchannel*internalSiN*(tSiN1+internalSiN/2)+ 3*btrench*tPolySi*(tSiN1+tPolySi/2)+
4*internalSiN*tPolySi*(tSiN1+tPolySi/2)+2*bchannel*internalSiN*(tSiN1+internalSiN+t
channel+internalSiN/2)+ bcanti*tSiN2*(tSiN1+tPolySi+tSiN2/2)))

 - Z0 = (Neutral axis - Channel axis)/tchannel

 - Channel axis = tSiN1 + internalSiN + tchannel/2

*)


EBL2width=1.4*10^-6; (* [m], width of EBL2 apertures *)
internalSiN=0.3*10^-6;(* [m], thickness of the nitride deposited on the internal
walls of the channels, during EBL2 filling *)

bcanti=30*10^-6;(* [m], cantilever width *)
bchannel=10*10^-6-2*internalSiN;(* [m], channel width *)
bflap=4*10^-6; (* [m], lateral nitride flap width, coming from the underecthing
etching of Polysilicon in isotropic etching *)
btrench=1*10^-6 ;(* [m], width of trenches defined with the first ebeam lithography:
channels' walls *)

tSiN1=0.5*10^-6; (* [m], thickness of the first layer of silicon nitride: channels'
floor *)
tPolySi=6*10^-6;(* [m], thickness of the polysilicon layer *)

tchannel=tPolySi-2*internalSiN;(* [m], thickness of the polysilicon: channels'
height. We also consider the deposition of nitride in the inner walls of the
channel while filling EBL2 *)

tSiN2=1.3*10^-6; (* [m], thickness of the second layer of silicon nitride: channels'
top *)

tcanti=tSiN1+tPolySi+tSiN2; (* [m], cantilever thickness *)


TopLayer=tSiN2+internalSiN;(* [m], Total top layer, taking into account the nitride
in the inner walls of the channel *)

Z0={-0.05,-0.04,-0.03,-0.02,-0.01,0, 0.01,
0.02,0.03,0.04,0.05,0.06,0.07,0.08,0.09,0.1,0.15,0.19157088122605365`};

NeutralAxis=Z0*tchannel+tSiN1+internalSiN+tchannel/2

{3.23`*^-6,3.284`*^-6,3.338`*^-6,3.392`*^-6,3.446`*^-6,3.5`*^-
6,3.5539999999999998`*^-6,3.608`*^-6,3.662`*^-6,3.716`*^-6,3.77`*^-6,3.824`*^-
6,3.878`*^-6,3.932`*^-6,3.986`*^-6,4.04`*^-6,4.31`*^-6,4.5344827586206895`*^-6}

(* Isolating tSiN2 from the neutral axis big equation, we can solve it to find the
final tSiN2, called x below *)
```

```
FinaltSiN2=NSolve[(-bcanti/2)*x^2+(parameter*bcanti-tSiN1*bcanti-tPolySi*bcanti)*x-((bcanti*tSiN1*(tSiN1/2)+2*bchannel*internalSiN*(tSiN1+internalSiN/2)+3*btrench*tPolySi*(tSiN1+tPolySi/2)+4*internalSiN*tPolySi*(tSiN1+tPolySi/2)+2*bchannel*internalSiN*(tSiN1+internalSiN+tchannel+internalSiN/2))-parameter*(bcanti*tSiN1+2*bchannel*internalSiN+3*btrench*tPolySi+4*internalSiN*tPolySi+2*bchannel*internalSiN))==0,x]/.parameter-> NeutralAxis
```

```
{{x->{-6.87781*10^-6,-6.80088*10^-6,-6.72462*10^-6,-6.64905*10^-6,-6.57417*10^-6,-6.5*10^-6,-6.42655*10^-6,-6.35384*10^-6,-6.28187*10^-6,-6.21066*10^-6,-6.14021*10^-6,-6.07055*10^-6,-6.00167*10^-6,-5.9336*10^-6,-5.86633*10^-6,-5.79989*10^-6,-5.48029*10^-6,-5.23103*10^-6}},
{x->{3.37805*10^-7,3.68877*10^-7,4.0062*10^-7,4.33046*10^-7,4.66169*10^-7,5.*10^-7,5.34552*10^-7,5.69838*10^-7,6.05868*10^-7,6.42656*10^-7,6.80211*10^-7,7.18546*10^-7,7.57672*10^-7,7.97598*10^-7,8.38335*10^-7,8.79892*10^-7,1.10029*10^-6,1.3*10^-6}}}
```

```
(*We are interested in the positive root of the equation, one for each value of Z0 *)
```

```
FinalTopLayer=(x/.FinaltSiN2[[2]])+internalSiN (* [m], Remaining thickness, taking into account the nitride in the inner walls of the channel *)
```

```
{6.37805*10^-7,6.68877*10^-7,7.0062*10^-7,7.33046*10^-7,7.66169*10^-7,8.*10^-7,8.34552*10^-7,8.69838*10^-7,9.05868*10^-7,9.42656*10^-7,9.80211*10^-7,1.01855*10^-6,1.05767*10^-6,1.0976*10^-6,1.13833*10^-6,1.17989*10^-6,1.40029*10^-6,1.6*10^-6}
```

```
tEtch=TopLayer-FinalTopLayer (* [m], Amount of material to be etched *)
```

```
{9.621945728739746`*^-7,9.311228751880495`*^-7,8.993801774536766`*^-7,8.669538269036925`*^-7,8.338312540447725`*^-7,8.000000000000005`*^-7,7.65447744969199`*^-7,7.301623377171488`*^-7,6.941318259840435`*^-7,6.573444876964952`*^-7,6.197888628414815`*^-7,5.814537858500139`*^-7,5.423284183222774`*^-7,5.024022819118743`*^-7,4.6166529117392693`*^-7,4.201077861703384`*^-7,1.9970821962549892`*^-7,4.235164736271502`*^-22}
```

```
{Z0, tEtch [nm]},
{-0.05, 962.2},
{-0.04, 931.1},
{-0.03, 899.4},
{-0.02, 866.95},
{-0.01, 833.8},
{0.00, 800.0},
{0.01, 765.4},
{0.02, 730.1},
{0.03, 694.1},
{0.04, 657.3},
{0.05, 619.8},
{0.06, 581.5},
{0.07, 542.3},
{0.08, 502.4},
{0.09, 461.7},
{0.10, 420.1},
{0.15, 199.7},
{0.20, 0.0}
```

C. Drawings

4 3 2 1

F E D C B A

Ø2

Ø0.90

5

UNLESS OTHERWISE SPECIFIED: DIMENSIONS ARE IN MILLIMETERS SURFACE FINISH: TOLERANCES: LINEAR: ANGULAR:	FINISH:	DEBURR AND BREAK SHARP EDGES	DO NOT SCALE DRAWING	REVISION
	NAME	SIGNATURE	DATE	TITLE:
DRAWN				
CHK'D				
APPV'D				
MFG				
Q.A			MATERIAL:	DWG NO. port_v1 A4
			WEIGHT:	SCALE:10:1 SHEET 1 OF 1

SOLIDWORKS Educational Product. For Instructional Use Only.

4 3 2 1

F E D C B A

⌀2

⌀1

5

⌀2.60

⌀1.60

UNLESS OTHERWISE SPECIFIED: DIMENSIONS ARE IN MILLIMETERS SURFACE FINISH: TOLERANCES: LINEAR: ANGULAR:	FINISH:	DEBURR AND BREAK SHARP EDGES	DO NOT SCALE DRAWING	REVISION

	NAME	SIGNATURE	DATE		TITLE:
DRAWN					
CHK'D					
APPV'D					
MFG					
Q.A				MATERIAL:	DWG NO. truncated_cone A4
				WEIGHT:	SCALE:10:1 SHEET 1 OF 1

SOLIDWORKS Educational Product. For Instructional Use Only.

D. MatLab Codes

```
%Averaging sweep amplitude data from the Zurich Instrument lock-in
%amplifier
%2017-03-22 Annalisa De Pastina

%1 Load measurement file to Workspace
%2 Run code

clear Freq Impedance ImpMean
close all

NoS =size(dev2063.demods.sample); %Get the number of sweeps

Freq = dev2063.demods.sample{1,1}.frequency'; %Get frequency data

%Move all amplitudes data into one matrix
for i = 1:max(NoS)
    Amplitude(:,i) = dev2063.demods.sample{1,i}.r(1,:);
    Phase(:,i) = dev2063.demods.sample{1,i}.phase(1,:);

end


%Plot each data set: Amplitude
for t = 1:max(NoS)
    if t == 1
    figure(1)
    plot(dev2063.demods.sample{1,t}.frequency*10^-3,Amplitude(:,1),'-
b','LineWidth',2);
    grid OFF
    %set(gca, 'yscale', 'log'); %Change to log scale
    set(gca, 'xscale', 'log'); %Change to log scale
    set(gcf,'color','w'); %Remove the gray rim around of plot
    set(gca,'FontSize',12) %Set fontsize to 12
    set(gca,'LineWidth',2) %Set axis line width to 2
    xlabel('Frequency [kHz]') %Labeling of x
    ylabel('Amplitude [mV]') %Labeling of y


   hold on
   pause(0.5)
   else
        plot(dev2063.demods.sample{1,t}.frequency*10^-
3,Amplitude(:,t),'LineWidth',2) %Plot all the sweeps for the modulus of the
impedance
        pause(0.5)
   end
end

%Plot each data set: Phase
for z = 1:max(NoS)
    if z == 1
    figure(3)
    plot(dev2063.demods.sample{1,z}.frequency*10^-3,Phase(:,1),'-b','LineWidth',2)
    grid OFF
    set(gca, 'xscale', 'log'); %Change to log scale
    set(gcf,'color','w'); %Remove the gray rim around of plot
    set(gca,'FontSize',12) %Set fontsize to 12
    set(gca,'LineWidth',2) %Set axis line width to 2
    xlabel('Frequency [kHz]') %Labeling of x
    ylabel('Phase [°]') %Labeling of y
   hold on
   pause(0.5)
   else
    plot(dev2063.demods.sample{1,z}.frequency*10^-3,Phase(:,z),'LineWidth',2)
%Plot all the sweeps for the phase of the impedance
```

```
        pause(0.5)
    end

end

array=horzcat(Freq, Amplitude);  % Concatenates Freq and Ampl in an array

%call the function lorentzfit(array)to obtain f0 and Q values
```

Published with MATLAB® R2017a

```
%Annalisa De Pastina, 2017.03.22
%this function gets array as a input where the frequency is the first
%column, all the other columns are amplitudes
%It makes a lorentzian fit of the square of the amplitude signal, and returns f0
and Q as strings
%f0 and Q values can be displayed and copied to store from the command window

function fitlor = lorentzfit(array)
close all

meff=2.55e-15;
guessQ=1000;
    for j=2:length(array)
        if j==2
            ampl = (array(:,j)/max(array(:,j))).^2;   %amplitude to the square
after being normalized to 1
            freq = array(:,1);    %define frequency values
            [maximum, number] = max(ampl);
            guessamp=pi*freq(number,1)/2/guessQ*maximum;

            ftype = fittype('off1 + amplitude*f0/2/pi/Q/((x - f0)^2 +
(f0/2/Q)^2)');   %define fit function (Lorentzian)
            opts =
fitoptions('Method','NonlinearLeastSquares','Algorithm','Levenberg-
Marquardt','TolX',1e-10,'TolFun',1e-10,'StartPoint', [guessQ guessamp
freq(number,1) 0]);
            fitlor = fit(freq, ampl, ftype, opts);
            fitlor3=fitlor(freq)*max(array(:,j))^2;

            disp(strcat('f0 from fit = ', num2str(fitlor.f0)));
            disp(strcat('Q from fit  = ', num2str(fitlor.Q)));


            figure
            %plot(freq,fitlor3,'r-');
            plot(freq*10^-3,fitlor3,'r-',freq*10^-
3,ampl*max(array(:,2))^2,'bo','MarkerSize',2);
                grid ON
                %set(gca, 'yscale', 'log'); %Change to log scale
                %set(gca, 'xscale', 'log'); %Change to log scale
                set(gcf,'color','w'); %Remove the gray rim around of plot
                set(gca,'FontSize',12) %Set fontsize to 12
                set(gca,'LineWidth',2) %Set axis line width to 2
                xlabel('Frequency [kHz]') %Labeling of x
                ylabel('Amplitude [a.u.] ') %Labeling of y
                str=sprintf('n= 6        20mV signal');

                  str=sprintf('n= %d',j-1);
                    %str=sprintf('channel length/cantilever length = 1');
                    title(str);
            hold on
```

```
                 if fitlor.off1>0
                     y0=sqrt(fitlor.off1);
                 else
                     y0=0;
                 end
         else
             ampl = (array(:,j)/max(array(:,j))).^2;    %amplitude to the square
after being normalized to 1
             freq = array(:,1);     %define frequency values
             [maximum, number] = max(ampl);
             guessamp=pi*freq(number,1)/2/guessQ*maximum;

             ftype = fittype('off1 + amplitude*f0/2/pi/Q/((x - f0)^2 +
(f0/2/Q)^2)');   %define fit function (Lorentzian)
             opts =
fitoptions('Method','NonlinearLeastSquares','Algorithm','Levenberg-
Marquardt','TolX',1e-10,'TolFun',1e-10,'StartPoint', [guessQ guessamp
freq(number,1) 0]);
             fitlor = fit(freq, ampl, ftype, opts);
             fitlor3=fitlor(freq)*max(array(:,j))^2;

             disp(strcat('', num2str(fitlor.f0)));
             disp(strcat('', num2str(fitlor.Q)));

             Q(:,j)=fitlor.Q;
             %plot(freq,fitlor3)
             figure
             plot(freq*10^-3,fitlor3,'r-',freq*10^-3,ampl*max(array(:,j))^2,'b.');
             grid ON
                 %set(gca, 'yscale', 'log'); %Change to log scale
                 %set(gca, 'xscale', 'log'); %Change to log scale
                 set(gcf,'color','w'); %Remove the gray rim around of plot
                 set(gca,'FontSize',12) %Set fontsize to 12
                 set(gca,'LineWidth',2) %Set axis line width to 2
                 xlabel('Frequency [kHz]') %Labeling of x
                 ylabel('Amplitude (Lorentzian fit) ') %Labeling of y


             str=sprintf('n= %d',j-1);
                %str=sprintf('channel length/cantilever length = 1');
                title(str);
                 pause(0.1)
         end
     end
end
```

Published with MATLAB® R2017a